

SURFACE AND MECHANICAL PROPERTIES OF CARBON STEEL AFFECTED BY ROTATING CONTINUOUS WAVE LASER TREATMENT

庄, 樹森

<https://hdl.handle.net/2324/4496049>

出版情報 : Kyushu University, 2021, 博士 (工学) , 課程博士
バージョン :
権利関係 :

**SURFACE AND MECHANICAL PROPERTIES OF
CARBON STEEL AFFECTED BY ROTATING
CONTINUOUS WAVE LASER TREATMENT**

Shusen Zhuang

SURFACE AND MECHANICAL PROPERTIES OF CARBON
STEEL AFFECTED BY ROTATING CONTINUOUS WAVE
LASER TREATMENT

A Thesis Submitted
In Partial Fulfillment of the Requirements
For the Degree of
Doctor of Engineering

By
Shusen Zhuang



to the
DEPARTMENT OF URBAN AND ENVIRONMENTAL ENGINEERING
GRADUATE SCHOOL OF ENGINEERING
KYUSHU UNIVERSITY
Fukuoka, Japan
September, 2021


DEPARTMENT OF URBAN AND ENVIRONMENTAL ENGINEERING
GRADUATE SCHOOL OF ENGINEERING
KYUSHU UNIVERSITY
Fukuoka, Japan

CERTIFICATE

The undersigned hereby certify that they have read and recommended to the Graduate School of Engineering for the acceptance of this Thesis entitled, “*Surface and mechanical properties of carbon steel affected by rotating continuous wave laser treatment*” by **Shusen Zhuang** in partial fulfillment of the requirements for the degree of **Doctor of Engineering**.

Dated: September, 2021

Thesis Supervisor:

貝沼重信 

Assoc. Prof. Shigenobu Kainuma, Dr. Eng.

Examining Committee:

濱田秀則 

Prof. Hidenori Hamada, Dr. Eng.

中野博昭 

Prof. Hiroaki Nakano, Dr. Eng.

ABSTRACT

Laser surface treatment has found successful applications in various fields. Surface contaminants such as corrosion products, paint, and salt can be efficiently removed by laser cleaning. However, an appropriate laser-based cleaning technique for larger size structures is still lacking. Although laser surface treatment has the potential to achieve better surface conditions, higher scanning speed and laser power are required to improve the treatment efficiency when targeting a large structure. A new method using high-power continuous-wave (CW) laser is proposed in this study as an alternative surface preparation technique for large steel structures. However, when using a high-power CW laser to clean a corroded structure, the laser beam will affect the base metal to a certain degree, owing to intense laser ablation effects and uncertainty in human operation. The major concerns of laser surface treatment are surface defects could result from laser irradiation, as long as oxide formation and microstructure modification on the steel surface. Thus, the durability and safety of steel structures could be affected by the high-power CW laser surface treatment.

To evaluate the effects of laser treatment on the surface properties and tensile behavior of the base metal, this study adopted a rotating high-power CW laser equipment to irradiate bare carbon steel plates. A modified calculation method for laser-induced peak temperature distribution considering overlapping effects was proposed. Different laser processing parameters were adopted, representing lower to higher laser thermal effects. The surface morphologies, iron oxide and microstructures after laser irradiation were evaluated using optical microscope, electrochemical test, SEM-EDX and XRD studies. Furthermore, tensile behavior of laser-treated steel coupons also tested to investigate the thermal effects on the mechanical properties of carbon steel.

The results showed that the peak temperature distribution obtained from the modified calculation method properly describes the re-melted zone depth in laser-treated specimens. The modified calculation method could help to optimize laser processing parameters to reduce melting of base material and avoid surface defects. Higher laser power density and interaction time result in denser iron oxide formed on the steel surface, which is the main reason for the improved corrosion resistance. The laser condition with proper processing

ABSTRACT

parameters will bring desirable laser ablation effects without damage the base metal. However, when the laser thermal effects increased, surface defects and modified microstructures will affect the mechanical properties of carbon steel, and result in decreasing elongation. Proper laser processing parameters are suggested in this study basing on the temperature calculation method and experimental analysis.

TABLES OF CONTENTS

ABSTRACT i

TABLES OF CONTENTS.....iii

LIST OF TABLES v

LIST OF FIGURES..... vi

CHAPTER 1 INTRODUCTION..... 1

 1.1 Background..... 1

 1.2 Objectives and scope 4

 1.3 Literature review..... 6

 1.4 Organization and outline 10

**CHAPTER 2 PEAK TEMPERATURE DISTRIBUTION IN STEEL
MATERIAL DURING LASER IRRADIATION..... 12**

 2.1 Introduction 12

 2.2 Laser equipment and processing parameters used in this study 13

 2.3 Analytical equations for temperature field produced by CW laser 15

 2.4 Calculation for peak temperature distribution of rotating CW laser 21

 2.5 Summary..... 37

**CHAPTER 3 SURFACE PROPERTIES AND MICROSTRUCTURES
OF LASER-TREATED CARBON STEEL 38**

 3.1 Introduction 38

 3.2 Experimental..... 41

 3.3 Surface morphology of laser-treated carbon steel plates..... 44

 3.4 Evaluation of oxide layer on steel surface after laser treatment..... 50

 3.5 Evaluation of microstructure and hardness distribution on cross-section of
 laser-treated specimens..... 54

 3.6 Consideration of laser effectiveness in field application..... 56

 3.7 Summary..... 62

CHAPTER 4 ELECTROCHEMICAL PROPERTIES OF LASER-TREATED CARBON STEEL SURFACE.....	64
4.1 Introduction	64
4.2 Experimental.....	65
4.3 Electrochemical test results of laser-treated and unirradiated specimens	66
4.4 Summary.....	81
CHAPTER 5 TENSILE PROPERTIES OF LASER-TREATED STEEL COUPON.....	82
5.1 Introduction	82
5.2 Experimental.....	83
5.3 Tensile test results.....	84
5.4 Fractography and fracture mechanism of specimens	89
5.5 Summary.....	97
CHAPTER 6 CONCLUSIONS AND FUTURE WORK	98
6.1 Main conclusions and innovations	98
6.2 Summary.....	98
6.3 Recommendations for future work	100
REFERENCES	102
ACKNOWLEDGEMENT	115

LIST OF TABLES

Table 2-1 Processing parameters of different laser treatment conditions.....	14
Table 2-2 Physical properties of SM490A carbon steel used for laser treatment.....	22
Table 2-3 Number of repetition irradiation n in different laser treatment conditions. ...	34
Table 2-4 Comparison of MZ depth obtained from OM microstructure and calculation method.	35
Table 4-1 Fitted electrochemical parameters of specimens in 3.5 wt% NaCl solution. .	70
Table 4-2 Fitted impedance parameters from EIS of laser-treated and unirradiated specimens.	78
Table 5-1 Average tensile test results and standard deviation	87

LIST OF FIGURES

Figure 1-1 Coating failure due to insufficient surface preparation and underlying corrosion.	1
Figure 1-2 Corrosion problem of weathering steel bridge.	2
Figure 1-3 Residual salts on the steel surface before and after laser treatment.....	3
Figure 1-4 Output power and duration for the pulsed and continuous wave laser.	8
Figure 1-5 Flowchart of the dissertation.....	11
Figure 2-1 Schematic illustration of rotating CW laser treatment.....	14
Figure 2-2 Laser spot size and energy distribution for different laser conditions.	15
Figure 2-3 The geometry of the integral method for calculating the heat cycle at the point P.	16
Figure 2-4 Schematic illustration of calculation portion and period for the temperature-time curves.....	22
Figure 2-5 Temperature-time curves of laser conditions used in this study for carbon steel SM490A.	23
Figure 2-6 Diagrammatic drawing of overlapped areas during rotating laser irradiation.	26
Figure 2-7 Experimental setup of laser irradiation using XY-axis motorized stage.....	28
Figure 2-8 Surface conditions of laser-treated specimens.....	29
Figure 2-9 OM surface morphologies and microstructures on cross-section of laser-treated specimens at Region A and Region B.....	31
Figure 2-10 Schematic illustration of laser-melted pool and bulge formation.....	32
Figure 2-11 OM cross-section of unirradiated and laser-treated specimens.	33
Figure 2-12 Peak temperature distribution on the cross-section of laser-treated specimens.	35
Figure 3-1 Schematic diagram of laser ablation effects.	39
Figure 3-2 Untreated area under higher laser ring moving speed.	39
Figure 3-3. Surface conditions of severely corroded steel member before and after removing the rust layer.	40
Figure 3-4. Laser defocus on the severely corroded steel surface.....	41

LIST OF FIGURES

Figure 3-5 Specimens under different laser beam overlapping rate.	43
Figure 3-6 Specimens with artificial corrosion pits and laser irradiation path.	44
Figure 3-7 OM surface morphologies of specimens.	46
Figure 3-8 Cross-section profile of laser-treated specimens.	48
Figure 3-9 Surface roughness of laser-treated specimens.	49
Figure 3-10 SEM-EDX analysis on surface of specimens.	51
Figure 3-11 XRD diffraction patterns of laser-treated specimens.	52
Figure 3-12 XRD semi-quantitative analysis of iron oxide formed on specimen surface.	53
Figure 3-13 OM microstructure on cross-section of laser-treated specimens.	55
Figure 3-14 HAZ and HV on cross-section of laser-treated specimens.	56
Figure 3-15 Surface condition of steel plate after laser treatment with varying laser beam overlapping rate.	57
Figure 3-16 Observation positions on specimen with artificial corrosion pit.	58
Figure 3-17 Surface morphology of laser-treated specimens with artificial corrosion pits.	59
Figure 3-18 High speed camera of the fume generated during CW laser irradiation.	60
Figure 3-19 Schematic illustration of the effects of pitting width on laser irradiation. ...	60
Figure 3-20 SEM-EDX analysis on laser-treated specimens with artificial corrosion pits.	61
Figure 4-1 Equipment setup of the electrochemical test.	65
Figure 4-2 Potential-time measurements of laser-treated and unirradiated specimens immersed in 3.5 wt% NaCl solution for (a) 1 h and (b) 24 h.	67
Figure 4-3 Potentiodynamic polarization curves of laser-treated and unirradiated specimens in 3.5 wt% NaCl solution.	70
Figure 4-4 Surface morphologies of specimens before and after potentiodynamic polarization test.	72
Figure 4-5 EIS results of laser-treated and unirradiated specimens in 3.5 wt% NaCl solution showed by (a) Nyquist plots, (b) Bode plot of magnitude Z and (c) Bode plot of phase angle.	75
Figure 4-6 Equivalent circuit used to fit EIS data of (a) Unirradiated specimen and (b)	

LIST OF FIGURES

Laser-treated specimen.	76
Figure 4-7 Contour plot of laser-treated specimens before and after potentiodynamic polarization test.	79
Figure 4-8 Schematic illustration of corrosion progress under different surface condition.	80
Figure 5-1 Schematic of macrofractography of the fracture surface.	83
Figure 5-2 Size of tensile specimens basing on JIS Z2201.	84
Figure 5-3 Fracture portions of specimens after tensile test.	85
Figure 5-4 Nominal stress-strain curves of specimens.	86
Figure 5-5 Schematic illustration of energy density result from laser irradiation.	88
Figure 5-6 Relationship between laser energy density and mechanical properties.	88
Figure 5-7 Fracture surface of specimens.	90
Figure 5-8 SEM observation position and fractographs of specimens.	92
Figure 5-9 Illustrative sketches of fracture mechanism from thickness direction.	93
Figure 5-10 Schematic illustration of hardness and MZ&HAZ on cross-section of laser-treated tensile specimens.	94

CHAPTER 1 INTRODUCTION

1.1 Background

Surface preparation is a common procedure for steel-structure maintenance. Abrasive blasting is a widely used technique for surface preparation. However, there are problems such as environmental concerns and flash rust on the steel surface after abrasive blasting. Similar problems can also be observed in chemical preparation methods [1]. Besides, the residual salts and contaminants on steel surfaces after abrasive blasting would damage the durability of the coating layer, as shown in Figure 1-1. Oxygen and moisture will permeate through the coating layer, then the residual contaminants act as solvents and inducing osmotic blistering. Eventually, the corrosion occurred and destroyed coating layer [2]. As a result, repainting processes would have to be carried out after several years of service [3][4].

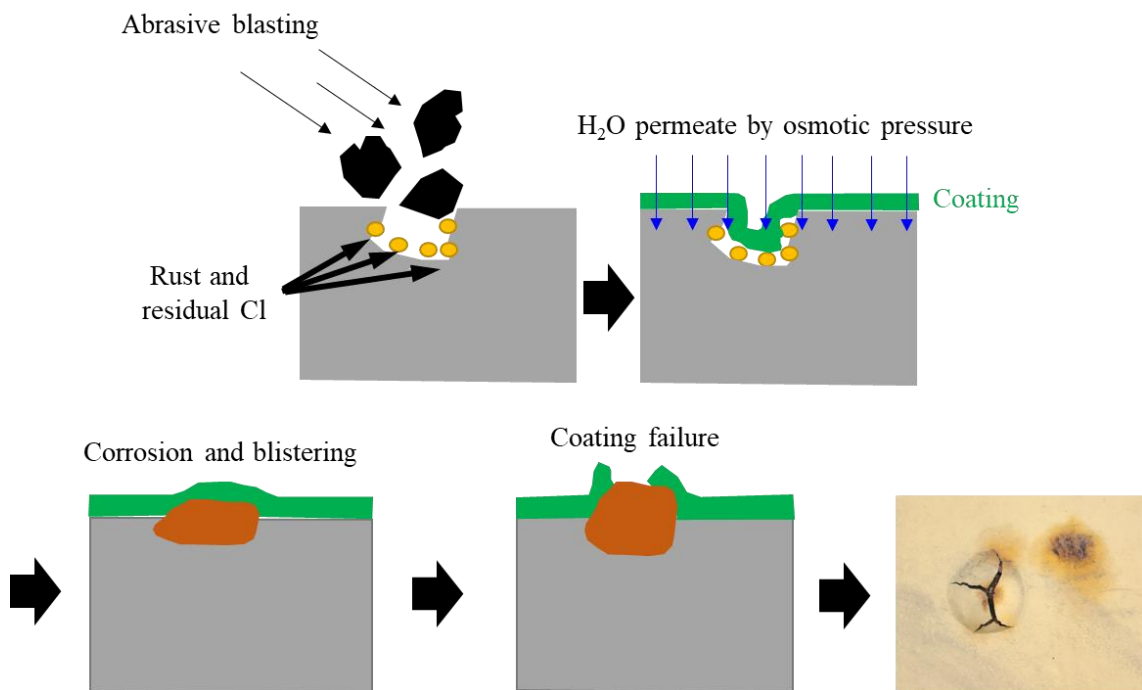


Figure 1-1 Coating failure due to insufficient surface preparation and underlying corrosion.

Among the widely used constructional steels, weathering steel (WS) are expected to have corrosion resistance due to protective corrosion layer formed on the surface [5].

However, some of the WS structure located in a highly corrosive environment by airborne sea salt may suffer from severe corrosion problems. Recent researches on WS corrosion had progressed on corrosion evaluation and prediction method [6], yet a practical surface preparation method for WS structure still lacks consideration. Figure 1-2 shows an example of severely corroded WS bridge. Layers of corrosion products appeared on the surfaces of truss frame and bolted joint, and pitting corrosion occurred underneath rust layers. Thus proper surface preparation is required for this kind of situation to maintain the durability of steel structure. Using the traditional abrasive blasting method, it is difficult to completely remove compact corrosion products formed on the weathering steel, not to mention the narrow positions where difficult to apply abrasive blasting.



Figure 1-2 Corrosion problem of weathering steel bridge.

To overcome these problems, laser cleaning has been drawing attention as an alternative surface preparation method. Laser cleaning has found successful applications in various fields [7][8][9]. Surface contaminants such as corrosion products, paint, and salt can be efficiently removed by laser cleaning. The mechanism of laser cleaning mainly contributes to the expansion and evaporation of contaminants on the steel surface. These effects are known as laser ablation [10]. Due to the high effectiveness of laser ablation, it had been adopted as a practical method for surface preparation in industrial production [11][12]. With enough laser output power, the compact corrosion products of weathering steel can also be removed. An example of surface salinity on corroded steel member before and after laser surface treatment is shown in Figure 1-3. The results after correction showed residual salts on the steel surface dropped from 156 to 1.3 mg/m². In addition, the standard requirement for residual salts in steel bridge field is 50 mg/m² according to Japanese Steel Bridge Anticorrosion Manual. Thus a desirable surface cleanliness is expectable through laser surface treatment.

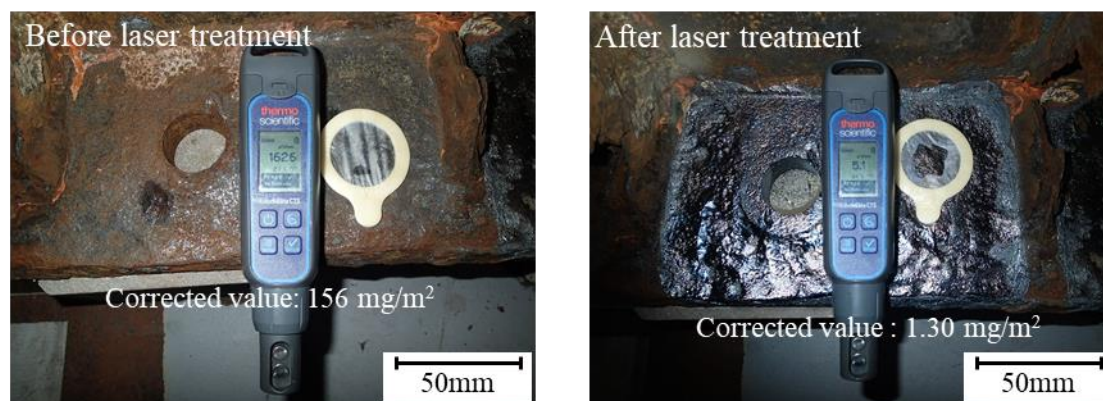


Figure 1-3 Residual salts on the steel surface before and after laser treatment.

Although various studies have been carried out to study the practicability and effects of laser treatment on the electrochemical and mechanical properties of metallic materials, these studies revolve around the industrial applications, of which, pulse laser is the most popular object of studies [13][14][15]. For the purpose of utilizing the laser surface treatment in larger objects, such as steel structures in the construction field, high treatment efficiency and effectiveness are essential requirements. In addition, the laser equipment should be optimized for hand-held operations to provide flexibility in practical applications. To date, few reports on high-power and high-efficiency laser treatment for large-scale structures have been presented. Compared to pulsed lasers, continuous wave (CW) lasers may be more appropriate for improving the treatment efficiency.

However, when using a high-power CW laser to clean a corroded structure, the laser beam will affect the base metal to a certain degree, owing to intense laser ablation effects and uncertainty in human operation. From the example of high-power CW laser cleaning shown in Figure 1-3. The laser treatment showed excellent cleaning effects for removing corrosion products and contaminants. Meanwhile, the appearance of the base metal suggested that the laser beam may also interact with the steel material below the corrosion products. The intense laser power will induce thermal effects on the steel surface, combined with the laser ablation effects, the surface morphologies, electrochemical and mechanical properties could be impacted. Thereby the concerns about durability and reliability of steel structures affected by the higher power CW laser, as well as the feasibility of this new technique should be evaluated carefully.

1.2 Objectives and scope

The primary objective of this dissertation is to evaluate the influence of thermal effects result from rotating CW laser on the surface and mechanical properties of carbon steel. To confirm the feasibility of this CW laser treatment for steel structures, surface properties, including surface morphology, iron oxide formation, electrochemical properties of the laser-treated steel plate, and the mechanical properties of carbon steel after laser irradiation should be established. Any possible defects on the surface or mechanical properties could damage the durability of steel structures during service. On the other hand, the surface properties give reference for decision of the following treatment, to remove laser-affected layer before coating, or just leave the layer even without coating. The dissertation specially focused on three laser parameters, which were power density, interaction time and the exclusive feature of rotating CW laser: laser beam overlapping effects. The thermal effects of CW laser beam were established by modifying the temperature calculation method, and experimental analysis on surface and mechanical properties. Surface morphologies and defects induced by laser irradiation were evaluated, as well as the performance degradation of mechanical properties under various laser conditions were also investigated. Proper laser treatment condition were proposed basing on the theoretical and experimental results.

This dissertation is organized basing on the objectives listed below:

- (1) Evaluate the thermal effects induced by rotating CW laser irradiation. To understand the thermal effects more specifically, temperature field during laser irradiation is an essential factor, especially peak temperature in the steel material during thermal circle. In this case, a widely used temperature field calculation method in CW laser treatment was adopted for modification. The laser beam overlapping effects resulted from rotation was taken into consideration during temperature field calculation. The calculated peak temperature field during rotating laser irradiation helps to explain resulting surface properties and microstructures. The appropriate laser processing parameters thereby suggested by the modified temperature calculation method.
- (2) Surface properties and the microstructures after CW laser treatment are directly impacted by thermal and laser ablation effects. Potential surface defects and

modification of microstructures could take place in the steel material and thereby impact the electrochemical and mechanical performances. With different laser processing parameters, the thermal and laser ablation effects may induced various degrees of influence. Thus the surface morphologies, oxide layer and microstructures were evaluated after laser irradiation, to establish relationship between laser processing parameters and surface properties, and identify the possible defects result from laser irradiation. Furthermore, a few cases in field application of rotating CW laser also considered, the proper moving speed of laser equipment and availability for steel surface with corrosion pit were confirmed.

- (3) The iron oxide and modified microstructures on laser-irradiated surface not only result in various surface morphologies, the electrochemical properties of carbon steel after laser irradiation could also been affected. The early corrosion behavior of laser-treated steel should yield the combination effects of oxide layer and modified microstructures. Furthermore, the integrity and amount of iron oxide can be further identified by the electrochemical test. Analysis on the electrochemical properties of the laser-treated steel surface helps to identify whether the surface condition is suitable for temporary storage, or even has the potential to act as protecting layers for steel structures.
- (4) Possible degradation in mechanical properties of steel material is another concern relating to high-power CW laser treatment. The surface defects caused by laser irradiation and modified microstructures could improve or reduce the mechanical properties of steel material. The reliability of steel structures is thereby another important objective for the application of high-power CW laser in field usage.

1.3 Literature review

1.3.1 Surface cleaning for corroded steel structures

Current surface cleaning method for steel rust including chemical and physical techniques. The chemical method usually use acid or alkaline solution to remove rust layer, in which the principle of acid solution is basing on the different dissolution rate between rust and steel material. The common acid solution for rust removal are hydrochloric acid [16], sulphuric acid [17], and tannic acid, etc. The advantage of chemical technique are the low cost and relatively high treatment efficiency, yet the base steel material could also been corroded by the acid solution [18]. On the other hand, the alkaline solution like sodium hydroxide and potassium hydroxide were also used for rust removal. Unlike the acid solution, alkaline solution combine with the ferric ion and separate the rust layer from base steel. Compare to the acid solution, alkali treatment have the similar efficiency and cost, however, no interaction with the base steel material can be expected. At the same time, application of chemical rust removal have environmental concerns. The waste liquid containing ferric ions, heavy metals and acid will lead to health hazardous and pollution [19]. The same problems can be found in the rust removal using alkaline solution. Besides the environmental concerns, the acid treated base steel will suffer flush rust more easily [20], which will be harmful for the following painting process. Therefore, chemical processing is not desirable in the field application.

Abrasive blasting is the most common surface cleaning method in construction field [21]. The corrosion products and contaminators are removed from the base steel material through the high pressure abrasive stream, meanwhile, underlying metal will been affected and resulting in surface microcutting [22]. However, the emission of rust products and abrasive materials will contaminate the environment. Especially copper slag or coal slag which might contain heavy metals and toxic substance [23], the collection for the abrasive materials is rather difficult to perform in the process of construction. Furthermore, more severe corrosion was identified after abrasive blasting due to the presence of surface microcutting [24], the reliability of abrasive blasting had been challenged by the environmental protection and durability issue.

To date, the surface cleaning method for corroded steel structures all have environmental or efficiency problems, more appropriate method with less emission and

higher efficiency are demanded. The laser surface treatment is another option for rust removal of steel structures, however, the research on this new technique is still lacking [1]. The advantages of laser treatment including environmental friendly, high treatment efficiency and applicability in the construction field. Furthermore, researchers suggested that the laser-treated steel material has no concerns for the flash rust after irradiation, due to the presence of passive layer. The difficulty of laser technique for the surface cleaning of steel structures is the high cost and electricity consuming [25]. There are still many obstacles to overcome in the development of laser surface treatment for steel structures.

1.3.2 Laser surface treatment

Basing on the output laser beam, there are two main types of laser equipment currently used in the surface preparation and industrial fields, which are pulsed-wave laser and continuous-wave laser. The power of laser intermittent output at given interval time are called pulsed-wave laser. Mode-locking, pulsed pumping and Q-switching are the most common controlling method for the pulsed-wave laser [26]. Pulsed laser are usually applied to surface texturing, fabricating of nanofilms, precision cleaning for the electronic component, or obtain biocompatible thin films [27]. On the contrary, the output power maintaining at a fixed value during the whole irradiation period are called continuous-wave laser. CW laser equipment usually cheaper and lighter than pulsed-wave laser because it does not need capacitor. Also, higher power and quicker energy output can be obtained in the CW laser [26]. They are commonly been used in the automobile and aerospace filed, for manufacturing purpose such as welding or drilling, or the painting removal [7]. The operating mode of pulsed-wave laser and continuous-wave laser is shown in Figure 1-4.

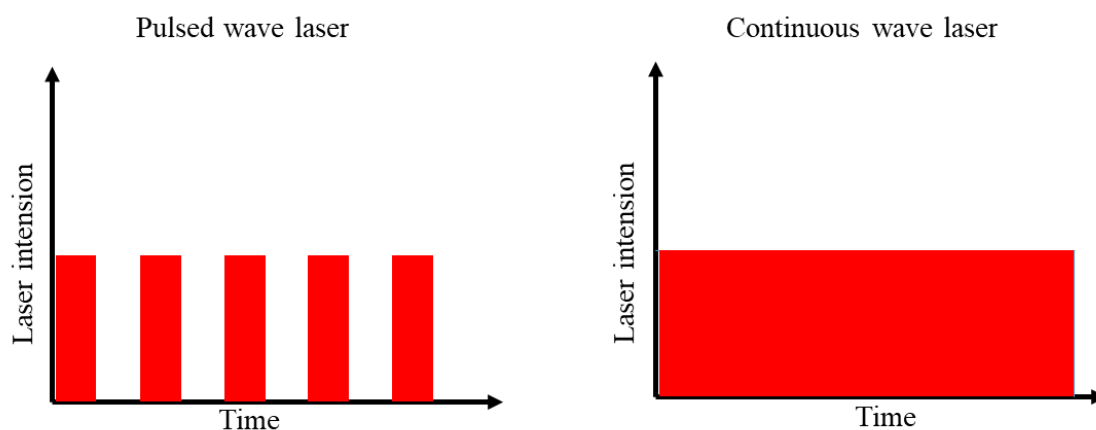


Figure 1-4 Output power and duration for the pulsed and continuous wave laser.

Laser surface cleaning is the process to remove contaminants remained on the substrate or coating layers [28]. Most of the current application of laser surface cleaning can be found in automotive industry [7]. Less environmental concerns and emission makes the laser cleaning has the possibility to replace traditional chemical cleaning method in the coating removal procedure [29][30]. With precise control of operation parameters in the pulsed-wave laser, the laser cleaning has the capability to remove coating laser without damage the substrate. In addition, the coating quality after laser cleaning was proved to have better adhesion attributed to smoother surface condition and finer microstructures on the laser-treated surface [7]. Besides the application in automotive industry, Zhou et al. [31] used a picosecond and nanosecond pulsed laser to clean the aluminum surface before welding. The results showed that both laser conditions can achieve desirable cleaning effects, thereby improving the welding quality. Zhang et al.[32] found that laser ablation was the predominant cleaning mechanism during low energy density. There are thresholds for initial cleaning and complete cleaning of Al alloys.

To date, the surface cleaning method using laser technology mainly adopt pulsed-wave laser as the output source. Indoor application for relatively small size of target is the current application status as mentioned above. Moreover, the low efficiency of pulsed wave laser may not applicable when targeting a large scale object (e.g. steel bridge). An appropriate laser-based cleaning technique for larger size structures is still lacking [1].

Although laser cleaning has the potential to achieve better surface conditions, higher scanning speed and laser power are required to improve the treatment efficiency when targeting a large structure. One of the major concerns of laser cleaning is that surface defects could result from laser irradiation. High-power laser treatment creates melt pools and heat-affected zone on material surfaces. In fact, laser additive manufacturing and laser welding relied on these thermal effects [33][34][35]. Therefore, the thermal effects on base material may affect mechanical properties [36][37]. When applying laser cleaning to a steel structure in the construction field, surface defects are undesired because they can give rise to stress concentration and decrease in fatigue lifetime [38]. Controlling the melting of base material during laser cleaning is required for practical applications to avoid detrimental phenomena [1].

1.4 Organization and outline

The dissertation is divided into six chapters, including this introduction.

In Chapter 2, the newly developed rotating CW laser equipment for surface treatment of corroded steel structures was introduced, main laser processing parameters were selected for following test and application. Then, a widely used temperature field calculation method for CW laser was adopted for modification, and the calculation method for peak temperature distribution along deepness direction in the steel material during laser irradiation was proposed. The modified peak temperature calculation method considered the overlapping effects of rotating CW laser beam, all the related parameters during laser processing were taken into the calculation. The surface morphologies and re-melted zone, heat-affected zone were observed in order to use as verification for the calculation method.

In Chapter 3, the surface properties and near-surface microstructure after laser irradiation were evaluated. The area suffered from more severe laser overlapping effects, and the average overlapping effects area was observed separately. Optical microscope and laser microscope were used for the surface morphologies and roughness inspection, SEM-EDX, XRD were adopted to observe the oxide layer on laser-treated steel surface. Relationship between laser processing parameters and the surface properties were established by comparing the test results referring to laser conditions. In addition, two cases that might be induced during the application of rotating CW laser in the construction field were also considered, to verify applicability of this new laser technique. Through the result, proper laser processing parameters were proposed.

In Chapter 4, the electrochemical properties of laser-treated steel plates were tested, including potential-time measurement, Potentiodynamic polarization test, and electrochemical impedance spectroscopy. The electrochemical test results were compared under different laser conditions, and associated with surface properties and modified microstructures. Changing corrosion properties and the iron oxide was further discussed in this chapter, to provide reference for following surface preparation procedure.

In Chapter 5, the tensile properties of steel coupon after laser irradiation were evaluated, together with the fractography after tensile test. The laser-treated steel coupon and unirradiated steel coupon were both tested under the identical monotonic tensile

condition. The test results were evaluated in association with surface properties discussed in Chapter 3. The influence of laser thermal effects on mechanical properties of steel coupon was established.

Chapter 6 summarized the work presented in this dissertation, future research topics emerged from this work were also proposed.

The flowchart of work in this dissertation is shown in Figure 1-5.

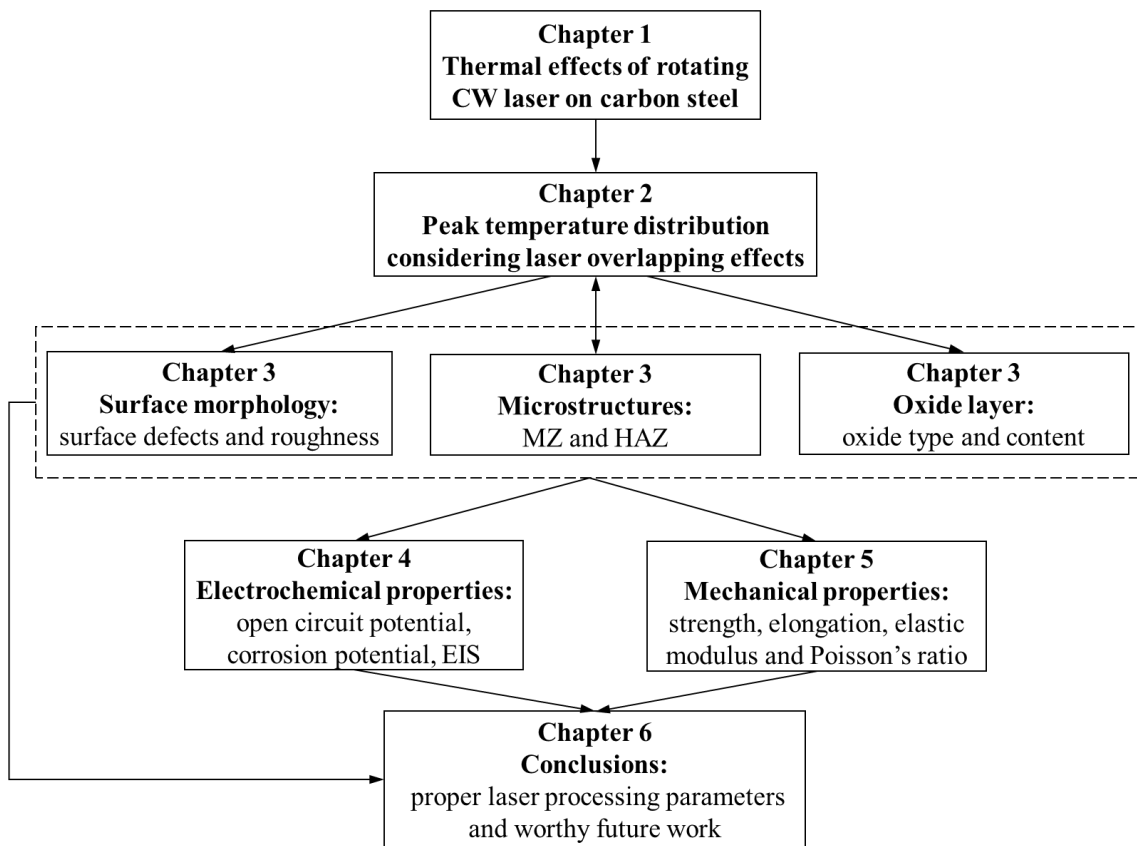


Figure 1-5 Flowchart of the dissertation.

CHAPTER 2 PEAK TEMPERATURE DISTRIBUTION IN STEEL MATERIAL DURING LASER IRRADIATION

2.1 Introduction

Analyzing the temperature field generated by a laser beam can help to evaluate the melting and laser ablation effects on materials. A numerical simulation method was proposed by Gao et al.[39] to investigate the temperature distribution law in molten pool during laser cladding. The simulation results described track dimensions and laser-induced temperature correctly in comparison to experimental results. The simulation method helped to optimize laser-processing parameters and reduce experimental costs. Lambiase and Genna [40] developed a finite element model to evaluate the effects of defocusing and position of laser beam on temperature field distribution. The results showed that laser beam defocusing reduces the temperature peak, and that the laser beam position can modify the thermal field. Nguyen et al.[41] investigated the temperature field and melt pool under different laser welding processing parameters. The measured temperature explained crack propagation and formation of an intermixing boundary of elements. The relationship between processing parameters with melt pool microstructure and defects was thus established. In addition to numerical simulation methods and experimental investigation, a calculation method developed by Ashby and Easterling[42] for describing the temperature field during laser irradiation was proved to achieve reasonable accuracy according to various studies [43][44][45][46]. Bendoumi et al.[43] evaluated the re-melted zone (MZ) and heat-affected zone (HAZ) in laser re-melted and laser-borided specimens. They also assessed the calculation results using equations developed by Ashby and Easterling. The calculation results showed good agreement with the experiments, confirming the feasibility of using these equations to estimate the thermal effects induced by laser treatment.

In this study, a newly developed CW laser was adopted as an alternative surface cleaning method for usage in the steel structures. The laser beam was rotated at given radius and speed to improve the treatment efficiency. In addition, frequent overlap of the laser beam was achieved during irradiation. This could contribute to higher thermal

effects on base material. Aiming at estimating the MZ in base material and optimizing laser-based cleaning processing parameters, equations by Ashby and Easterling were modified to consider the effects of overlap on the laser-induced temperature field. The calculation results were verified with an experimental method. Furthermore, surface morphologies of laser-treated specimens under different processing parameters were adopted to investigate the surface defects resulting from laser treatment. After laser treatment, the surface morphologies of laser-treated specimens were evaluated by optical microscopy (OM). The microstructures on the cross-section of specimens were observed after etching with 2 % nital to identify the MZ and HAZ.

2.2 Laser equipment and processing parameters used in this study

During laser surface treatment, the CW laser beam was rotated by a prism inside laser equipment, and projected to a target surface. The laser ring was manipulated to move at a given speed and direction until covering the entire area of the target surface, as shown in Figure 2-1. The laser-beam scanning speed v_B in Figure 2-1 refers to linear speed of rotation, and moving speed v_R describes the movement of the laser ring. There were two overlapping regions during laser treatment, as shown in Figure 2-1. In the processing of surface treatment specimens under given laser conditions, the laser ring overlapped 50 % of the ring diameter every time shift at vertical direction, the overlapping rate was calculated by dividing the overlapped width of laser ring by the ring diameter. The overlapping rate of the laser beam is represented by the ratio of overlapped width of laser beam and the beam diameter[47][48], which is changed with the processing parameters. Laser devices with power of 2 kW and 3 kW were used for surface treatment. The radius of laser beam r_B was 215 μm for 2-kW device, while 3-kW device operate at different r_B of 430 μm and 215 μm , labeled as LC and LD respectively. The rotation radius r_R of the 2-kW device was fixed at 5 mm, and for 3-kW devices, the radii were 10 mm and 13 mm for LC and LD conditions respectively. Various laser conditions with different scanning speed, rotation period, and moving speed were selected.

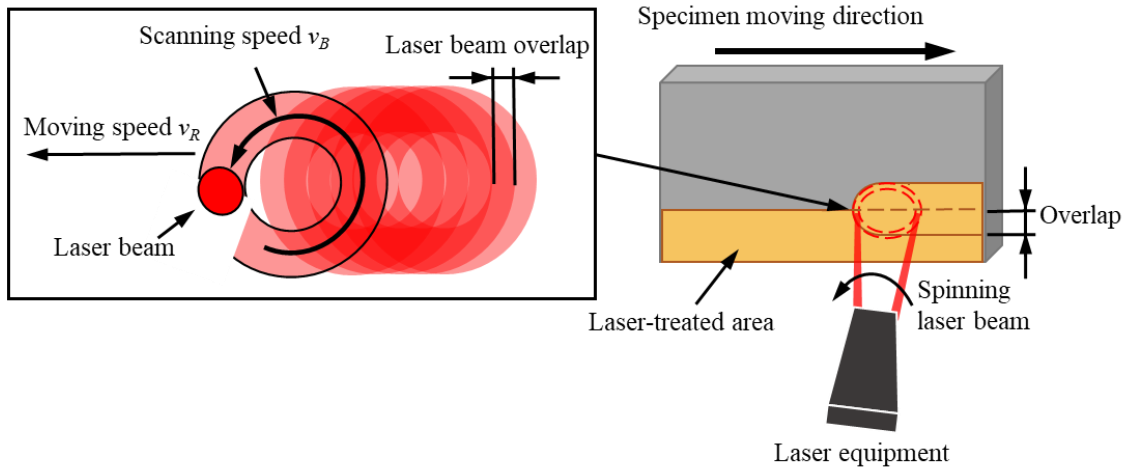


Figure 2-1 Schematic illustration of rotating CW laser treatment.

To identify the most important parameters for thermal effects of laser surface treatment, the laser power density (calculated by dividing the laser power by the area of the laser beam) and interaction time (defined as the beam radius divided by the scanning speed) were chosen based on references [42][43][49][50]. The overlapping rate of the laser beam was selected as the characteristic parameter of rotating laser beam. Processing parameters of laser conditions were shown in Table 2-1. Higher laser power density and longer interaction time contribute to more energy transfer from laser beam to steel material, and the laser beam overlap might enhance the thermal effects furthermore. The LA and LB treatment conditions were conducted with the 2-kW laser device, in which the LA condition exhibited longer interaction time. The LB and LC conditions had different laser power density, but similar interaction time and identical laser beam overlapping rate. The LD1, LD2 and LD3 treatment conditions were conducted with the same 3-kW laser equipment, where LD3 condition exhibited much higher laser beam overlapping rate.

Table 2-1 Processing parameters of different laser treatment conditions.

Laser condition	Power density q (kW·cm ⁻²)	Interaction time (μ s)	Laser beam overlapping rate (%)
LA	1377	103	50
LB	1377	58.6	50
LC	516	58.7	50
LD1	2066	31.6	50
LD2	2066	31.6	75
LD3	2066	31.6	86

The laser power density were all Gaussian distribution, where LA and LB conditions had the same laser power distribution, LC condition had the largest beam size and lowest peak value of power density. LD1, LD2 and LD3 conditions had the same laser power distribution and highest peak value, as shown in Figure 2-2.

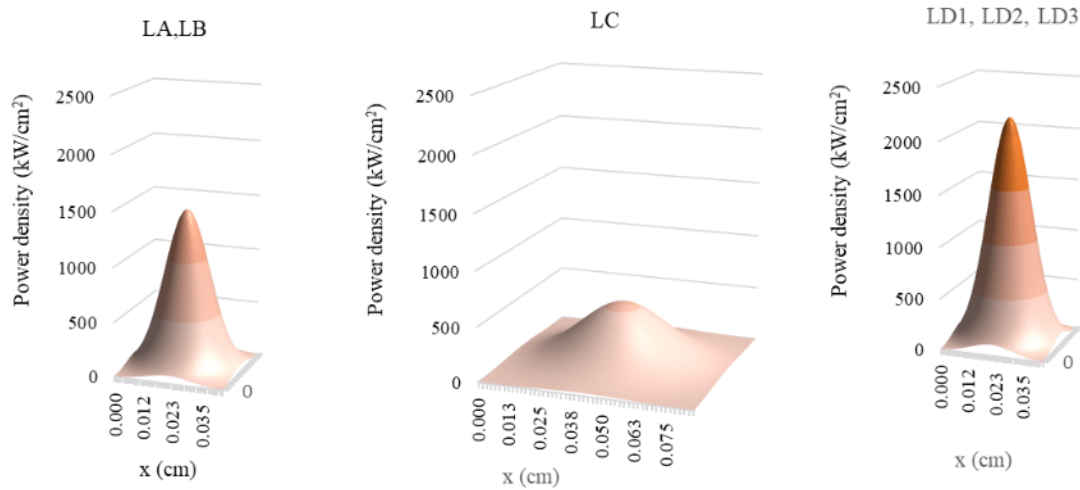


Figure 2-2 Laser spot size and energy distribution for different laser conditions.

2.3 Analytical equations for temperature field produced by CW laser

When a CW laser beam is applied to the surface of a solid, the material is heated by absorb the laser energy. The temperature field produced by the laser irradiation must satisfy the equations of heat flow. Assuming the thermal properties of the material do not affected by the temperature, the governing differential equation is:

$$\nabla^2 T - \frac{1}{\alpha} \frac{dT}{dt} + \frac{q_v}{\lambda} = 0 \quad (2-1)$$

where α is the thermal diffusivity, λ is the conductivity, and q_v the rate at which heat is supplied to the solid per unit time and volume. For a CW laser beam with energy q and radius R_b , scanning the semi-infinite solid surface with velocity v_B (that is, solutions describing a laser beam tracked across the surface of a solid), the solutions are in the form of difficult integrals or multiple integrals. Which are too cumbersome to allow the analysis of a CW laser. This problem is overcome by Ashby and Easterling [42] through developing an approximate solution to the same laser thermal problem. The accuracy of

this approximated method was verified by comparing to integral solutions.

The total power in the beam of laser irradiation is considered a cylindrical beam of radius r_B delivering a power density $q_s(x, y)$:

$$q = \int_0^{\infty} \int_0^{\infty} q_s dx dy \quad (2-2)$$

in case of a Gaussian power density:

$$q_s = q_{max} \exp - \left(\frac{x^2 + y^2}{r_B^2} \right) \quad (2-3)$$

r_B is the distance from the beam center at which the power density has fallen to $1/e$ of q_{max} .

The temperature field caused by a point source can be written:

$$T = T_0 + \frac{Aq}{2\pi\lambda r} \exp - \left\{ \frac{v_B}{2\alpha} (x + r) \right\} \quad (2-4)$$

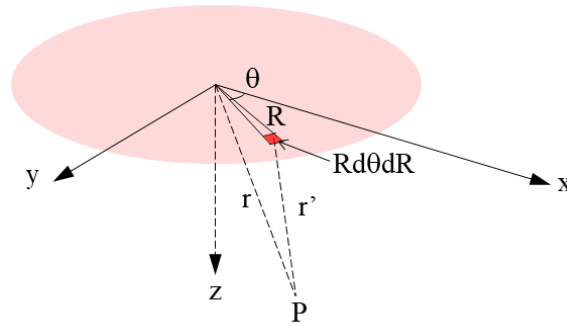


Figure 2-3 The geometry of the integral method for calculating the heat cycle at the point P.

The diffuse laser beam is now divided into small segments of area $Rd\theta dR$, as shown in Figure 2-3. Then the temperature field can be calculated by integrating. At a point P

below the surface:

$$T = T_0 + \int_0^\infty \int_0^{2x} \frac{Aq}{2\pi\lambda r'} \exp - \left\{ \frac{v_B}{2\alpha} (x' + r') \right\} R dR d\theta \quad (2-5)$$

where

$$x' = x - R \cos\theta \quad (2-6)$$

and

$$r' = [(x - R \cos\theta)^2 + (y - R \cos\theta)^2 + z^2]^{1/2} \quad (2-7)$$

The calculation here is too slow for the scanning CW laser beam, in this case, Ashby and Easterling developed an approximate calculation method for the temperature field. Assuming a diffuse beam with a Gaussian energy distribution, scanning in the x direction with velocity v_B . When the velocity v_B of the beam is high enough, it can be equivalent to a line source with finite width and infinitesimally small length. An analytical solution for the temperature field $T(y, z, t)$ is written:

$$T = T_0 + \frac{Aq/v_B}{2\pi\lambda[t(t+t_0)]^{1/2}} \exp - \frac{1}{4\alpha} \left\{ \frac{z^2}{t} + \frac{y^2}{t+t_0} \right\} \quad (2-8)$$

where

$$t_0 = \frac{r_B^2}{4\alpha} \quad (2-9)$$

That is a major change of equation (2-4) which separate laser beam heat in y direction. The new parameter t_0 is simply the time taken for heat to diffuse over the beam radius, r_B . For calculation point far from the heat source where $z^2 + y^2 \gg r_B^2$ and $t \gg t_0$, the equation reduces to the result for a point source. But this equation leads to infinite temperatures at the surface encountered with laser beam. Due to the line source assumption means that energy is injected into the solid at $t=0$. In purpose of describing laser surface treatment approximately, the width of the beam in both the x and y directions

must be considered.

To do so, Ashby et al. assume that the laser beam has radius r_B , then energy is injected at a given point on the surface over a interaction time:

$$t_B = \frac{r_B}{v_B} \quad (2-10)$$

The interaction time describe heat conduction on the solid surface, not only injected from the laser beam, but also draining away by the underlying material. Therefore, the surface temperature can be limited to a finite value. Ashby et al. allow for this by replacing the real source in the plane $z = 0$ by an apparent source in the plane $z = z_0$ above the surface, so that:

$$T = T_0 + \frac{Aq/v_B}{2\pi\lambda[t(t+t_0)]^{1/2}} \exp - \frac{1}{4\alpha} \left\{ \frac{(z+z_0)^2}{t} + \frac{y^2}{t+t_0} \right\} \quad (2-11)$$

or immediately below the center of the beam, $y = 0$:

$$T = T_0 + \frac{Aq/v_B}{2\pi\lambda[t(t+t_0)]^{1/2}} \exp - \left\{ \frac{1}{4\alpha} \frac{(z+z_0)^2}{t} \right\} \quad (2-12)$$

The heating and cooling rate are given by differentiating with respect to time:

$$\frac{dT}{dt} = \frac{T - T_0}{t} \left\{ \frac{(z+z_0)^2}{4\alpha t} - \frac{1}{2} \left(\frac{2t+t_0}{t+t_0} \right) \right\} \quad (2-13)$$

The first term in the brackets describes heating; the second describes cooling. The peak temperature, T_p , is at the point $dT/dt = 0$, when:

$$\frac{t(2t+t_0)}{(t+t_0)} = \frac{(z+z_0)^2}{2\alpha} \quad (2-14)$$

Two limits were taken into account to evaluate z_0 .

(1) The limit $t \gg t_0$. In this limit the equation (2-14) simplifies to

$$t = \frac{(z + z_{02})^2}{4\alpha} \quad (2-15)$$

and the peak temperature is

$$T_{P1} = T_0 + \frac{2Aq/v_B}{e\pi\rho c(z + z_{01})^2} \quad (2-16)$$

when $z \gg z_{01}$ which reduces to the Rosenthal equation for a point source scanning across a thick plate.

The depth at which a given peak T_{p1} is reached:

$$z + z_{01} = \left(\frac{2}{\pi e}\right)^{1/2} \left\{ \frac{A(q/v_B r_B) r_B}{\rho c (T_{P1} - T_0)} \right\}^{1/2} \quad (2-17)$$

To determine z_{01} , a fixed laser beam with intensity of $q/\pi r_B^2$, applied for a time t_B , produces a peak surface temperature T_s given by:

$$T_s = T_0 + \frac{2Aq}{\pi^{3/2} r_B^2 \lambda} \{\alpha t_B\}^{1/2} \quad (2-18)$$

Equating this to equation (2-16) with $z = 0$ gives:

$$z_{01}^2 = \left(\frac{\pi^{1/2}}{e}\right) \left\{ \frac{\alpha r_B}{v_B} \right\}^{1/2} r_B \quad (2-19)$$

The cooling rate beyond the peak also means the first term in equation (2-13) is negligible:

$$\frac{dT}{dt} = -\frac{2\pi\lambda(T - T_0)^2}{A(q/v_B)} \quad (2-20)$$

(2) In limit of $t \ll t_0$, the equation (2-8) beacomes:

$$t = \frac{(z + z_{02})^2}{2\alpha} \quad (2-21)$$

and the peak temperature is

$$T_{P2} = T_0 + \left(\frac{2}{e}\right)^{\frac{1}{2}} \frac{Aq/v_B}{\pi\rho cr_B(z + z_{02})} \quad (2-22)$$

and the depth at which a given peak T_{p2} is reached:

$$z + z_{02} = \left(\frac{2}{e}\right)^{\frac{1}{2}} \frac{Aq/v_B r_B}{\pi\rho c(T_{P2} - T_0)^2} \quad (2-23)$$

equating equation (2-21) to equation (2-18) gives z_0 , in this limit, as:

$$z_{02}^2 = \left(\frac{\pi}{2e}\right) \left(\frac{\alpha r_B}{v_B}\right) \quad (2-24)$$

the cooling rate beyond the peak is:

$$\frac{dT}{dt} = -\frac{\pi^2 \lambda \rho c (T - T_0)^3}{2[A(q/v_B r_B)]^2} \quad (2-25)$$

For a laser beam with energy q and radius r_B , the calculation method can be used to exam whether the laser energy inducing surface melting or contribute the surface temperature to exceed a critical value T_c . From the equation (2-16) this is:

$$\frac{q}{v_B r_B} = \frac{\pi^3}{4} \left[\frac{(T_c - T_0) r_B}{A} \right]^2 \frac{\lambda \rho c}{q} \quad (2-26)$$

Ashby et al. demonstrate that this new approximation (2-8) for the temperature field $T(y, z, t)$ of a CW laser beam gives more precise solutions for temperature field

calculation. Furthermore, the approximate field equation (2-12) is verified with the double-integral equation (2-5). Desirable result can be obtained through this simplified calculation method.

The peak temperature of equation (2-12) is always close to the smaller of equation (2-16) and (2-22) and is well approximated by:

$$T_p(z) = \frac{(T_{p1} + T_{p2})T_{p1}T_{p2}}{T_{p1}^2 + T_{p2}^2} \quad (2-27)$$

Equations (2-12) and (2-27) describe temperature field and peak temperature distribution below the center of laser beam. Some assumptions were applied for the approximate peak temperature calculation:

(1) Physical properties such as absorptivity A , material density ρ , specific heat c , and thermal conductivity λ were deemed constant during laser treatment;

(2) Ambient temperature was also deemed constant and kept at 293 K.

The accuracy of these equations had been verified with experimental results in the works of Bendoumi et al. [43]. However, these solutions did not consider the overlapping effects. As for rotating laser surface treatment used in this study, the temperature field in overlapped area may differ from single path laser scanning, especially for frequent overlapping irradiation. The temperature field under laser beam may superposed within heating and cooling circle, result in improving peak temperature during laser irradiation.

As for purpose of heat effects evaluation during laser treatment, the peak temperature among laser irradiation is the key factor for discussion of laser ablation, microstructure of steel material and surface morphologies after laser treatment. Therefore, to simplify calculation method, and also for practical purpose in this study, only the peak temperature calculation equations of steel material during laser irradiation was investigated.

2.4 Calculation for peak temperature distribution of rotating CW laser

2.4.1 Peak temperature distribution considering laser beam overlapping effects

The thermal circle during laser irradiation are rapid process [51] that usually in millisecond scale. To visualize the heat and cooling speed during CW laser treatment, the

laser conditions adopted in this study are used to calculate the approximate temperature-time curves base on equation (2-12). The calculation considered center portion on the surface of carbon steel encountered with CW laser beam. The laser energy injected into the surface during interaction time, inducing heating process at the calculation portion, and then cooling process take place with leaving laser beam, as shown in Figure 2-4. Carbon steel of SM490A basing on JIS G3106 are chosen as the target material, physical properties of SM490A are listed in Table 2-2. The calculation here only considered a single laser scanning track without overlapping effects. The scanning track within a heating and cooling circle are treated as line source in consideration of extremely fast moving speed and negligible laser beam diameter.

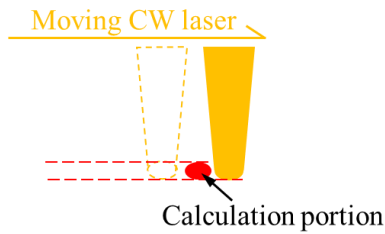


Figure 2-4 Schematic illustration of calculation portion and period for the temperature-time curves.

Table 2-2 Physical properties of SM490A carbon steel used for laser treatment.

	Density ρ (kg·m ³)	Specific heat c (J·kg ⁻¹ ·K ⁻¹)	Thermal conductivity λ (W·m ⁻¹ ·K ⁻¹)	Absorptivity A
SM490A	7850	422	45	0.36

The temperature-time results of various laser conditions are described in Figure 2-5, as the LD1, LD2 and LD3 are using the same parameters but different laser ring moving rate, the heat effects of these conditions are the same within single scanning track. The temperature of steel surface at the center of laser beam are improved rapidly, and reach the peak temperature in under 0.1 ms. From the partial enlarged detail around 0 to 0.3 ms, the highest peak temperature are reached in LA condition, created 4860 K in approximate, followed by LD condition of 4136 K and LB condition of 3739 K. The LC condition possessed lowest peak temperature value of around 1600 K. Thus it can be seen that

temperature result from CW laser irradiation are related to combined action of laser parameters. Higher laser output power does not mean higher temperature induced on the steel surface, because the beam diameter limits the power density, which means smaller beam owns higher power density and more potential for significant laser heat effects. On the other hand, scanning speed of laser beam determined the interaction time of steel surface and laser beam, higher speed restrict the time for steel surface to absorb laser energy, thus lead to lower heat effects. However, when the laser beam leaving from calculation portion, cooling process are taken into place and the cooling rate of all the laser conditions are extremely fast, just like heating process. After 3 ms of the thermal circle, temperature of all the laser conditions tend to be stable at a certain values, which still higher than the initial temperature of 293 K (ambient temperature). Noticing that the rotation period of laser conditions are range from 9 to 15 ms, it is nonnegligible that the temperature between rotation period of laser beam could superposition and further improve the initial temperature before a new rotation circle.

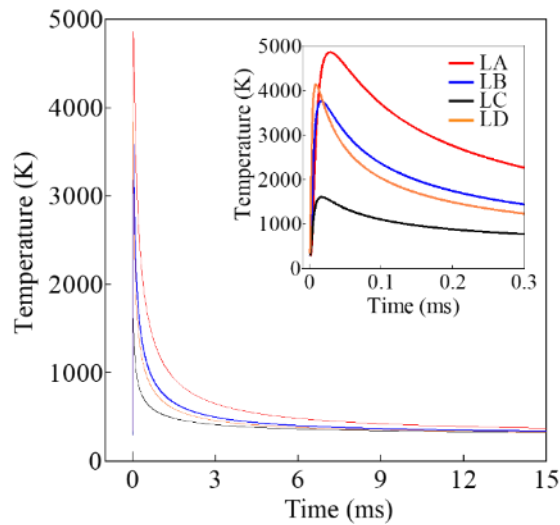


Figure 2-5 Temperature-time curves of laser conditions used in this study for carbon steel SM490A.

To take the overlapping effects of rotating laser beam into consider of temperature field calculation, heating and cooling circle is the critical factor since temperature would accumulate before cools down. Equations (2-11) and (2-12) describe the heating and

cooling circle during laser irradiation. The cooling process is dominated by thermal conduction of the material as the laser beam moves away. Moreover, the thermal circles are unsynchronized along the depth direction, which means that a deeper layer may still be undergoing a heating process while the upper layers begin to cooling. Generally, the overlapping effects on temperature distribution can be attributed to the accumulation of initial temperature due to repetition irradiation. The second term in equations (2-11) and (2-12) describes temperature evolution with time-lapse. Assuming that the temperature field is dominated by the heating effects of subsequent irradiation, the initial temperature before a repetition irradiation should be the accumulation of temperature increment of previous repetition irradiations. For laser irradiation with overlapping process, the temperature increment at the beginning of the last repetition irradiation n can be derived from equation (2-12) as follows:

$$T_{n-1}(z) = T_0 + \sum_{i=1}^{n-1} \frac{Aq}{2\pi\lambda v_B \sqrt{[t_i(t_i + t_0)]}} \exp\left[-\frac{(z + z_0)^2}{4\alpha t_i}\right] \quad (2-28)$$

where T_0 is the initial temperature (K), which usually refers to the ambient temperature; n is the number of repetition irradiation in an overlapping region; and t_i is the time interval of each repetition irradiation (s).

Then, the initial temperature for the last repetition irradiation n is replaced by $T_{n-1}(z)$, and the temperature distribution of the last repetition irradiation is given by the following expression:

$$T_n(z, t) = T_{n-1}(z) + \frac{Aq}{2\pi\lambda v_B \sqrt{[t(t + t_0)]}} \exp\left[-\frac{(z + z_0)^2}{4\alpha t}\right] \quad (2-29)$$

Therefore, the peak temperatures of T_{p1} and T_{p2} within two limits are expressed as follows:

$$T_{P1}(z) = T_{n-1}(z) + \frac{Aq\sqrt{2/e}}{\pi\rho c v_B r_B(z + z_{01})} \quad (2-30)$$

and

$$T_{P2}(z) = T_{n-1}(z) + \frac{2Aq}{e\pi\rho cv_B(z + z_{02})^2} \quad (2-31)$$

Finally, the peak temperature distribution considering overlapping effects can be obtained by substituting the results of equations (2-30) and (2-31) into equation (2-27).

2.4.2 Application of approximate calculation method for rotating CW laser treatment

The laser treatment used in this study was a rotating laser beam that traveled with the movement of the rotation center. Consequently, there were various overlapping areas including laser ring and beam overlaps, as illustrated in Figure 2-1. However, the time interval of laser ring overlap was in the range of 3–30 s, depending on the moving speed of the laser ring. For laser beam overlap, the time interval was approximately equal to the rotation period, which was in the order of milliseconds. Considering the extremely fast cooling rate during laser irradiation (approximately 10^3 – 10^8 K/s)[51][52], the thermal effects of repetition irradiation were dominated by a laser-beam overlapping process. Therefore, the laser-ring overlapping effects were ignored in the temperature calculation.

The combination of rotating laser beam and moving laser ring produced non-uniform overlapped areas, as shown in Figure 2-6 (a). The concept of diagrammatic drawing here was employed to compare the overlapped areas at each position within one rotation period separately. In this case, the laser beam returned to its previous spot with horizontal displacement owing to the movement of the laser ring. When the laser beam reached the middle position of the laser ring, the overlapped area contained both the traveled and covered areas, denoted as A_1' and A_1 in Figure 2-6 (a), respectively. Similarly, the overlapped area at top position was composed of A_2' and A_2 . It is evident that the scanning laser beam traveled through a previously irradiated area within a rotation period, causing repetition irradiation. The same effects took place at any position of the laser ring because the scanning speed v_B was much faster than the moving speed v_R . Therefore, a rotating laser beam creates different overlapped areas during irradiation, even if the laser ring moves at a certain speed. In the example here, the overlapped areas fulfilled the inequality $A_1 < A_2$.

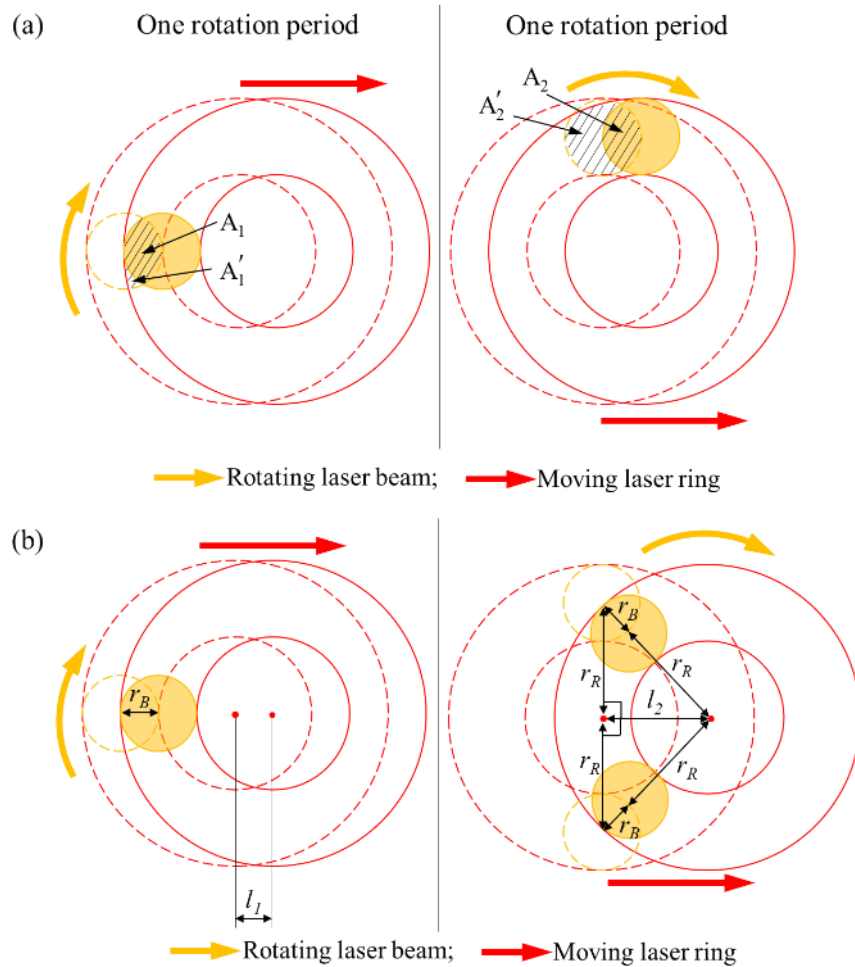


Figure 2-6 Diagrammatic drawing of overlapped areas during rotating laser irradiation.

Although it was difficult to consider varying overlapped areas in the calculations, the number of repetition irradiation n in equation (2-28) was easier to obtain. Note that the overlapped areas at each repetition irradiation decreased with the movement of the laser ring. In a study by Ashby and Easterling [42], the interaction time of the laser beam was defined as the beam radius divided by the scanning speed owing to the low-power density around the edge of the laser beam. To decide the number of repetition irradiation n , the varying overlapped areas during repetition irradiation were assumed to possess the same thermal effects until the overlapped width exceeded the beam radius r_B , as shown in Figure 2-6 (b). It is evident that the overlapped width at middle position started to exceed the beam radius when the laser ring displacement l_1 equaled r_B . However, a longer displacement l_2 was required for top and bottom positions. Here, the top/bottom and

middle positions were selected to calculate the peak temperature distribution as representatives of maximum and minimum temperature values, respectively. For fixed rotation period t_R and moving speed v_R , the number of repetition irradiation n is expressed as follows:

$$n = \frac{l}{v_R t_R} \quad (2-32)$$

where l is the displacement of the laser ring when the overlapped width of the laser beam equals the beam radius (m); v_R is the moving speed of the laser ring ($\text{m}\cdot\text{s}^{-1}$); and t_R is the rotation period of the laser beam (s).

According to Figure 2-6 (b), the displacement of the laser ring l at middle position is given by the following expression:

$$l_1 = r_B \quad (2-33)$$

The top/bottom position has an l expressed as follows:

$$l_2 = \sqrt{(r_B + r_R)^2 - r_R^2} \quad (2-34)$$

Note that the interval time t_i in rotating laser treatment is a fixed value and equals the rotation period t_R . Therefore, equation (2-28) can be simplified as follows:

$$T_{n-1}(z) = T_0 + (n - 1) \left\{ \frac{Aq}{2\pi\lambda v_B \sqrt{[t_R(t_R + t_0)]}} \exp \left[-\frac{(z + z_0)^2}{4\alpha t_R} \right] \right\} \quad (2-35)$$

Then, the peak temperature distribution can be obtained from equations (2-30), (2-31), and (2-27).

2.4.3 Verification of analytical equations for peak temperature distribution produced by rotating CW laser

Carbon steel plates (JIS G3106 SM490A) were used as the irradiation target for verification analysis. The dimensions of steel plates were 150×70×6 mm. Before laser

treatment, steel plates were pretreated by abrasive blasting to remove the mill scale on surface and also to reduce the laser reflectivity [53] and create similar surface conditions for irradiation targets. During laser treatment, the steel plates remained perpendicular to the ground, and fixed at an XY-axis motorized stage and moved in a given direction and speed to acquire designed laser parameters, as shown in Figure 2-7. At the meantime, the rotational axis of the laser beam was kept parallel to the ground. After laser treatment, the surface morphologies of laser-treated specimens were evaluated by optical microscopy (OM), and the surface roughness was measured with a laser microscope. The microstructures on the cross-section of specimens were observed after etching with 2 % nital to identify the re-melted zone (MZ) and heat-affected zone (HAZ).

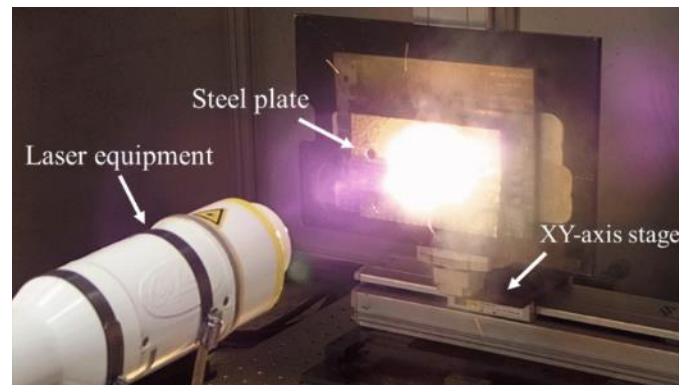


Figure 2-7 Experimental setup of laser irradiation using XY-axis motorized stage.

The surface conditions of specimens after rotating CW laser irradiation are shown in Figure 2-8. Region A (blue zone) represents the area with minor overlapping effects. It refers to the middle position as described in the previous section, while Region B (green zone) represents the top/bottom positions with the highest overlapping effects. Basically, Region B appeared as the boundary of the overlapped laser ring paths. No evident differences in surface appearance could be observed from the photos of LA and LB specimens, both conditions revealed surface morphologies with clear laser scanning paths, and obvious overlapped boundaries. Implying the temperature distributions of these two laser conditions may trigger severe laser ablation effects. When using LC condition, which also represent the lowest laser output power density, result in a surface condition with less features of overlapped laser boundary. Meanwhile, the line at Region B appears to be more flat instead of sags and crests. On the other hand, the laser ring moving speed

are decreased in LD2 and LD3 conditions, which means more overlap times during the laser irradiation. As a result, the specimens presented a wider Region B in comparison to the LD1 specimen. In addition, all of the laser-treated steel surfaces presented oxide luster, implying possible oxidation induced by the laser beam. Among the specimens, LC and LD1 conditions revealed even bluer surface luster, while the other conditions contribute to a darker surface luster. The change of surface luster suggesting a different levels of laser heat effects under different operating parameters.

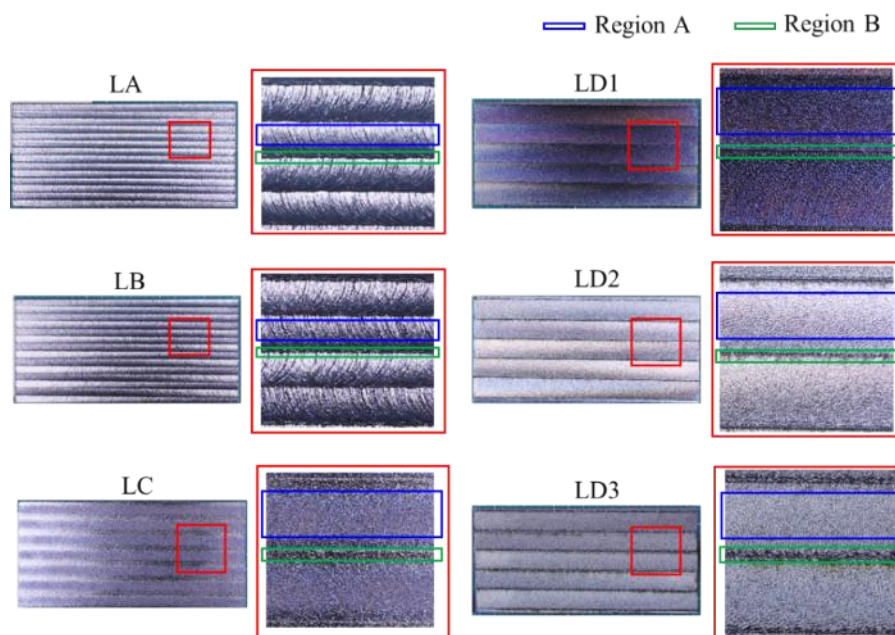


Figure 2-8 Surface conditions of laser-treated specimens.

The OM surface morphologies of specimens are shown in Figure 2-9. In Region A of LA, LB and LD1 specimens, the rotation paths of the laser beam were observed, while LC specimen presented no obvious laser scanning tracks, except for craters formed on the steel surface. Less laser scanning tracks might be attributed to lower power density and fast laser beam moving speed, hence the amount of heat transfer was limited by the power supply and interaction time. The surface morphologies of the LD2 and LD3 specimens were significantly different from LD1 specimen. A rougher surface without clear rotation paths were presented in the LD2 and LD3 specimens. Note that the LD2 and LD3

conditions had the slower moving speeds. Therefore, the overlapping effects could be significantly improved according to equation (2-32), and higher roughness was achieved. Micrographs of the cross-section under the LA, LB and LC conditions show smoother surfaces than those of LD1, LD2 and LD3 specimens. However, no distinct surface defects were observed in Region A of all specimens.

The OM morphologies of LA, LB, LD1 and LD2 specimens in Region B clearly showed the boundary between laser ring paths; note that the rotation path of the laser beam at top/bottom positions was perpendicular to the middle position. While the LC specimen presented most flat and smooth surface features than the other laser conditions, this might be the result of minimal thermal effects. Concerning the LD3 specimens, the boundary vanished and was replaced by an extremely irregular bulge. Micrographs of the cross-section clearly show the outstanding bulges that appeared under LD2 and LD3 conditions; micro cracks were also found in the bulge area. In contrast, smaller bulge was found in the LD1 specimen, which also represent the faster laser ring moving speed in LD conditions. Generally, a bulge structure is considered as the result of ripples, undercuts, step structures, and martensite needles induced by laser irradiation [54], but the sizes of bulge attributed to these reasons were very small, as a-a and b-b cross-sections show in Region B. Therefore, the outstanding bulges in LD2 and LD3 specimens could also result from improving the overlapping effects. In this case, the specimen surface absorbs more laser energy, thereby leading to a larger melt pool. The steel plates were perpendicular to ground during laser treatment. Hence, liquid flowing of melt pool may occur before resolidification, resulting in outstanding bulges formed in Region B, as shown in Figure 2-10.

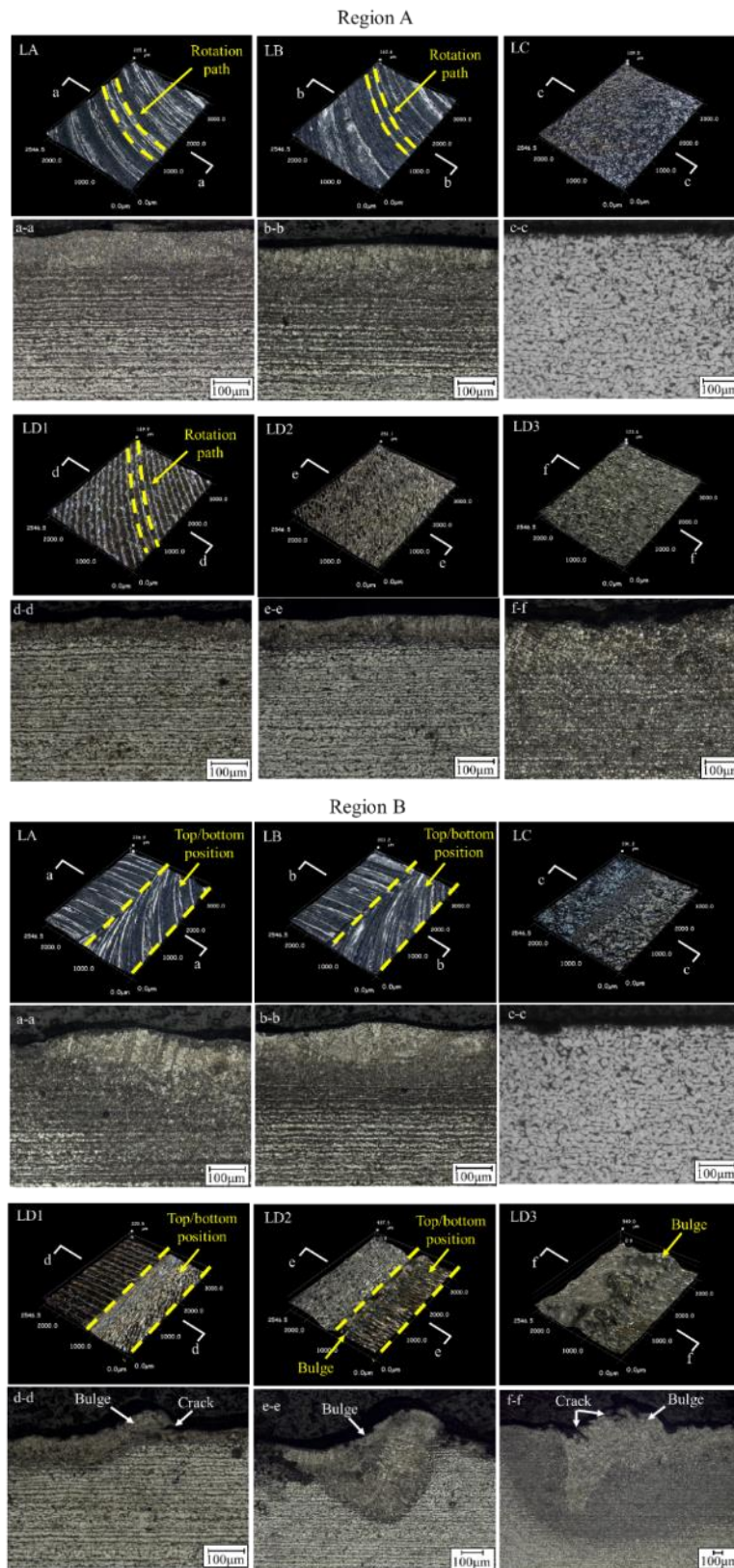


Figure 2-9 OM surface morphologies and microstructures on cross-section of laser-treated specimens at Region A and Region B.

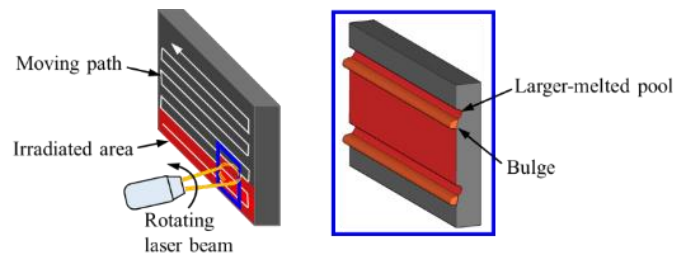


Figure 2-10 Schematic illustration of laser-melted pool and bulge formation.

Figure 2-11 shows the microstructures on cross-sections perpendicular to the laser ring moving direction. A layer-laminated microstructure was observed in the non-irradiated specimen. This structure represents the initial microstructure of steel plates before laser treatment. When the surface of the material underwent a melting process, the original layer-laminated microstructure disappeared and reformed the MZ [55], as shown in Figure 2-11. Furthermore, a certain depth of material below the MZ was also impacted by thermal effects and created the HAZ, which consisted of a refined layer-laminated microstructure. Note that the depth of the MZ improved when decreasing the scanning speed according to the LA and LB specimens. By contrast, microstructures of the LD1, LD2 and LD3 specimens indicated that a slower moving speed of the laser ring also contributed to the MZ formation. The MZ of laser-treated specimens in Region B was deeper than that in Region A, in which the LD2 and LD3 specimen presented an extraordinary improvement in the MZ. On the other hand, the microstructure of LC specimens presented no indication of MZ or HAZ. The least thermal effects was observed under LC condition, which is consistent with the surface observation results in Figure 2-8 and Figure 2-9. The calculated peak temperature distribution in the following section further explains the evolution of the MZ in laser-treated specimens.

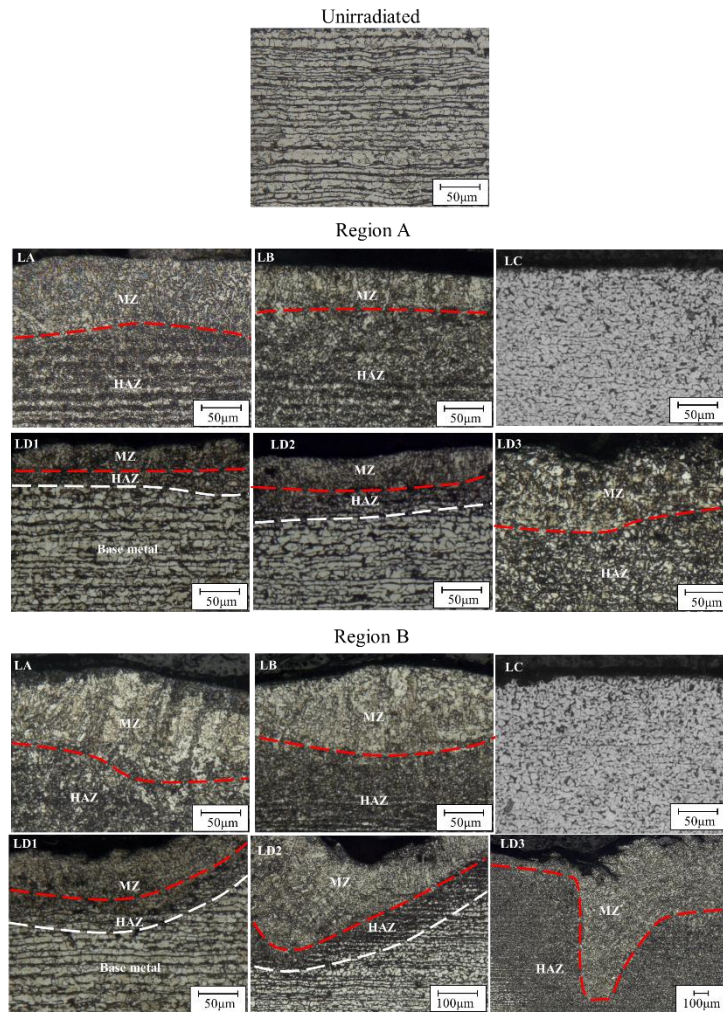


Figure 2-11 OM cross-section of unirradiated and laser-treated specimens.

The number of repetition irradiation n for various laser treatment conditions according to equation (2-32) is listed in Table 2-3. The repetition irradiation at the middle position of the laser ring was chosen to represent Region A. The results verified that more repetition irradiation took place in Region B, where the LD3 specimen possessed the largest number of repetition irradiation, followed by the LD2 specimen. The calculated peak temperature distributions of laser-treated specimens are presented in Figure 2-12. The theoretical results are compared with the MZ in the OM microstructure to verify the accuracy of the calculation method. A melting point of 1698 K [56] for SM490A carbon steel was adopted to identify the MZ in calculated results; a boiling point of 3273 K[57] is also illustrated in the graph as a reference to evaluate laser-induced thermal effects.

According to Figure 2-12, the MZ obtained from the calculation method is in good agreement with the MZ in the OM microstructure. The results for Region B corroborated the suitability of this calculation method, providing a good indication of the overlapping effects. By contrast, the OM microstructure presented a slightly deeper MZ than that from the calculated results. In real situations, the surface material would start evaporation once the temperature exceeds the boiling point. Note that the peak temperature near the surface exceeded the boiling point in all laser conditions except for LC conditions, as shown in Figure 2-12. In this case, part of the surface material will be removed owing to laser ablation effects [58] and the liquid flow of melt pool. Then, the underlying layer was exposed to the laser beam directly, thereby leading to deeper MZ formation. Besides, increasing the material temperature also resulted in higher laser absorptivity, and hence the thermal effects further improved [59]. As for LC condition, the calculation method also revealed a suitable results to explain the less laser tracks appearance on the surface observation in Figure 2-9. Laser-induced surface peak temperature just exceed the melting point of steel material, therefore the laser ablation effects are restricted under this circumstance. A melting dominate effects rather than ablation effects are taken in place under LC condition. To assess the accuracy of the calculation method quantitatively, the MZ depth in Region A and maximum MZ depth in Region B of the specimens were measured and illustrated in Table 2-4. The MZ depth in Region A was obtained by averaging the depths in five equidistant positions. The calculation method presented reasonable accuracy for estimating the MZ depth, according to Table 2-4.

Table 2-3 Number of repetition irradiation n in different laser treatment conditions.

	LA	LB	LC	LD1	LD2	LD3
Region A	2	2	2	2	2	4
Region B	8	8	7	11	22	40

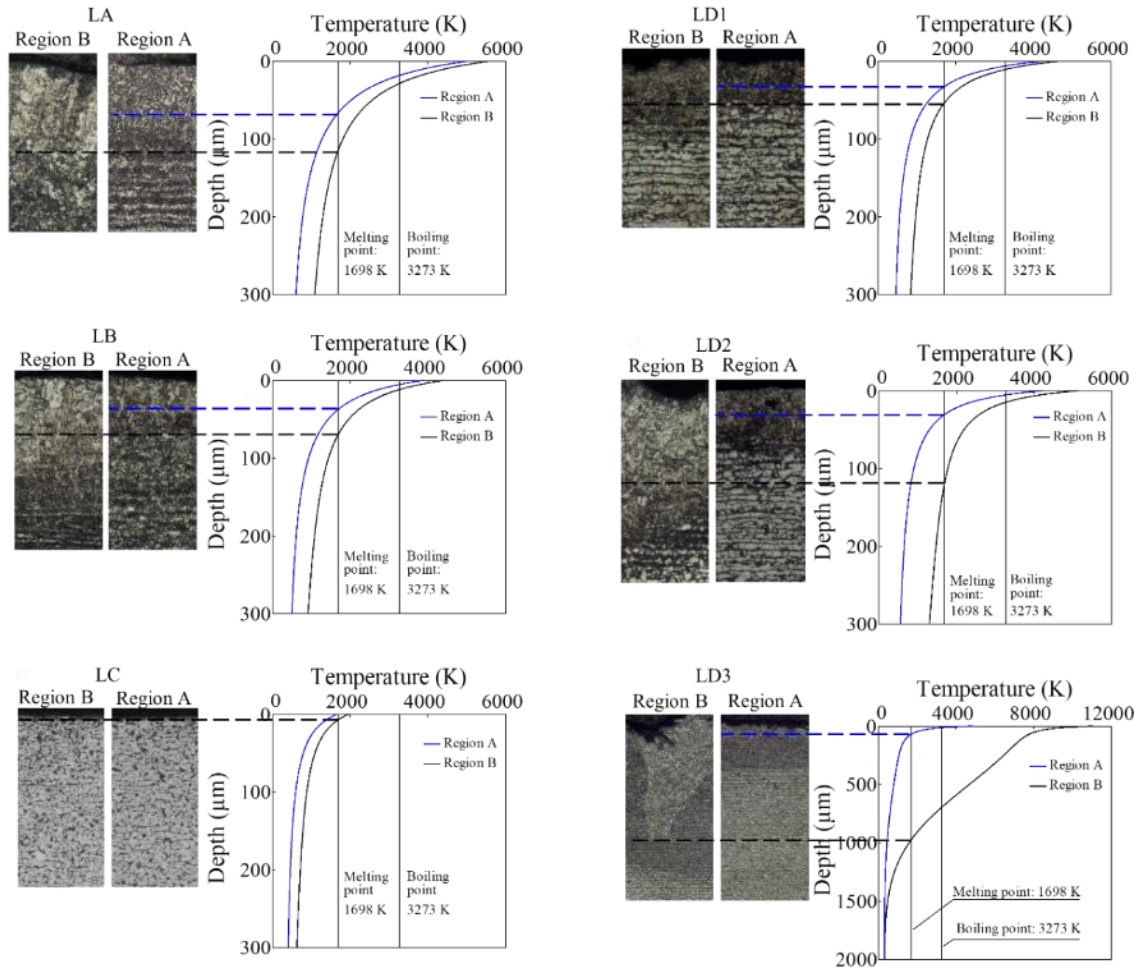


Figure 2-12 Peak temperature distribution on the cross-section of laser-treated specimens.

Table 2-4 Comparison of MZ depth obtained from OM microstructure and calculation method.

Laser condition		LA	LB	LC	LD1	LD2	LD3
MZ depth in Region A (μm)	Experiment	88.0	49.5	0	33.1	42.2	92.9
	Calculation	67.0	38.0	0	32.0	34.0	73.0
	Cal./Exp.	0.761	0.767	-	0.967	0.810	0.786
MZ depth in Region B (μm)	Experiment	137	110	0	58.5	155	976
	Calculation	115	74.0	7	54.0	112	974
	Cal./Exp.	0.840	0.673	-	0.924	0.723	0.998

Concerning the surface morphologies of laser-treated specimens, laser overlapping effects have the potential to cause surface defects. When the repetition irradiation reaches a higher state, extremely deep MZ formation is likely to take place. This was the case of the MZ in Region B of the LD3 specimen. Inhomogeneity and micro-cracks in the MZ could damage the mechanical properties of laser-cleaned structures. Therefore, the approximate calculation method could be helpful in optimizing the processing parameters of laser cleaning, to acquire a thinner and uniform MZ on the cleaned surface while reducing the risk of generation of surface defects.

2.5 Summary

A newly developed rotating CW laser treatment was considered as a surface cleaning technique for usage in construction structures. To investigate the thermal effects of the laser beam on base material, an approximate calculation method for peak temperature distribution considering laser-beam overlap is proposed. The overlapping effects of laser irradiation were considered by introducing the number of repetition irradiation into the calculation method. The surface morphologies and microstructures in cross-section of laser-treated specimens were evaluated and used for comparison with the calculation method. The main results in this chapter were summarized as follows:

- (1) Inspection of laser-treated specimens confirmed that the overlapping laser beam improves the thermal effects and causes surface defects. In which LC specimen only present pores instead of laser scanning tracks left on the steel surface after irradiation. The other laser parameters present fewer overlap effects region and obvious overlap effects region, which is in the center portion and top/bottom portion of laser ring. In the top/bottom portion, laser overlapping effects will induce bulge formation, and micro cracks are found inside the bulges in higher laser output power cases. From the surface and cross-section observation, the overlapping effects are supposed to affect the mechanical properties due to the presence of bulges, micro cracks and heat-affected zone.
- (2) The modified calculation method properly describes the peak temperature distribution under rotating CW laser irradiation. Depths of calculated MZs are in good agreement with observations of laser-treated specimens. The overlapping effects, namely the repetition irradiation can be well considered in the calculation equations. This calculation method could be useful to optimize the processing parameters, control the base material melting, and avoid surface defects during laser cleaning.

CHAPTER 3 SURFACE PROPERTIES AND MICROSTRUCTURES OF LASER-TREATED CARBON STEEL

3.1 Introduction

The laser ablation induced surface breakdown is illustrated as a schematic in Figure 3-1. When the CW laser beam hits the steel surface, the material absorbs laser energy, and the thermal motion of some particles is accelerated. Once the sublimation temperature of steel material is reached, these particles evaporate and become vaporized particles, resulting in ablated craters [58]. Owing to the high-power density and long irradiation period of the CW laser, a thin layer of steel material melted and formed the re-melted zone (MZ) after cooling. Below the MZ, the laser beam still impacts the substrate and modifies a certain depth of microstructure, which then forms the heat-affected zone (HAZ). The surface morphologies of steel plates are changed because of laser ablation effects, the surface patterns created under moving laser beam may be different according to different parameter combinations. Even when the surface temperature induced by laser beam was lower than the boiling point of steel material, once the melting point is reached, the original surface characteristics are still affected by the melting effects. Thus examining the surface properties are essential for laser heat effects evaluation. The main surface properties after laser irradiation including: surface morphologies and surface oxidation. There are concerns about the surface oxidation induced by laser irradiation, due to the presence of oxide layer could damage the surface intact, also the electrochemical properties and coating qualities [60]. On the other hand, microstructures below the surface will also modified by the laser ablation effects. In the MZ layer, completely different microstructures might reform after solidification [61]. As for HAZ layer, the effects of laser ablation including thermal and non-thermal contents (i.e. shock wave generated by laser ablation), the size and compositions of microstructures may also be changed in this area. Evaluate the microstructures also important for the mechanical and electrochemical analysis, because the chemical and physical properties of steel

material are dominated by the shape and compositions of microstructures.

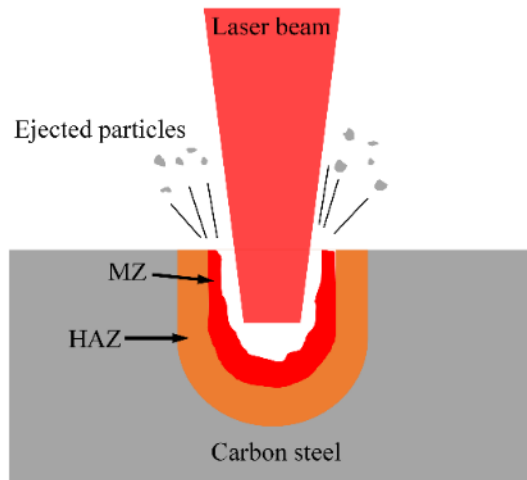


Figure 3-1 Schematic diagram of laser ablation effects.

In consideration of field application, most of the laser processing parameters were predetermined and unable to change. Consequently, human operation during the laser treatment only holding the laser equipment and controlling the laser ring moving speed v_R as shown in Figure 2-1. As a result, the gap between adjacent laser ring could create untreated area due to the laser ablation only affect certain range of area. Assuming a laser operator handling the equipment to clean a corroded steel surface rapidly, as shown in Figure 3-2, the excessive laser ring moving speed turned out to be an improper parameter that leave untreated areas. Which reduce the efficiency of laser surface treatment, and leaving residual salts or contaminators on the laser-treated surface. Thus an appropriate laser ring moving speed, or in other words, an upper limit for the laser ring moving speed is required.

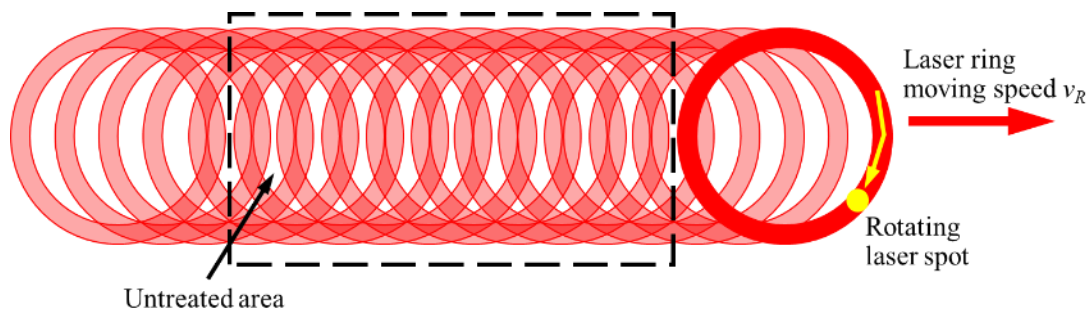


Figure 3-2 Untreated area under higher laser ring moving speed.

Also, the high power CW laser aims for severely corroded steel members. Deep corrosion pits exist on the steel surface are tough issues for the surface preparation. An example of corrosion pits on severely corroded steel member is presented in Figure 3-3. The steel member is removed from rock shed which exposed at coastal region of Kagoshima (Lat. $31^{\circ}53'51''\text{N}$, Long. $130^{\circ}13'20''\text{E}$) for 41 years. Corrosion pits were observed on the steel surface, causing irregularity appearance, and diamond disc grinder was managed to remove top rust layers only in consideration of avoiding damage on base metal. Therefore, corrosion products inside large pits still remained after the cleaning treatment. The corrosion pits containing salts and rust which is difficult to remove completely, therefore damage the durability of repainted coating. Besides, the irregular surface profile will also induce laser defocus, which might decrease the laser ablation effects.



Figure 3-3. Surface conditions of severely corroded steel member before and after removing the rust layer.

Laser defocus is a common problem during laser treatment [62], the deep corrosion pit which exists in severely corroded steel surface may induce power attenuation, and affect laser treatment efficiency. There are two kinds of laser defocus, one induced inside the bottom of corrosion pit, known as positive defocus; the other occurs on the top of corrosion products, known as negative defocus. Studies from other researchers had proved that negative defocus only have a little effects on the power distribution [62][63],

desirable laser heat effects can be still obtained. Besides, the outer rust layer is less dense and easier to remove. However, positive defocus decrease the energy distribution of laser beam sharply, and that is the main type of laser defocus induced on corroded steel surface.

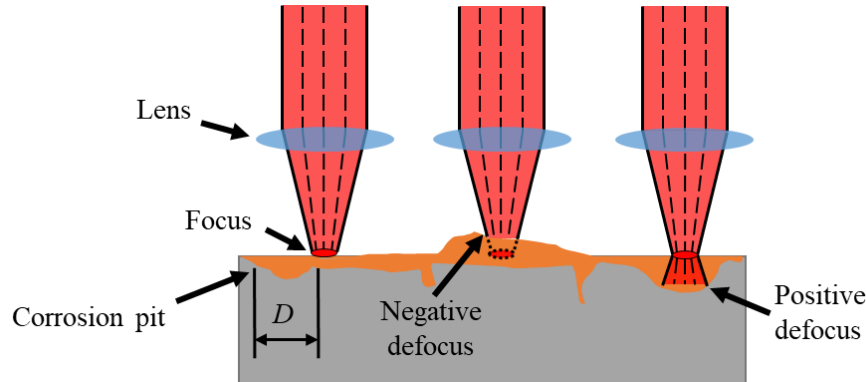


Figure 3-4. Laser defocus on the severely corroded steel surface.

In the surface properties and microstructure observations, all the laser conditions evaluated in CHAPTER 2 were adopted for laser surface treatments. According to the parameters of each laser condition, the LA and LB refers to different interaction time, while LB and LC imply varying laser power densities. The LD1, LD2 and LD3 conditions are the same laser parameters with different moving speed of laser ring, which means different laser overlapping effects occurred under these conditions. Thus the evaluation of surface characteristics and microstructures of laser-treated steel plates were based on the laser parameters analysis of interaction time, power density and overlapping effects. The surface morphology, iron oxide, microstructures and hardness of laser-treated steel plates were evaluated.

Concerning the field application of laser surface treatment, the laser treatment coverage under different laser ring moving speed is observed under LA and LD conditions. On the other hand, LA condition was chosen for the surface irradiation of steel plate with artificial corrosion pits, to verify the effects of laser positive defocus on the laser ablation effects.

3.2 Experimental

Carbon steel plate according to JIS G3106 SM490A with dimensions of 150×70×9 mm is prepared for the laser irradiation. The mill scale were removed by abrasive blasting before laser irradiation to achieve identical surface condition before laser irradiation. All

laser conditions listed in Table 2-1 were used for specimen preparation. To identify the surface crystalline phases and elemental distribution, the laser-treated specimens were prepared as bulk samples for X-ray diffraction (XRD, model: SmartLab, Rigaku) and scanning electron microscope-energy dispersive X-ray spectrometry (SEM-EDX, model: SU3500, Hitachi) evaluation. Due to the difficulty of spotting observation position using the SEM-EDX equipment, only Region A as described in CHAPTER 2 was observed. The measurement area in XRD study including Region A and Region B. The XRD measurements were performed with Cu-K α radiations ($\lambda=1.54 \text{ \AA}$) X-ray source under generator settings of 40 kV and 30 mA, and the data was collected over a range of 20° to 90°. The cross-sections of laser-treated specimens were prepared, polished, and etched with 2 % nital, and the microstructure of the specimens was observed under optical microscopy (OM, model: VHX-1000, Keyence). The surface roughness of laser-treated specimens were measured using laser scanning microscope (model: OLS4500, Olympus), the surface profile in Region A and Region B were observed after laser irradiation, every profile measurements were conducted in sampling length of 10mm for 11 times. Vickers hardness (HV) of the cross-sections in Region A and Region B along thickness direction were tested under 100 gf test force and 15 s holding period.

In order to simulate the insufficient laser surface treatment induced by hand-hold operation, various laser beam overlapping rate result from different laser ring moving speed were adopted. The overlapping rate were ranged from 50% to -200%, namely, the distance between laser spot centers of repetitive irradiation changed from the beam radius to twice the beam diameter. The laser absorption of specimen surface would changed due to various factors [53], such as the surface roughness, chemical composition and environment temperature, etc. In order to acquire basic laser ring moving parameters for the field application, the smooth surface with lowest absorptivity is designed as the surface condition for laser beam overlapping rate observation. In this case, milling process was taken to remove the mill scale and provide smooth surface before laser irradiation. LA and LD conditions were adoped as the laser conditions, where the laser paths only scan the specimens surface once, thus no laser ring overlap in these specimens. Between parallel laser ring paths, interval time was prepared for the steel plates to return to room temperature before next irradiation.

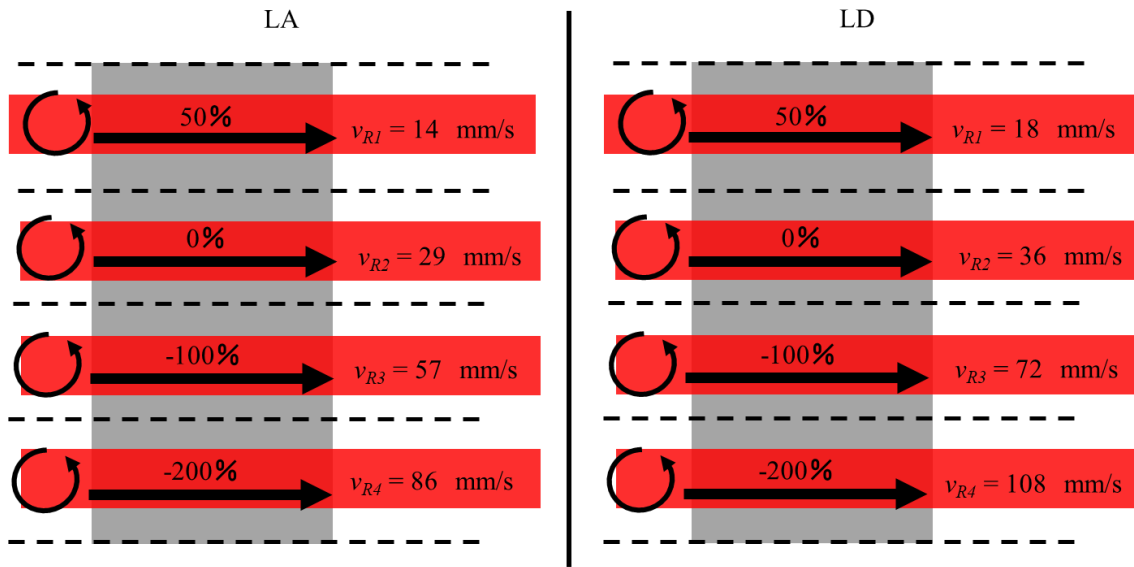


Figure 3-5 Specimens under different laser beam overlapping rate.

On the surface of severely corroded steel plate, various shapes of corrosion pits are included. The main control variables which affect laser surface treatment most are pitting depth and width. The depth of corrosion pit induces laser defocus at the bottom, which may weaken the laser output power density. On the other hand, a narrow corrosion pit only allows short irradiation period inside the pinhole, thus limiting heat transfer from laser beam to the bottom of corrosion pit. In consideration of irregular corrosion morphology on the steel plate, the corrosion depth and pinhole width are regarded as separate parameters for evaluation of laser treatment effects. Carbon steel plate of SM490A is prepared for artificial corrosion pit processing. A flat drill was used during drilling processing, in order to acquire smooth bottom for surface analysis. To compare the laser effects at upper surface and inside the artificial pit, milling process was adopted before drilling to remove mill scale and provide similar surface conditions for both positions. For specimens with different corrosion depths, the same pitting diameter of 4 mm is chosen, and the pitting depths are range from 2 mm to 8 mm. The same pitting depth is manufactured in a line, and different depth of artificial pits was separated to avoid mutual interference when irradiating adjacent corrosion pits. During surface treatment, laser ring scanning across the line of corrosion pits at given speed, then interval time was prepared between each irradiation, allowing steel plate cooling down to room temperature. The same laser treatment method was applied to the specimen with different pitting width,

in which the pitting depth maintain at 4 mm. Only LA condition is used in the laser irradiation. The OM photos of specimens with artificial corrosion pits were taken to verify the laser ablation effects, and SEM-EDX surface inspection on the element of Fe and O also conducted to further verify the thermal effects of laser irradiation inside the various size of artificial corrosion pits. Figure 3-6 shows the specimens with artificial corrosion pits and laser irradiation method.

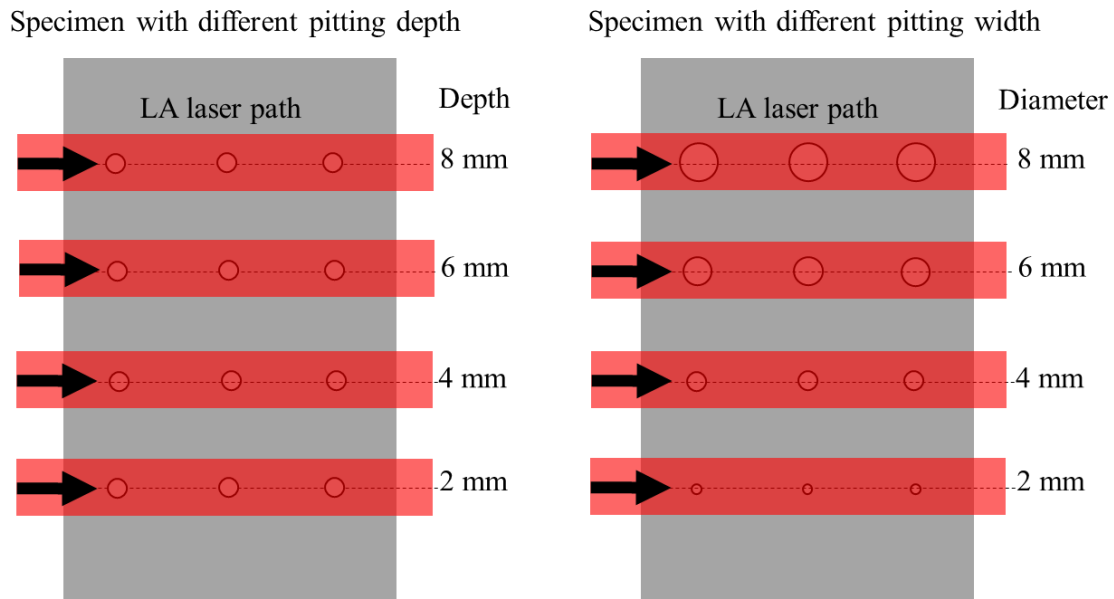


Figure 3-6 Specimens with artificial corrosion pits and laser irradiation path.

3.3 Surface morphology of laser-treated carbon steel plates

Figure 3-7 shows the high magnification OM surface morphologies of the specimens. Two regions on the specimen surface were observed according to Figure 2-8, in which Region A implies the area encounter less laser overlapping effects and the Region B is area suffered more laser overlapping effects as described in the CHAPTER 2. In Region A, the Laser scanning tracks were observed in LA, LB and LD1 conditions, yet LC presented no distinct scanning tracks, except for some small pores. The reason for pore formation instead of ablation craters in LC conditions is the escape of gases during resolidification [64]. Under a lower power density and interaction time, the melted materials resolidified before the liquid can fill the pores caused by escaping gases [65]. LA, LB and LD1 conditions possessed higher power density and interaction time than LC conditions. Thus, more energy transformation is acquired [66]. The peak temperature on

the steel surface as discussed in CHAPTER 2 also verified the thermal effects under LC conditions only induced melting of steel material, and the other laser conditions provided peak temperature exceed boiling point of steel material. Consequently, deeper and wider ablation craters are formed in the LA, LB and LD1 conditions, and appear as scanning tracks on the surface. Among the laser tracks appeared on the steel surface, LA condition tend to have wider tracks than the LB condition, notice that LA and LB conditions used the same laser beam generator but different rotating speed and laser ring moving speed, the faster rotating speed of LB condition presented less time for laser beam to interact with steel surface, thus a narrower tracks were presented in LB condition. The gap between laser tracks also indicated laser ablation effects only effective in a given range of the Gaussian power distribution, rather than the whole area inside laser beam. On the other hand, when the moving speed of laser ring drop down to a certain value, the surface morphologies of steel plate after laser irradiation presented irregular patterns as shown in LD2 and LD3 specimens. Laser scanning tracks were vanished and replaced by wave-like surface features. This is assumed that slower moving speed of laser ring causing more overlapping effects, and reduce the distance between the adjacent laser tracks. The resolidified steel materials could be remelted by the adjacent laser scanning tracks, and irregular ablation craters were formed on the steel surface.

In Region B, all of the laser conditions revealed top/bottom position in rotating laser irradiation but LC condition. Only pores can be observed on the LC specimen surface as presented in the Region A, implying the laser overlapping effects had few impact in this portion. The peak temperature in LC condition as shown in Figure 2-12 confirmed only melting can take place in this region rather than laser ablation effects. In contrast with the LC condition, LA, LB and LD1 conditions showing the boundary of top/bottom position and middle position in two laser ring moving paths. The middle position of laser ring revealed surface features with clear laser scanning tracks as shown in Region A, on the contrary, top/bottom position presented a surface morphologies without laser scanning tracks, but rather irregular patterns. According to the overlapping effects as described in CHAPTER 2, more repetition irradiation was arose in the top/bottom position, repetitive melting and solidification will occurred in this region, leading to irregular surface patterns. When the laser ring moving speed slow enough, extremely severe overlapping effects

were presented in the top/bottom position as shown in the LD2 and LD3 specimens. Bulge structures were observed around the boundary line, and surface defects were included in it, the main reasons for bulge structures were discussed in CHAPTER 2 and Figure 2-10.

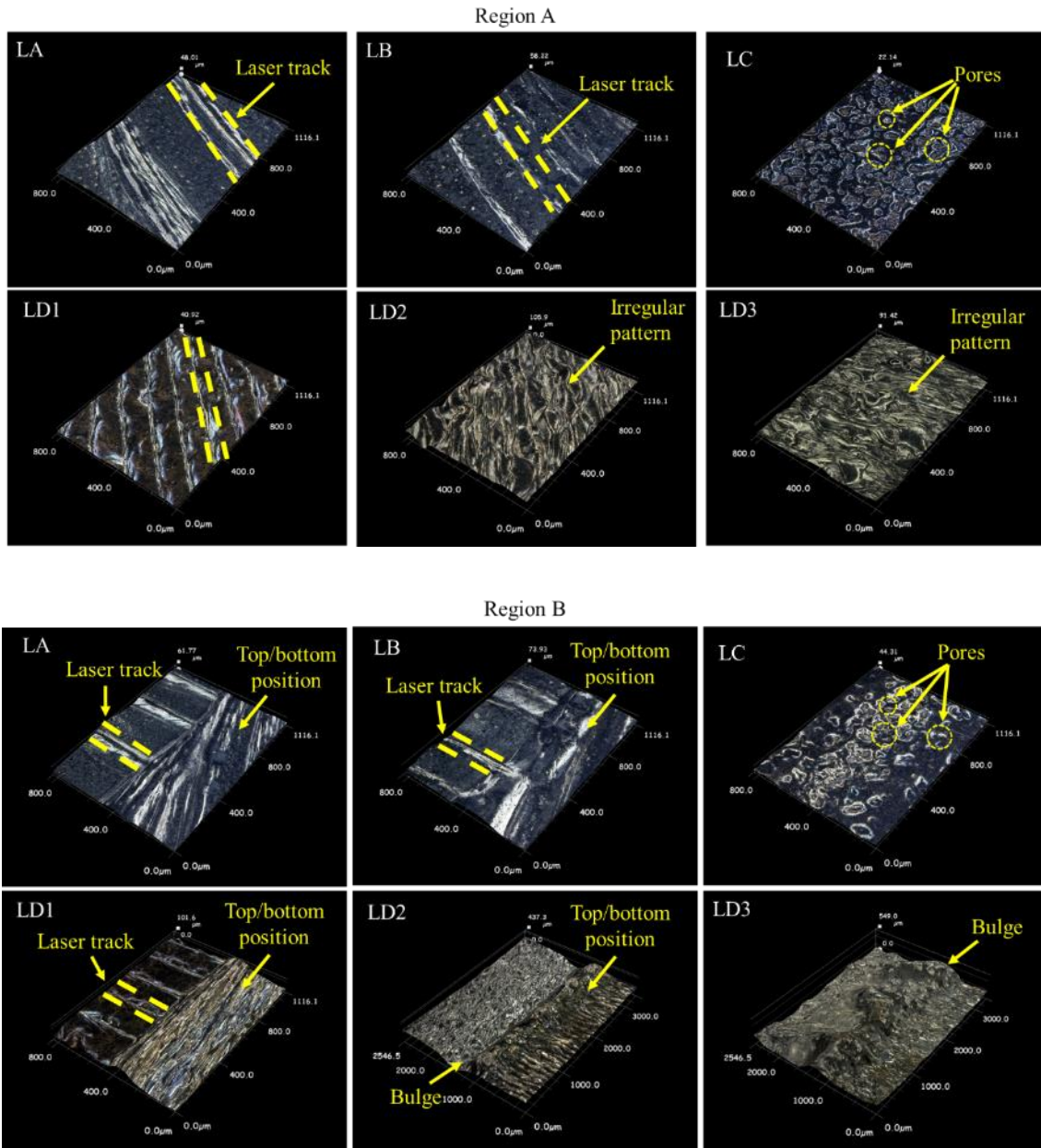


Figure 3-7 OM surface morphologies of specimens.

In general, from LA and LB specimens, less laser interaction time contributed to a similar surface morphologies, only narrower laser scanning tracks were observed. Laser power density is a more important parameter responsible for the laser-treated surface

features, according to LB and LC conditions. Where lower the laser power density to the level of LC, the laser ablation effects decreased and showing no obvious laser scanning tracks. When the moving speed of laser ring decreased (i.e. more severe laser overlapping effects), surface morphologies of laser-treated steel plate changed significantly, irregular patterns were presented on the steel surface, result in obvious cratered surface. The bulge structures were formed on the higher laser overlapping effects area, Region B, due to severe laser heat effects induced by repetitive melting and solidification.

The cross-section profile of laser-treated steel specimens were illustrated in Figure 3-8. The roughness distribution in Region A were similar from LA to LD2 specimen, with increasing laser overlapping effects, the cross-section of LD3 specimens in Region A presented obvious improving roughness. Associate with the irregular surface features observed in Figure 3-7, more obvious peaks and valleys structures were dominate this area and improved the surface roughness. Compares to the other profile observed in Region A, broader peaks were presented with less micro roughness characteristics. The less detail profile may be attributed to the more repetition irradiation, repetitive melting and solidification result in higher peaks and valleys, and eliminate the laser ablated craters and cracks. As for the cross-section profile in Region B, LC and LD1 conditions presented similar trends to the Region A, while the other laser conditions revealed less detail profile as described before. It is worth noting that peaks and valleys in LD2 and LD3 specimens were significantly improved, 2 times and 8 times of the range were observed respectively.

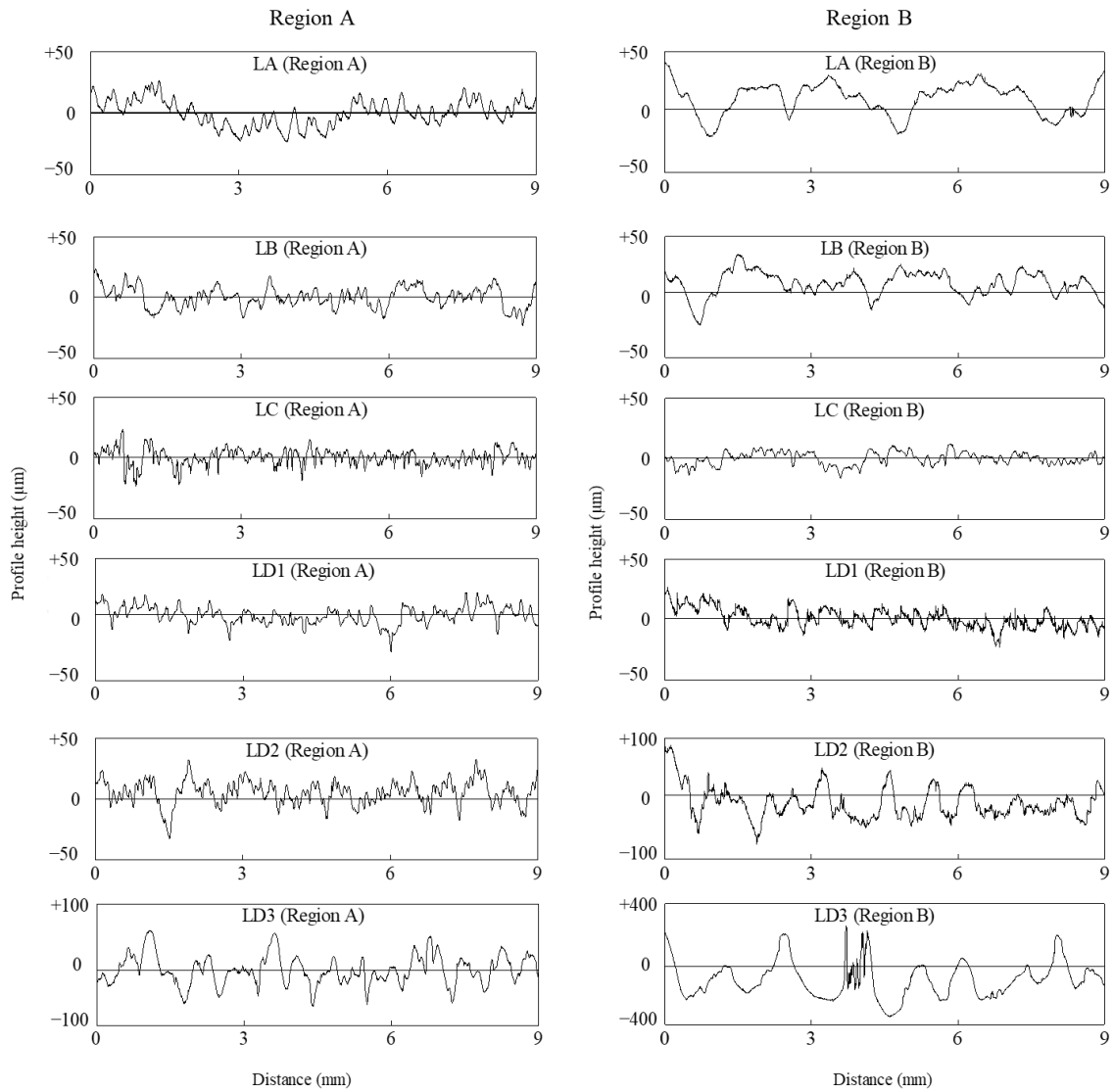


Figure 3-8 Cross-section profile of laser-treated specimens.

The most common expression for average peak height is R_a which is the arithmetical mean deviation of the assessed profile, the calculation:

$$R_a = \frac{1}{l} \int_0^l |Z(x)| dx \quad (3-1)$$

where l is the sampling length, $Z(x)$ the ordinate value within the sampling length.

The measured roughness R_a of all laser conditions were presented in Figure 3-9, the

results showed similar trends to the cross-section profile observation. In which, Region B possessed higher roughness than Region A. For laser conditions LA, LB and LC, R_a less than $10\ \mu\text{m}$ regardless of the measurement region. When the laser overlapping effects significantly increased, as shown in LD1 to LD3, the roughness rose dramatically. R_a in Region B of LD3 specimens even reached $80\ \mu\text{m}$, which is 8 times larger than the other laser conditions.

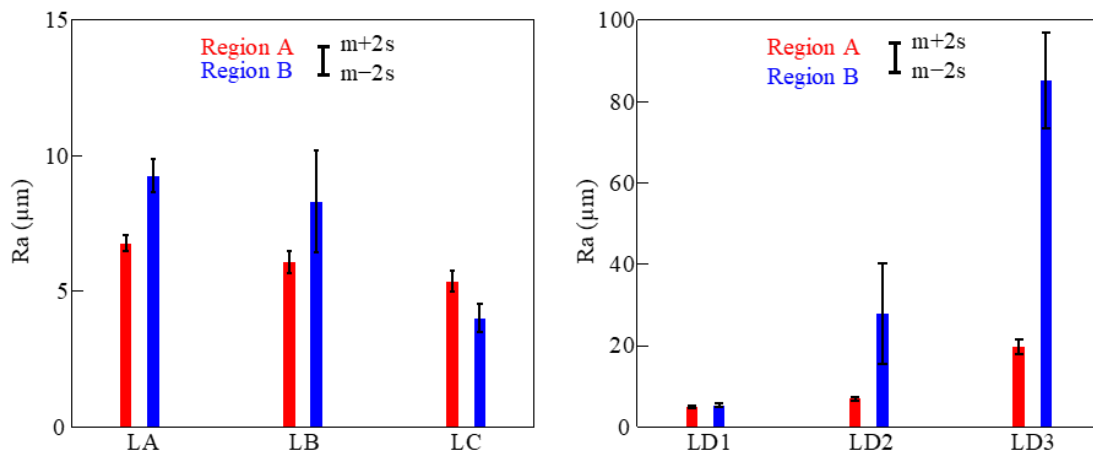


Figure 3-9 Surface roughness of laser-treated specimens.

The rough surface features generally considered as a beneficial factor for improving the adhesion of organic coating. Long term corrosion protection of the coating rely on its integrity, in this case, prevailing hypothesis is the corrosion protection improved with the adhesion property. In construction field, high adhesion strength is the essential requirement for a coating system to remain effective protection. In fact, the relationship between adhesion and durability of coating system still under study, particularly when it comes to surface roughness. By contrast, the thickness of coating is straightforward factor that affect durability of coating layer. Long term corrosion protection of the organic coatings requires the thickness in millimeter scale. In the area of infrastructure, the limitation for surface roughness is to control the thickness of coating layer. Thicker coatings are supposed to have better corrosion protection, and the coating are supported better by the metal substrate when the rough surface protrudes more into the coating. But there are limits for the surface roughness, a very rough surface might possessed defects on it, and the coating layer is difficult to fill the deepest valleys thus leave cavity between the coating and substrate surface. On the other hand, the thickness of coating at highest

peaks might be decreased and thus damage the durability of coating system [67]. Hence, the bulges formed under higher laser overlapping effects not only changes the surface morphologies, but also affect the durability of coating layer to a certain state. Besides, micro cracks could affect the mechanical properties of steel material as well.

3.4 Evaluation of oxide layer on steel surface after laser treatment

3.4.1 SEM-EDX surface elements analysis

From the SEM-EDX results shown in Figure 3-10, oxygen is observed on the steel surface after laser treatment. Oxygen mainly exists inside the small pores of the LC, and the center of the laser scanning tracks of LA and LB. Semi-quantitative analysis of SEM-EDX revealed that the oxygen content on the laser-treated surface was 20.0, 14.3, and 9.72 wt% for LA, LB, and LC specimens, respectively. The variations in the oxygen content of LA and LB conditions are caused by the varying interaction times. Longer interaction time of LA results in more laser energy absorbed by the steel surface to initiate oxidation. The relatively smaller power density and interaction time of LC limited the laser heating effects, presenting the lower surface oxygen content.

Compares to the other specimens, LD1 condition possessed lowest oxygen content on the surface. Then, the oxygen content increased with increasing laser overlapping effects. It is showed that LD1, LD2 and LD3 have oxygen content of 4.87, 11.7 and 18.7 wt% respectively. This would be attributed to the fast scanning speed of LD conditions, the interaction time of LD among the other laser conditions is the shortest of 31.6 μs , which is half the LB and LC conditions and one third of LA condition. The principle of laser ablation is based on melting and vaporization. When the laser beam hits steel surface, the material absorb laser energy and start to melt or vaporize, depending on the temperature. Larger power density causes higher temperature on the heated material, and shorter interaction time limits the heat conduction during laser ablation, therefore the ablation is enhanced, resulting in larger volumes of removed material from steel surface. In this case, the power of LD1 is large enough to produce a relatively ablation dominated processing mechanism. The heated materials in higher temperature were ablated, and took away most of the energy by themselves. Therefore, the remaining energy in the base metal could be relatively small, resulting in clear laser paths and less oxygen on the surface. With increasing laser overlapping effects, repetitive melting and solidification replace the

ablated surface features with resolidification features as shown in LD2 and LD3 of Figure 3-10, thus a higher oxygen content is presented in the higher overlapping effects laser conditions.

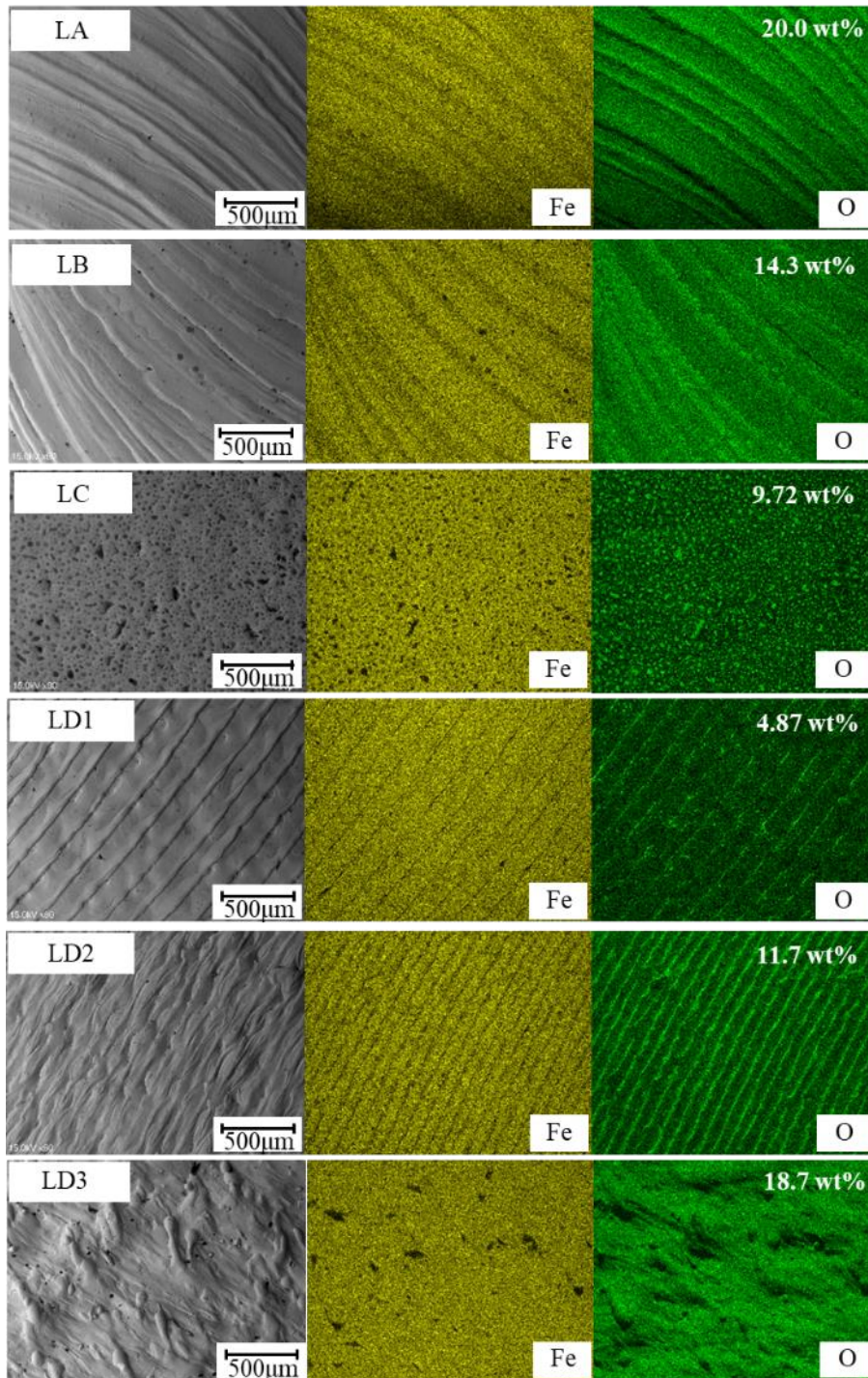


Figure 3-10 SEM-EDX analysis on surface of specimens.

Concerning the laser treatment parameters, shorter interaction time restrict the surface

oxidation reaction as shown in LA and LB specimens, as well as decreasing the laser power density according to LB and LC specimens. On the other hand, increasing laser overlapping effects contribute to the oxidation reaction during laser treatment.

3.4.2 Iron oxide evaluation using XRD diffraction patterns

To further clarify the composition of the oxide film, XRD patterns of the specimens were obtained and are illustrated in Figure 3-11. From the peaks observed, XRD results corresponding to the SEM-EDX analysis. The surface contain more oxygen presented more iron oxide patterns. Different iron oxide compositions were identified in all laser-treated specimens. Patterns of wustite (FeO) were observed in all of the laser-treated specimens, while LA and LB specimens presented patterns of magnetite (Fe₃O₄) or maghemite (γ-Fe₂O₃), which are indistinguishable by XRD [68]. While LC specimen surface only possessed wustite diffraction patterns. On the other hand, LD1 specimen revealed even lower wustite peaks than LC specimen, and the patterns of magnetite or maghemite appeared and increased in LD2 and LD3 specimens.

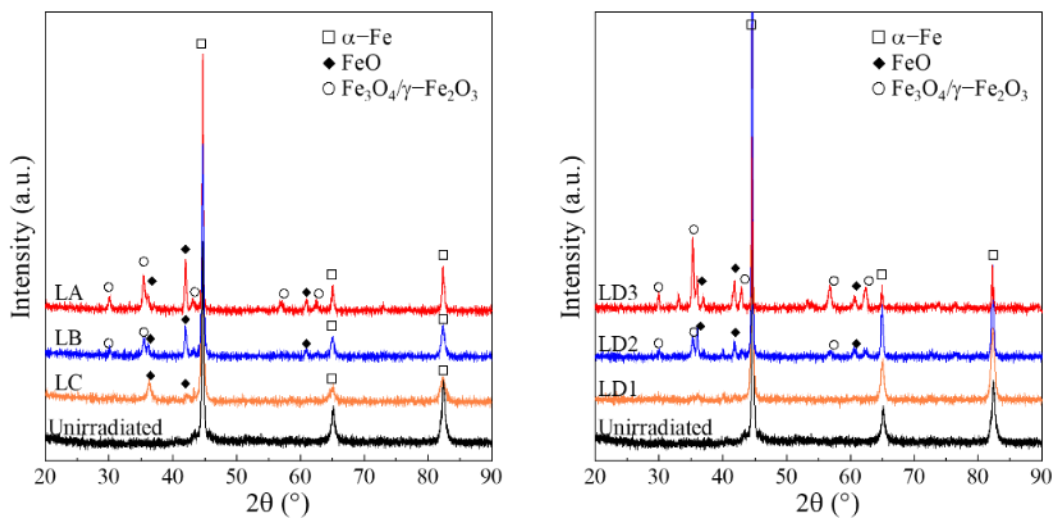


Figure 3-11 XRD diffraction patterns of laser-treated specimens.

Semi-quantitative analysis based on relative intensity ratio (RIR) [69] was performed to verify the oxide component on laser-treated specimens, Figure 3-12 presented the weight ratio of α-Fe, FeO and γ-Fe₂O₃/Fe₃O₄. It can be seen that a higher proportion of iron oxide was achieved in LA and LB conditions, where LA possessed more γ-Fe₂O₃/Fe₃O₄ than LB. LC showed the lowest iron oxide proportion, containing 9 wt% FeO. In the case of LA and LB conditions, the same power density and longer interaction

time of LA contributed to a slightly higher oxide proportion. On the other hand, the LC condition has a similar interaction time with LB but a lower power density, leading to an obvious decrease in oxygen content and oxide components. Therefore, increasing the power density and interaction time will amplify the laser ablation effects on surface morphology. Meanwhile, improved heat transfer from the laser beam to the specimen surface promoted the formation of iron oxide at a higher oxidation state (i.e., γ - $\text{Fe}_2\text{O}_3/\text{Fe}_3\text{O}_4$), in which the surface oxide formation is significantly affected by the laser power density. When the laser overlapping effects increased, as shown in LD1, LD2 and LD3 specimens, the amount and components of iron oxide increased. In which higher state oxide of γ - $\text{Fe}_2\text{O}_3/\text{Fe}_3\text{O}_4$ appeared at LD2 and LD3 conditions. Among all the laser-treated specimens, LC possessed the least iron oxide, while LD3 presented higher iron oxide content on the surface.

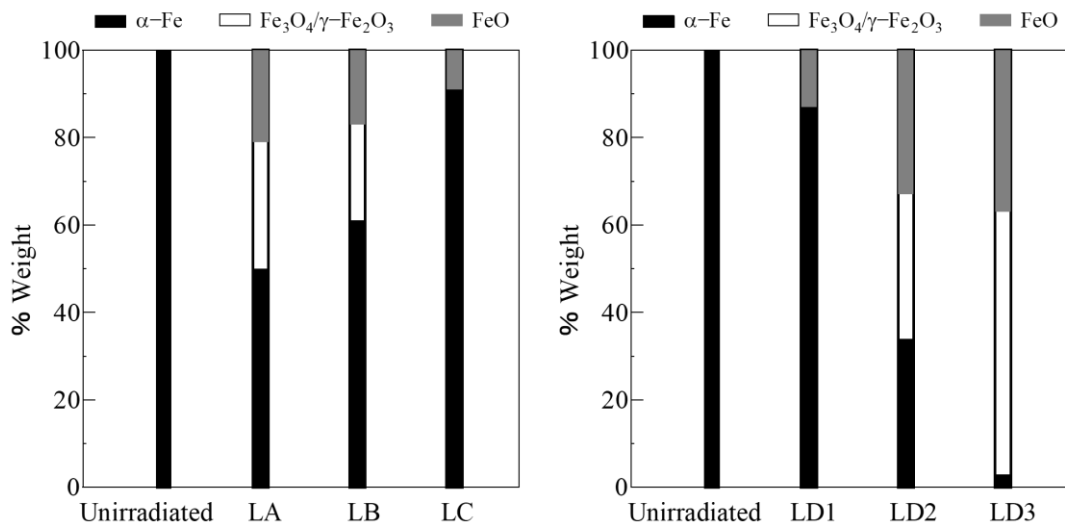


Figure 3-12 XRD semi-quantitative analysis of iron oxide formed on specimen surface.

It can be seen that longer laser interaction time contribute to more oxide formation, as LA and LB specimen shows. While decreasing the laser power density restrict oxidation reaction on the steel surface, less oxide content were revealed, as shown in LB and LC specimens. The laser overlapping effects dramatically promote oxidation during laser irradiation according to LD1, LD2 and LD3 specimens. Under the same laser equipment parameters, the iron oxide content on the steel surface would rise from 13 % to 97 % due to improving laser overlapping effects.

3.5 Evaluation of microstructure and hardness distribution on cross-section of laser-treated specimens

The OM microstructures in the MZ and HAZ under different laser conditions are shown in Figure 3-13. The microstructure distribution on Region A and Region B were similar to each other, only revealed depths difference, thus only the cross-sections in Region A were discussed in this section. From the microstructure of the base metal, the constituents of SM490A grade steel are characterized as ferrite and perlite. It can be seen that besides LC specimen, the other laser conditions revealed certain depth impacted by the laser treatment. The main reason for microstructure changes are attributed to the laser ablation effects, as for LC condition, only melting can be induced by the laser beam, thus no laser ablation effects result in less change in the microstructures. On the other hand, other laser conditions presented similar microstructure distribution, only different depths were observed. As for the microstructure distribution in the MZ of laser-treated specimens, refined microstructures were observed owing to the rapid heating and cooling rates of laser treatment. Although the phases in the MZ are difficult to identify through OM microstructures, martensite and bainite are very likely to exist because of the high temperature gradient and the non-equilibrium rapid solidification phenomena [70]. The melt pool of the laser-irradiated area undergoes different cooling rates in the depth direction, and the microstructure may transform into upper bainite, lower bainite, or martensite [71]. Similar microstructure distribution after laser treatment can also be found in the works of Bendoumi et al.[43] and Zhou et al.[72]. Beneath the MZ layer, refined ferrite and pearlite were observed, representing the HAZ in laser-treated specimens.

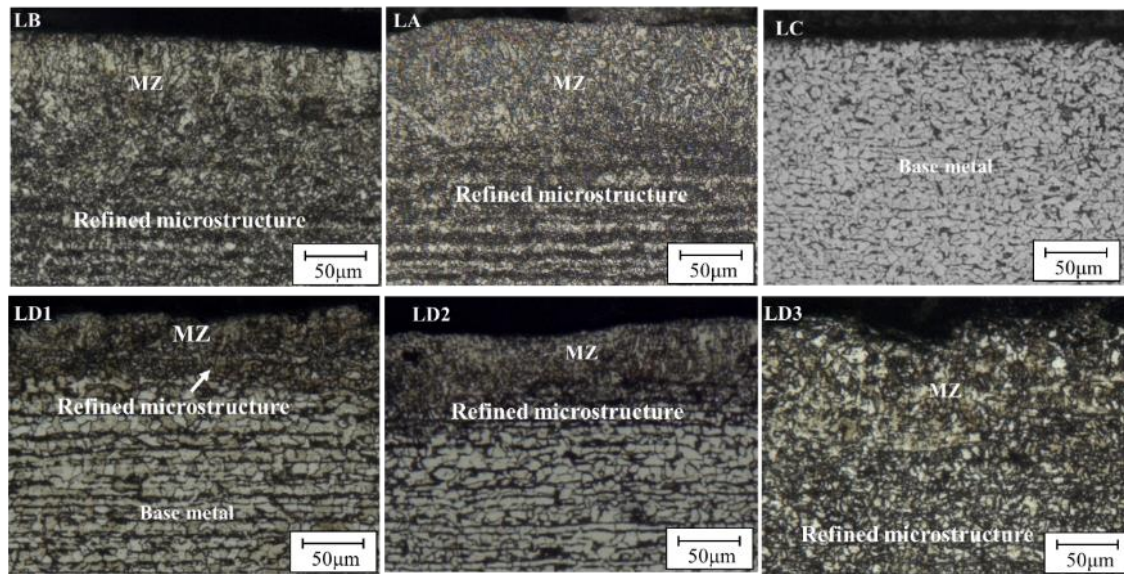


Figure 3-13 OM microstructure on cross-section of laser-treated specimens.

Figure 3-14 shows the HV on the cross-section of laser-treated specimens. The cross-section of MZ&HAZ were presented on the side of HV results as comparison. The center of Region B and nearby Region A were chosen for the Vickers hardness test. With longer laser interaction time, the depth of MZ&HAZ increased, as shown in LA and LB specimens. In which LA shows approximately 500 μm MZ&HAZ deepness in Region B, and 300 μm deepness in Region A, where the depths in LB specimen were 250 and 200 μm respectively. No visible MZ&HAZ can be observed in LC specimen due to the lowest laser thermal effects. With increasing laser overlapping effects, as shown in LD1, LD2 and LD3 specimens, the depth of MZ&HAZ were significantly increased. In which the MZ&HAZ deepness increased from 50 to 500 μm in Region A, and 50 to 1500 μm in Region B. The changing MZ&HAZ are supposed to affects the mechanical properties of steel material, as the essence of these layers is the microstructure changing. The hardness of metallic material were generally considered as a representative parameter for the mechanical properties, actually, the yield strength and ultimate tensile strength are proportional to hardness [73]. According to Figure 3-14, the hardness mostly improved within the MZ&HAZ layer, in the Region B, the improving hardness are more noticeable under LA, LB and LD2 conditions. Hardness improvement of approximately 50 HV were presented in these specimens. When it comes to LD3 condition, opposite hardness results were presented Region A and Region B. Higher hardness distribution was observed in

Region A of the LD3 specimen, and relative lower hardness were presented in the Region B. It was considered that the grain size in MZ of Region B grown under higher laser overlapping effects of LD3 condition, the repetitive irradiation restrict cooling speed of the laser-melted materials, as a result, the solidification of liquid materials slow down and formed larger microstructure [74], as shown in Figure 2-11. It is obvious that MZ layer in Region B of LD3 specimen is significantly deeper, reaching 1200 μm in approximately, thus the composition of MZ&HAZ in LD3 is mostly composed by MZ. Usually, larger grain size contribute to lower hardness in steel materials [75]. As a consequence, the hardness in Region B of LD3 decreased.

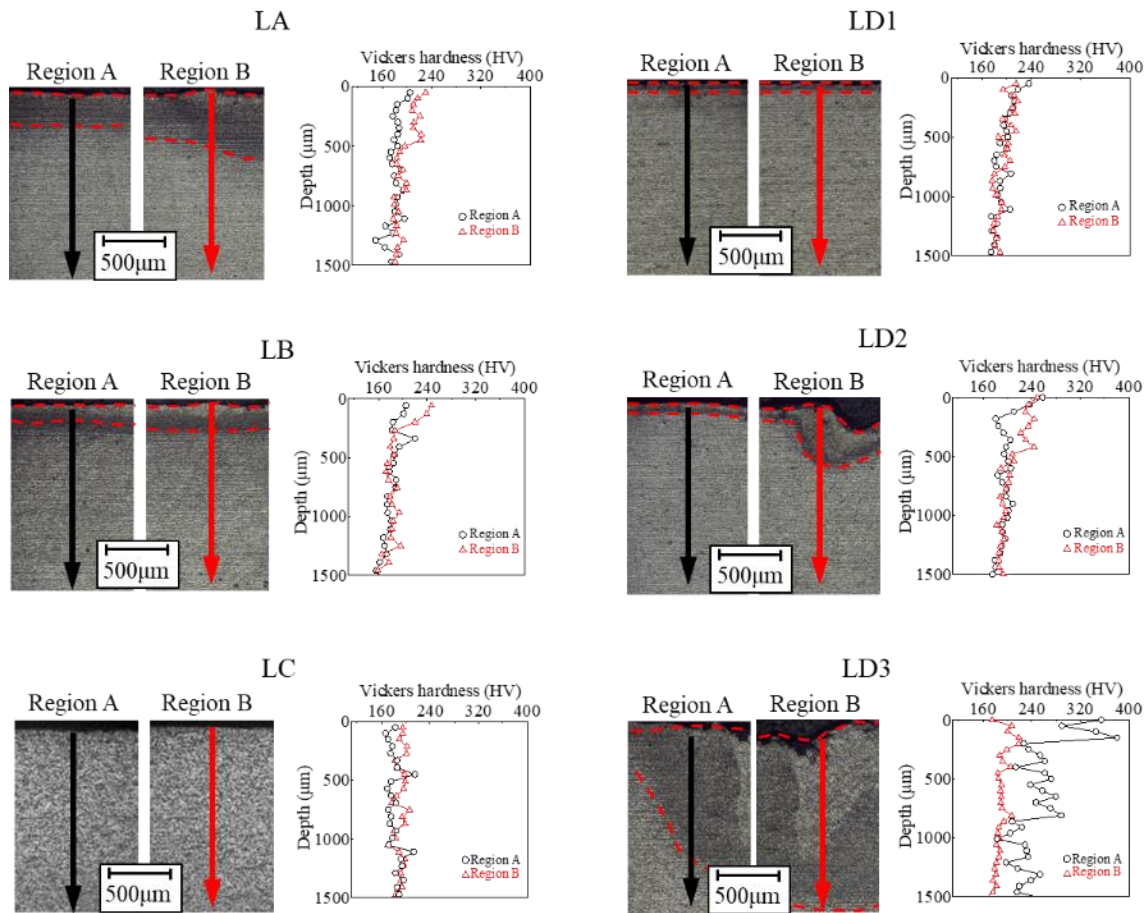


Figure 3-14 HAZ and HV on cross-section of laser-treated specimens.

3.6 Consideration of laser effectiveness in field application

3.6.1 Evaluation of appropriate laser ring moving speed for hand hold operation

The surface conditions of steel plates after laser irradiation were exhibited in Figure

3-15. The observation spots were selected at the center of the laser scanning paths, where the coverage of repetitive irradiation should be the lowest as illustrated in Figure 2-6. In this case, if the laser coverage in this position reached whole area, there will be no untreated area in the laser scanning path. On the opposite, even small untreated area was spotted in the path center still means more untreated areas were existed at the upper portion of the laser scanning path.

From the surface condition observed, the surface coverage of both laser condition reached whole area when the laser beam overlapping rate was equal or greater than 0%. With the laser ring moving speed accelerate, the untreated area were observed in both laser conditions from -100% overlapping rate, and keep growing with less laser beam overlapping rate (i.e. higher laser ring moving speed). Although the laser absorptivity of corrosion product may higher than the milled steel surface, the fundamental research are lacking to give a certain laser ablation effects for the corrosion product. To be on the safe side, the proper laser ring moving speed was selected as the resulting laser beam overlapping rate higher than 0%, to ensure comprehensive treatment. Take LA and LD conditions as examples, the laser ring moving speed were expected to lower than 29 and 36 mm/s, respectively.

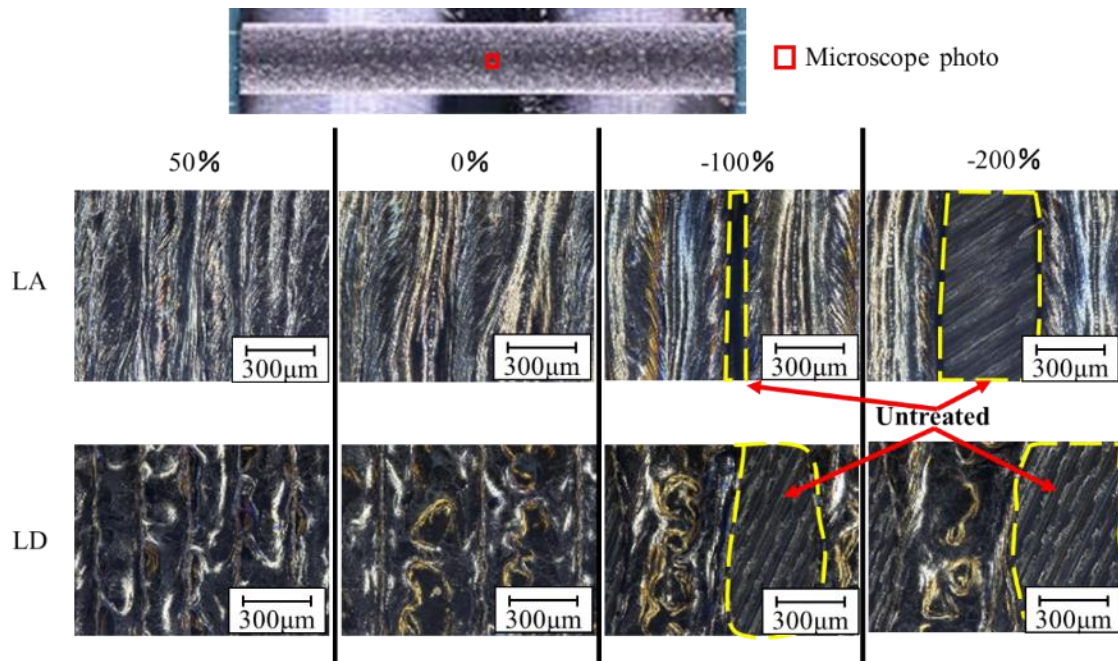


Figure 3-15 Surface condition of steel plate after laser treatment with varying laser beam overlapping rate.

3.6.2 Effectiveness of laser surface treatment for the carbon steel with severe artificial corrosion pits

Two positions as upper surface near the edge of corrosion pit, and bottom surface at the center of corrosion pit were selected to observe the surface morphology, as shown in Figure 3-16. The surface upon corrosion pit was used as comparison to identify the effects of corrosion pits on laser surface treatment.

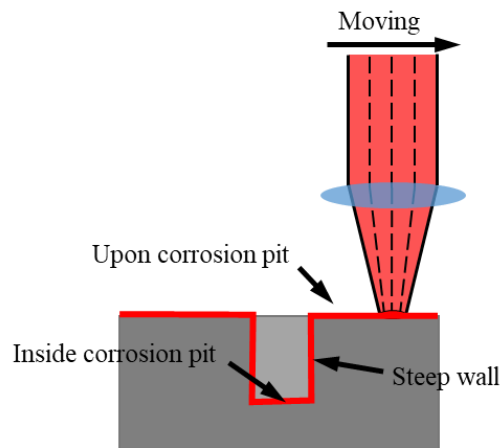


Figure 3-16 Observation positions on specimen with artificial corrosion pit.

The results of surface morphology and corresponding contour plots are shown in Figure 3-17. From the surface morphologies of specimen with different corrosion depths, the laser paths were observed in every depth of corrosion pits, demonstrating effective laser irradiation for all corrosion depth investigated in this study. The positive defocus of laser beam on the corrosion pit bottom enlarges the size of laser spot, thus laser defocus is likely to reduce power density in case of larger spot size. The laser surface treatment is mainly depending on thermal effects induced by laser beam, thus lower power density will limit the interaction between laser beam and target surface. Less effective laser ablation could be induced by the decreasing laser power density. However, on the basis of surface morphology observed inside corrosion pit up to 8 mm depth, an acceptable laser ablation effect was provided.

Basing on the surface morphologies inside corrosion pits with different pitting width as shown in Figure 3-17. Although the laser scanning paths were also presented at the bottom, a blurry image of laser path is shown inside corrosion pit with 2 mm diameter. Among the corrosion pits with different width, identical laser defocus are ensured because

of the same artificial pitting depth. On the other hand, steep wall of pinhole results in discontinuous in upper surface and the corrosion bottom, thus reduce the thermal effects during laser irradiation. In addition, high-density fumes and particles also generated and confined in the narrow pit hole during laser irradiation, then act as a shelter and reduce the thermal effects of laser beam reaching the bottom surface [76]. In fact, the laser energy will be absorbed by fume present in the laser scanning path. As a result, further defocuses and scattering can be the consequences of the present fume in the laser path. In the research of Shcheglov et al. [77] confirmed the maximum laser beam attenuation by the vapor fume was estimated to be up to 40%. It is known that fiber lasers are unlikely to undergo attenuation by the generation of plasma as other laser equipments [78]. Therefore, the fume is responsible for the laser beam attenuation. Evidence of the fume generation during CW laser irradiation is provided in the high speed camera photo of Figure 3-18.

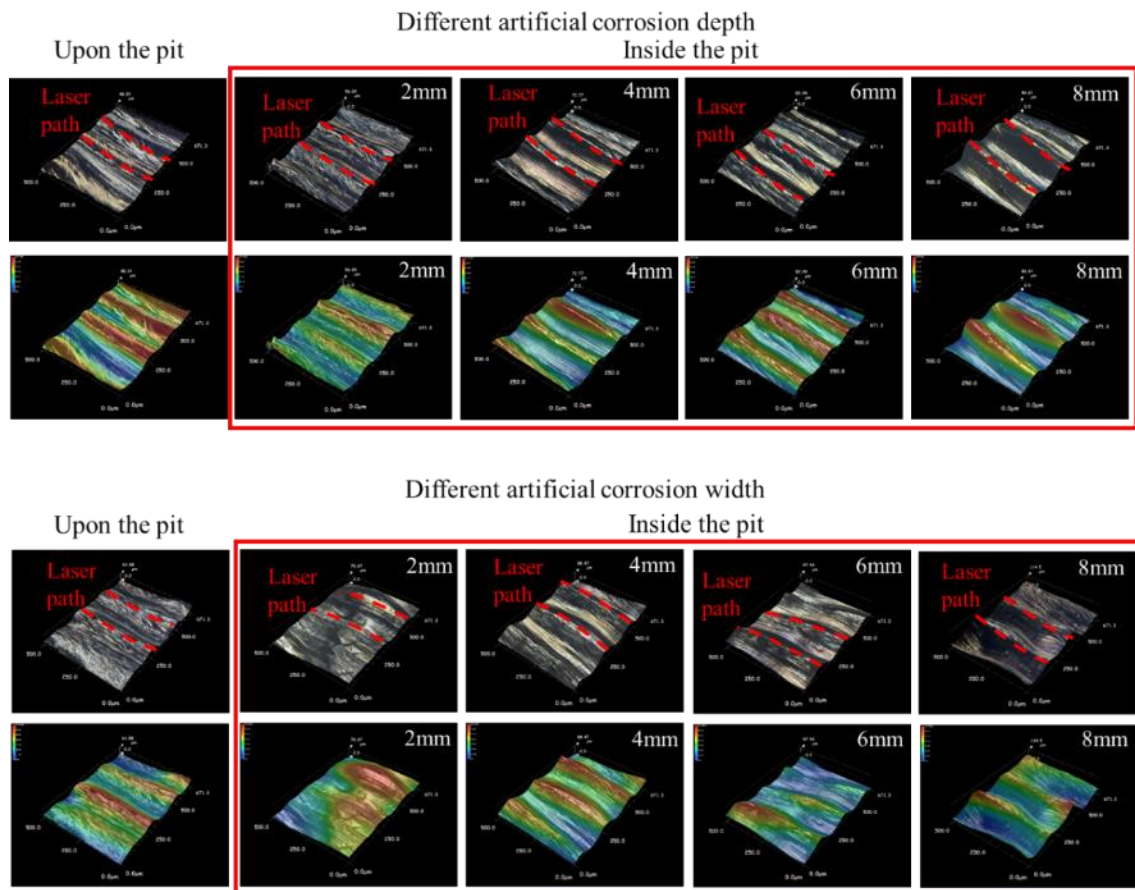


Figure 3-17 Surface morphology of laser-treated specimens with artificial corrosion pits.

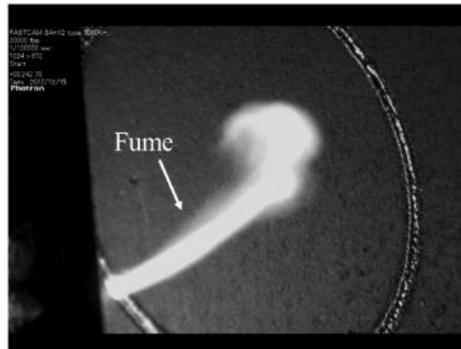


Figure 3-18 High speed camera of the fume generated during CW laser irradiation.

Besides the fume generation, any slight oblique angle of laser beam towards the corrosion pits would result in blocking effect by the discontinuous surface, narrow pit width are more likely to block the laser beam, as shown in Figure 3-19. Thereby the laser power is restricted due to the laser beam reached pit bottom is actually reflection. On the other hand, the size of corrosion pits also limited the irradiation time of rotating laser beam, thus preheating effects were confined under smaller pit width. As the laser absorptivity of steel material will improved with improving temperature [79], the laser energy transfer to bottom surface of corrosion pit might be lower due to shorter irradiation time and preheating process.

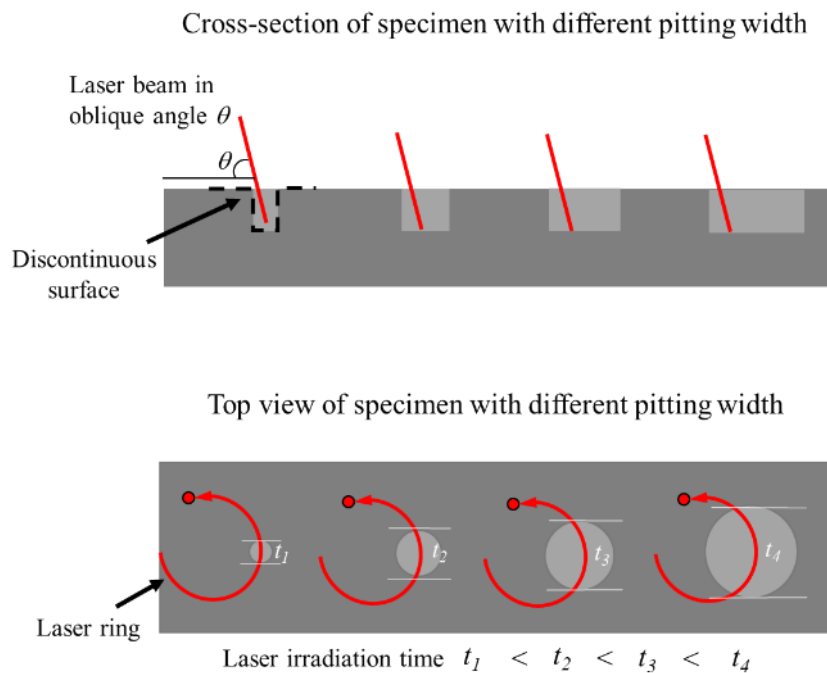


Figure 3-19 Schematic illustration of the effects of pitting width on laser irradiation.

The element distribution of Fe and O on the laser-treated steel surface is presented in Figure 3-20 of SEM-EDX observation results. From the amount of oxygen presented, the oxygen reduced with deeper corrosion pit. However, the content is still similar to upper steel surface as presented in Figure 3-10 of LA specimen. However, the oxygen tend to lower under the condition of 2 mm pit width. The result is corresponding to the surface morphologies illustrated in Figure 3-17.

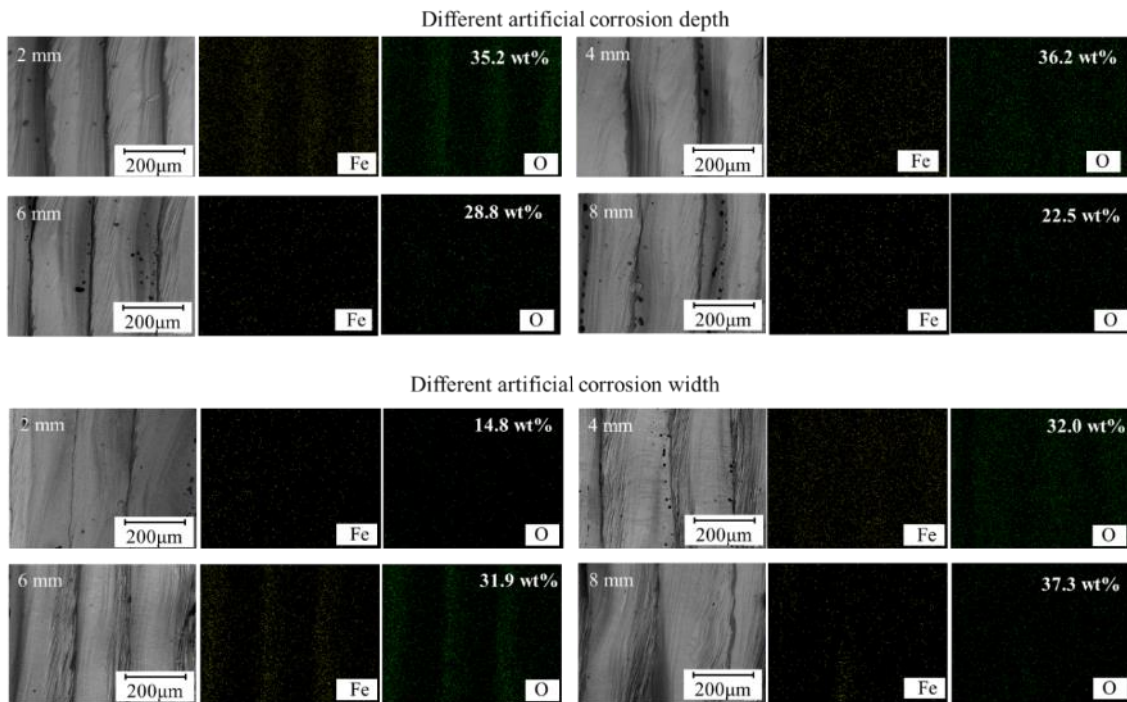


Figure 3-20 SEM-EDX analysis on laser-treated specimens with artificial corrosion pits.

However, the laser paths still confirmed effectiveness of laser treatment inside corrosion pits with different width and depth. Take the residual salts into account, the melting point and boiling point of NaCl are 1074K and 1738K respectively, much smaller than the steel material (melting point 1698K, boiling point 3273K). This level of laser power still enough to remove residual salts inside the corrosion pits.

3.7 Summary

In this chapter, the surface characteristics and microstructure of laser-treated steel plates were evaluated using OM microscope, SEM-EDX and XRD diffraction. The effects of laser ring moving speed on treatment coverage were investigated basing on the surface appearance of laser-treated carbon steel. Steel plates with different depths and widths of artificial corrosion pits are manufactured to evaluate the laser defocus influence on treatment effectiveness. Basing on the result, the following summary can be drowned:

- (1) Surface morphologies of the laser-treated specimens indicating the laser scanning tracks are dominated by the combined effects of processing parameters. Generally, higher laser power density and longer interaction time contribute to more thermal effects, while under the same laser power density, shorter interaction time result in laser ablation dominate surface features (i.e. laser scanning tracks). The area in moving laser ring was divided into Region A (middle portion) and Region B (top/bottom portion). Due to laser overlapping effects, Region B possessed more irregular patterns than Region A, therefore surface roughness in Region B also increased. When the laser overlapping effects increased to a certain value, surface defects will take place as shown in LD2 and LD3 specimens.
- (2) Iron oxide formation during laser irradiation is related to the thermal effects induced by laser beam. As a result, higher laser power density improve the oxidation. The longer interaction time and higher power density are the key factors that result in surface oxidation. Furthermore, laser overlapping effects contribute to the repetitive melting and solidification, result in increasing iron oxide formation on the steel surface. XRD result revealed that greater heat transfer from the laser beam to the specimen promotes the formation of iron oxide at the higher oxidation state of $\gamma\text{-Fe}_2\text{O}_3/\text{Fe}_3\text{O}_4$. Higher laser power density and more overlapping effects are the reasons for improving oxide content.
- (3) The microstructure of laser-treated steel plates modified by the laser thermal effects, when the laser parameter could not satisfy the condition to

lead laser ablation as LC specimen shows, the microstructure near laser-irradiated surface mostly remain unchanged. For the other laser conditions, both MZ and HAZ were observed and presented similar components but different deepness. The microstructure in MZ layer changed after laser irradiation, martensite and bainite could be formed due to the rapid laser heating and cooling process. In the HAZ area, refined ferrite and perlite were observed, attributed to the thermal and non-thermal combination effects of laser ablation. The hardness within the MZ&HAZ was mostly improved, except for Region B in LD3 specimen. More laser overlapping effects were considered as the reason for decreasing hardness due to larger grain size generated in repetitive irradiation. Basing on the changing microstructure and surface characteristics, the electrochemical and mechanical properties of steel materials could be affected, which will be discussed in the following chapters.

- (4) Surface morphologies in different laser beam overlapping rates suggested the appropriate laser ring moving speed should satisfy at least 0% of the overlapping rate. Desirable laser treatment effectiveness is expected inside corrosion pits up to 8 mm depth in this study. Small width of corrosion pit will limit the thermal effects of laser irradiation, due to fume concentration and shelter effects of discontinuous surface. Yet promising cleaning efficiency of laser irradiation is still worth expecting.

CHAPTER 4 ELECTROCHEMICAL PROPERTIES OF LASER-TREATED CARBON STEEL SURFACE

4.1 Introduction

During field application of the high-power CW laser equipment, the laser beam could affect the base metal to a certain degree, due to human operation error and the purpose of acquiring comprehensive treatment. Extremely high temperature was induced by the laser beam during irradiation as analyzed in CHAPTER 2, the microstructure of base steel material and surface oxidation could take place due to the thermal effects. Therefore, laser treatment can also modify the corrosion properties of metallic material. It was found that the corrosion resistance of ferritic alloy improved after laser treatment, due to the formation of a protective oxide film [80]. A similar result was reported by Zhang et al. for Al Alloy [81]. On the other hand, the variation in microstructure may also affect the corrosion properties of the laser-treated materials [82][83]. The corrosion resistance of steel materials after surface preparation may be improved or reduced, relating to the surface morphology, surface strain, and surrounding environment [84][85].

In fact, the corrosion of metallic materials is an electrochemical process involving redox reaction. Electrons were released from the steel material, and caught by the elements in surrounding environment during corrosion process. Therefore, the flow of electrons can be controlled electronically to evaluate the corrosion properties of metallic materials. One of the useful techniques is potentiodynamic polarization test, which including working electrode (testing specimen), counter electrode, reference electrode and electrolyte solution. All the electrodes are immersed in electrolyte solution that represent the corrosive environment, and connected to a potentiostat. Electrochemical potential is applied between the electrodes in respect to reference electrode. And the current flow in the cell was constantly monitored. The corrosion current (i_{corr}) and corrosion potential (E_{corr}) can be defined by polarization test. The open circuit potential (E_{ocp}) is the potential of working electrode in respect to reference electrode without impressed current through the working electrode (i.e. open circuit). Stable E_{ocp} implying the electrochemical cell reached steady state in the open circuit condition. Another

commonly used electrochemical test is electrochemical impedance spectroscopy (EIS), EIS measure the impedance of the surface layer at different frequencies, this method used to evaluate the surface coverage of coating layer. With appropriate evaluation, EIS is an indication of protective effect of the surface. More intact passive layer on the steel surface contribute to higher impedance results.

To further evaluate the formation of oxide layer, and the effects of laser treatment on corrosion properties of the base metal, this chapter applied electrochemical test for laser-treated carbon steel. All the laser processing parameters were used during the irradiation procedure, including LA, LB, LC and LD1, LD2, LD3. The electrochemical test results were evaluated and compared with surface morphologies and microstructures after laser treatment, to establish the effects of the laser treatment on the corrosion properties of carbon steel plates, and the status of oxide layer.

4.2 Experimental

Before the electrochemical test, the specimens were degreased and cleaned using acetone and deionized water. The test surface was then covered by an electrochemical sample mask and exposed to a 100 mm² area to serve as the working electrode. A three-electrode system was adopted, with Ag/AgCl in a saturated potassium chloride solution used as the reference electrode, and platinum foil was embedded as the counter electrode. All electrochemical tests were conducted using a potentiostat (VersaSTAT 4, Princeton Applied Research) at room temperature. Naturally aerated 3.5 wt% NaCl solution prepared with deionized water was used as the electrolyte. The setup of electrochemical test is shown in Figure 4-1.

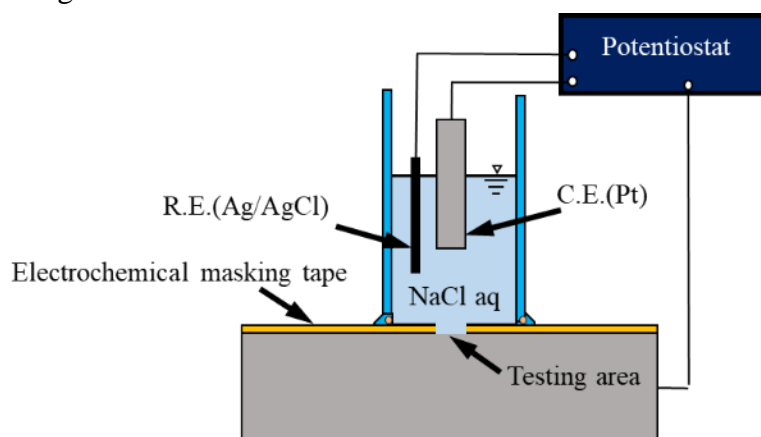


Figure 4-1 Equipment setup of the electrochemical test.

The E_{ocp} of the specimens was measured for 1 h, till it reached a stable value. Then, the polarization curves were tested in the range of $E_{ocp} \pm 250$ mV, with a scanning speed of 10 mV/min. The i_{corr} and E_{corr} were determined using the Tafel extrapolation method, commercial software VersaStudio (Princeton Applied Research) was used for the analysis of polarization results. EIS spectra with 10 mV signal amplitude were performed in the range of 10 mHz to 100 kHz with respect to E_{ocp} . Commercial software ZSimpWin (AMETEK) was used for the simulation analysis of the EIS results.

4.3 Electrochemical test results of laser-treated and unirradiated specimens

4.3.1 Potential-time measurements of specimens

The potential-time measurements of laser-treated and unirradiated specimens in 3.5 wt% NaCl solution are shown in Figure 4-2. Decreasing trends in potential for all specimens were observed, indicating a typical active dissolution of the specimen surface [86]. The laser-treated specimens exhibited nobler potential values under different processing parameters in comparison to unirradiated specimens, indicating a less tendency of corrosion for laser-treated steel surface from thermodynamics point of view [84]. As for similar surface roughness specimens of LA, LB and LC conditions according to Figure 3-9, the electrochemical changing would mainly attributed to the oxide layer and modified microstructures. From the 1 h E_{ocp} measurement shown in Figure 4-2(a), LA and LB specimens possessed similar potential values and trends, while LC presented more cathodic values than the laser-treated specimens. Associated with the oxide component results illustrated in Figure 3-12, potential shifting after laser treatment can be attributed to the presence of iron oxide formed on the steel surface [87]. The E_{ocp} during the initial phase mainly depends on the oxide proportions. More $\gamma\text{-Fe}_2\text{O}_3/\text{Fe}_3\text{O}_4$ is related to higher potential values. In fact, $\gamma\text{-Fe}_2\text{O}_3/\text{Fe}_3\text{O}_4$ is considered an important component of the protective layer [88]. A longer immersion time of 24 h was also conducted on the laser-treated and unirradiated specimens, as shown in Figure 4-2(b). From the transients obtained, it is obvious that laser-treated carbon steels maintain nobler potential values than the unirradiated carbon steel with time lapse. Abrupt potential decay during the first two hour of immersion was observed in the unirradiated specimens, after which the equilibrium state at which the oxidation equals reduction was achieved. On the other hand,

the laser-treated samples presented a delay to reach the equilibrium state, showing approximately 8 h, 16 h, and 20 h for LC, LB, and LA specimens, respectively. Eventually, the E_{ocp} of LA reached the highest stable value of $-622 \text{ mV}_{\text{Ag}/\text{AgCl}}$, followed by LB of $-655 \text{ mV}_{\text{Ag}/\text{AgCl}}$ and LC of $-665 \text{ mV}_{\text{Ag}/\text{AgCl}}$. The unirradiated specimens possessed the most cathodic values of $-683 \text{ mV}_{\text{Ag}/\text{AgCl}}$ at the equilibrium state. In addition, martensite and bainite are found to have nobler potential than ferrite [89][90][91], as well as a more refined grain size [92][93]. After 24 h of immersion in aggressive 3.5 wt% NaCl solution, the oxide film on laser-treated steel surfaces could be dissolved, especially in the lowest oxide content situation in LC specimens. Therefore, the MZ or HAZ may be exposed to the electrolyte and may partially contribute to the nobler potential value.

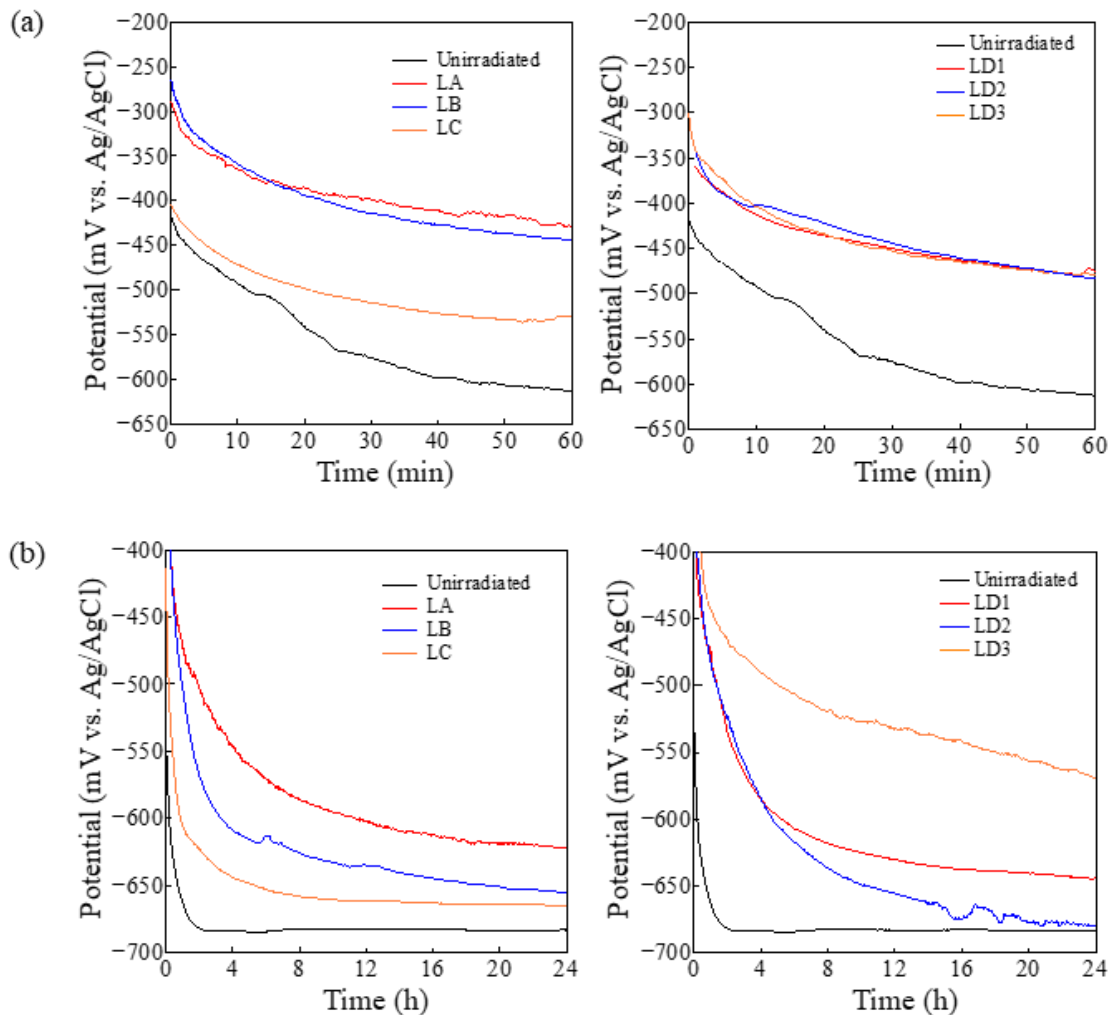


Figure 4-2 Potential-time measurements of laser-treated and unirradiated specimens immersed in 3.5 wt% NaCl solution for (a) 1 h and (b) 24 h.

When the laser overlapping effects increased, the surface roughness changed

significantly as shown in the LD1, LD2 and LD3 results of Figure 3-9. In the short time immersion test as shown in the 1 h potential-time measurements of these specimens, all of the potential values of the specimens presenting similar values, and higher than unirradiated specimen. It is considered that the iron oxide still playing an important role in the short time immersion test, because most of the iron oxide remained after 1 h encounter with the electrolyte. However, the content of iron oxide only one influence factor among the others. Noticing that LD1 has much more deeper MZ than LC specimen, and the MZ layer suppose to provide part of function for improving E_{ocp} . 1 h potential-time measurement of LD3 specimen indicating the nobler potential value are mainly attributed to the presence of iron oxide, especially γ -Fe₂O₃/ Fe₃O₄ content in the oxide layer. In the longer immersion time of 24 h, as shown in Figure 4-2(b), LD3 specimen maintaining the highest potential value of -569 mV_{Ag/AgCl}, followed by LD1 specimen of -644 mV_{Ag/AgCl} and LD2 specimen of -679 mV_{Ag/AgCl}. The equilibrium state of LD1, LD2 and LD3 were delayed compares to unirradiated specimen, and presenting approximately 8, 9 and 12 h for LD3, LD1 and LD2 conditions respectively. The high iron oxide amount in the LD3 specimen was considered as the principal cause of noblest potential value among all the laser treatment conditions. However, LD2 condition also possessed higher iron oxide content in comparison to LD1 condition, more cathodic potential value was observed in this laser condition. From the cross-section profile and surface roughness presented in Figure 3-8 and Figure 3-9, LD2 specimens possess more obvious grooves on the surface, and the roughness is higher than the other laser conditions either in Region A or Region B. The rougher surface condition and grooves on the surface will trap the corrosive ions and products inside, and inducing more severe pitting corrosion [94]. Consequently, the corrosion are more prone to occur in the surface defects and grooves [95]. Also noted that the LD2 has similar MZ&HAZ depth with LD1 condition as shown in Figure 3-14. The amount of iron oxide and modified microstructure is not enough to resist pitting corrosion in the surface grooves, thus an abrupt decrease was presented after 15 h of immersion due to the dissolution of iron oxide and the underneath, and the potential value become relatively unstable after then. The extremely deep MZ&HAZ and large quantity of high state iron oxide on the surface of LD3 ensured the nobler potential with time lapse.

Overall, the effects of laser surface treatment on the E_{ocp} of carbon steel are combined influence of surface roughness, iron oxide content and modified microstructures. The presence of iron oxide and modified microstructures provided the factors that nobler will be obtained. The surface roughness, amount of iron oxide and deepness of the modified microstructures decided stability of the E_{ocp} with time lapse. Generally, larger and higher state iron oxide, deeper modified microstructures and lower surface roughness contributed to a nobler and stable E_{ocp} .

4.3.2 Potentiodynamic polarization curves of laser-treated and unirradiated specimens

The potentiodynamic polarization curves of laser-treated and unirradiated specimens after 1 h immersion in 3.5 wt% NaCl solution are presented in Figure 4-3. From the test results of all laser conditions, the E_{corr} illustrated in the polarization curves corresponds with E_{ocp} . As for the potentiodynamic polarization of LA, LB and LC specimens, the highest E_{corr} value was obtained under LA conditions. It is seen that the anodic current densities are reduced after laser treatment, whereas the cathodic current densities are similar for both laser-treated and unirradiated specimens. The reduction of anodic current density is higher under LA and LB conditions, which leads to a more positive shift in E_{corr} . The E_{corr} of LD1, LD2 and LD3 specimens also cooperate with the E_{ocp} in 1 h immersion. Similar E_{corr} values were observed in these laser conditions, as the dominant factor for noble E_{corr} is the presence of iron oxide. However, the anodic slope of LD3 specimen exhibited higher than the other laser conditions, with decreasing in the current density. This phenomenon indicated an inhibition effects of anodic dissolution of the specimen surface own to the protective iron oxide layer formation and modified microstructures[96]. Under higher thermal effects of LD3 condition, the amount of iron oxide and deepness of modified microstructures layers reached highest level, thus more protective effects presented in this laser condition.

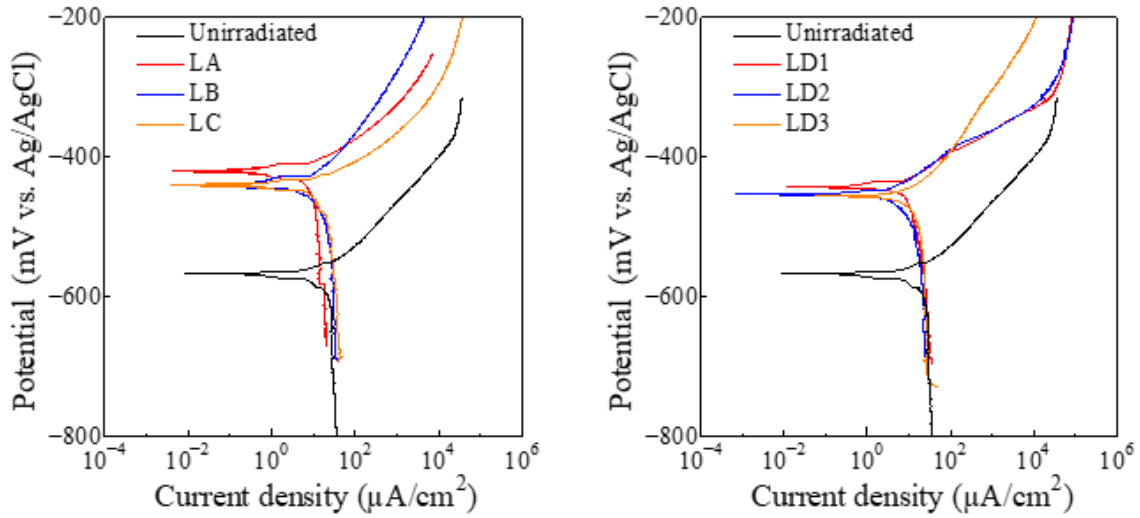


Figure 4-3 Potentiodynamic polarization curves of laser-treated and unirradiated specimens in 3.5 wt% NaCl solution.

Table 4-1 lists the fitted electrochemical properties based on the anodic polarization curves. The corrosion protective efficiency (P_{EF}) of the modified surface after laser treatment was calculated using the following equation [97]:

$$P_{EF} = \frac{i_{corr,0} - i_{corr,L}}{i_{corr,0}} \quad (4-1)$$

where $i_{corr,0}$ is the corrosion current density of the unirradiated specimens and $i_{corr,L}$ is the corrosion current density of laser-treated specimens. This equation gives a simple indicator of the integrity and stability of the iron oxide and modified microstructure layers.

Table 4-1 Fitted electrochemical parameters of specimens in 3.5 wt% NaCl solution.

Surface treatment	E_{corr} (mV _{Ag/AgCl})	b_a (mV/decade of current)	i_{corr} ($\mu\text{A}/\text{cm}^2$)	P_{EF} (%)
Unirradiated	-566	64.3	24.0	/
LA	-420	48.9	10.0	58.1
LB	-440	76.5	11.2	53.1
LC	-443	40.4	18.0	25.2
LD1	-443	41.0	17.3	27.9
LD2	-453	44.3	19.6	18.3
LD3	-456	65.1	13.1	45.4

From the i_{corr} listed in Table 4-1, the laser-treated specimens possessed lower current density values as compared to the unirradiated specimens. Generally, i_{corr} is one of the most important parameters for evaluating corrosion performance. A lower i_{corr} indicates

better corrosion resistance [98]. The calculated P_{EF} using i_{corr} gives a rough represent for the early corrosion resistant of laser-treated specimens. From the calculated P_{EF} , LD3 and LD2 specimens possessed the highest and lowest P_{EF} of 63.7 % and 18.3 %, respectively, while LB specimens had similar P_{EF} with LA specimens, similar values were presented in LC and LD1 conditions. The improved corrosion resistance after 1 h of immersion mainly contributed to the formation of iron oxide on the steel surface. According to the XRD results shown in Figure 3-11 and Figure 3-12, the oxide content in LA and LB are similar, same as LC and LD1 specimens. Considering the 1 h potential-time measurement results, the oxide film of LA and LB specimens acted as the main passive layer during this period, also LC and LD1 specimens. Besides, the LD3 specimen possessed highest iron oxide content, with most noble E_{ocp} in longer immersion period. Therefore, the P_{EF} is mainly attributed to the content of iron oxide. Similar oxide content resulted in close P_{EF} . However, the decrease in P_{EF} of LD2 specimens may be derived from the rough surface condition. Although a relatively higher iron oxide content was observed on the LD2 surface, but the presence of grooves and surface defects might induce localized corrosion, and lower the protection efficiency of iron oxide and modified microstructure layers. The potential-time measurement also revealed a similar trends of the unstable film of LD2 laser condition. In addition, the LD3 specimen has the roughest surface condition, but at the same time the most iron oxide content and deepest modified microstructures insured the protective efficiency of the laser modified steel surface.

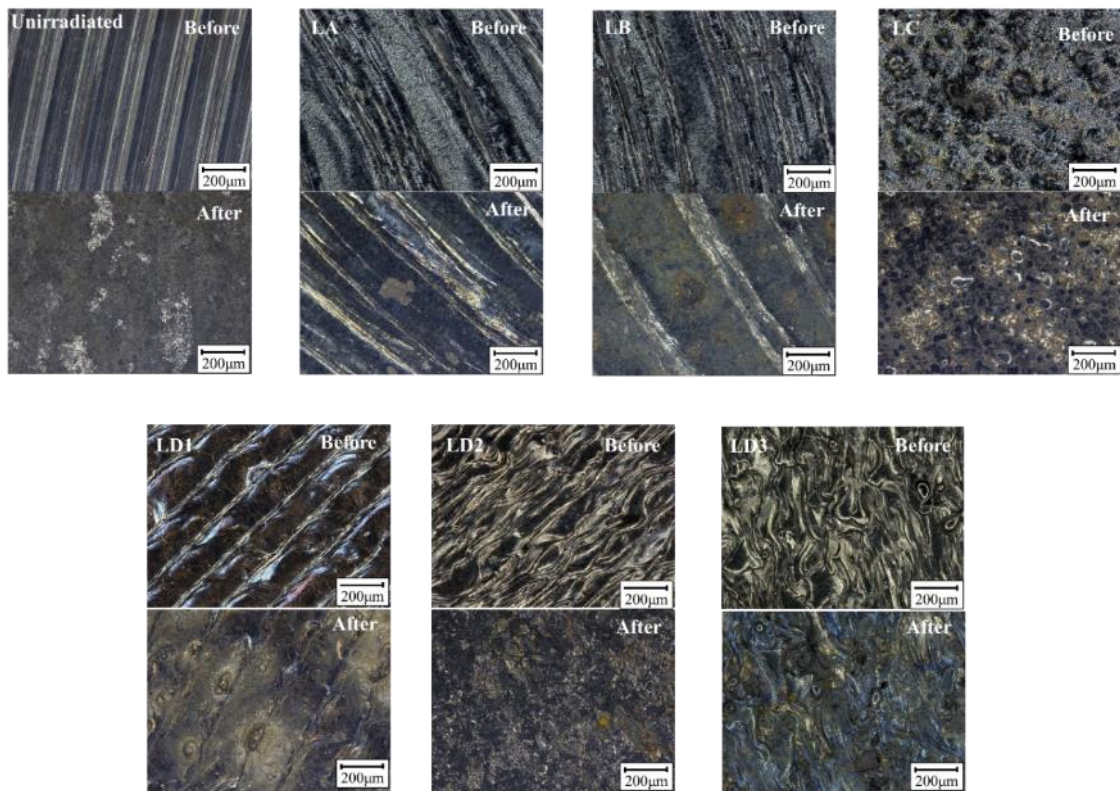


Figure 4-4 Surface morphologies of specimens before and after potentiodynamic polarization test.

Figure 4-4 shows the surface conditions of the specimens after the polarization test. The unirradiated specimen was observed to suffer more severe corrosion than the laser-treated specimens. It can be observed that with increasing laser power density and interaction time, the corroded area on the steel surface was gradually restricted according to LA, LB and LC conditions. From the corrosion status revealed in the laser-treated specimens, most of the corrosion locations appeared near the laser scanning tracks in LA, LB and LD1 conditions, or around the pores in the LC condition. Note that the oxygen contents in the above-mentioned positions are lower according to the EDX results presented in Figure 3-10. It can be assumed that corrosion on the surface of laser-treated specimens was initiated in the regions with less protective oxide film formation. This result also consistent with the previous potential-time measurement and potentiodynamic analysis, iron oxide formation is the most important passive layer for the laser-treated specimens. Among the laser-treated specimens, LD3 specimen presented a surface condition with the slightest corrosion, only the surface gloss was changed after potentiodynamic test. The surface of LD2 specimen after test exhibited most severe

corrosion within the laser-treated specimens. Original surface features of irregular oxide luster was vanished and replaced by corrosion products. The less protective laser-treated steel surface is thereby confirmed through the potential-time measurement and potentiodynamic test.

4.3.3 EIS analysis on the laser-treated and unirradiated specimens

The EIS results of the laser-treated and unirradiated specimens are shown in Figure 4-5. From the Nyquist plots illustrated in Figure 4-5 (a), nonstandard semicircles were observed in all specimens, which may be the consequence of unevenness and roughness of the steel surface [99]. The diameter of the Nyquist loops of laser-treated specimens was larger than that of the unirradiated specimens, which indicates that the laser treatment had positive effects on the early corrosion resistance. For laser condition of LA, LB and LC, the semicircle diameter of the LA specimen was significantly larger than that of the others, followed by the LB specimen. Particularly, the LC specimen exhibited semicircles similar to those of the unirradiated specimens, showing the least laser effects on the steel surface. When the laser overlapping effects increased, as shown in the results of LD1, LD2 and LD3 specimens, the semicircle of Nyquist plots presenting the diameters descending order follow the sequence of LD3, LD1, and LD2. Where LD3 exhibited the larger semicircle than the others, attributed to the iron oxide and modified microstructures as discussed in the previous section. The LD1 condition created a laser-treated surface with a Nyquist plot as large as LB condition, besides the iron oxide layer, the underneath microstructure also contribute to a more stable passive layer, due to the refined grain size and gradient distribution. However, the decreasing in the semicircle of LD2 specimen should be attributed to the rough surface condition with relatively less iron oxide formation and modified microstructure layer, as the same reason for more cathodic E_{ocp} and larger i_{corr} .

EIS spectra in the form of Bode plots express absolute impedance $|Z|$ are shown in Figure 4-5 (b) and (c). As can be seen in the plot, the absolute impedance $|Z|$ of the laser-treated specimens was higher than that of the unirradiated specimens. As for LA, LB and LC laser conditions, the absolute impedance of LA specimen was much greater than that of the other two. For the LD condition in different overlapping effects of LD1, LD2 and LD3, evident higher $|Z|$ were presented in all of the conditions. However, the LD3

condition still possessed the highest $|Z|$ value, while the LD2 specimen has lowest $|Z|$ value.

The Bode plots of phase angle of specimens were illustrated in Figure 4-5 (c). Within the laser condition of LA, LB and LC, it can be seen that LC and unirradiated specimens possessed higher phase angles around -60° to -63° , in the frequency range of approximately 3 Hz to 8 Hz, confirming the formation of a less protective oxide film on the steel surface [100]. Moreover, the phase angles of the LB, LC, and unirradiated specimens shift significantly at approximately 20 kHz, manifesting a less protective oxide film at higher frequencies. In contrast, LA specimens showed a stable protective layer across the examined frequency range. The phase angle plot of LD1, LD2 and LD3 exhibited a similar higher angle for unirradiated and LD2 specimens in the range of -60° to -63° , at around 3 to 8 Hz frequency range. Indicating the less protective laser-treated surface under LD2 condition.

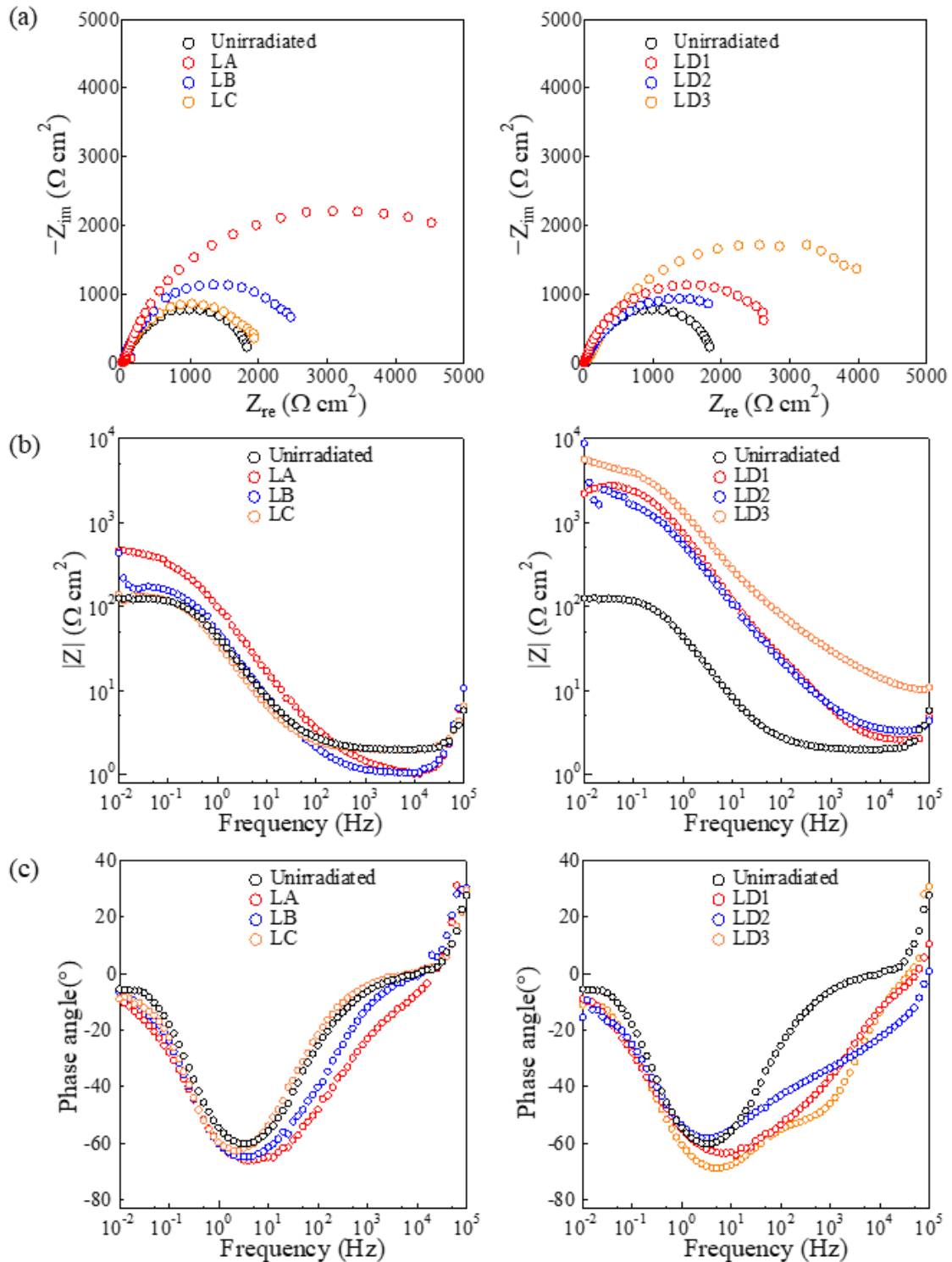


Figure 4-5 EIS results of laser-treated and unirradiated specimens in 3.5 wt% NaCl solution showed by (a) Nyquist plots, (b) Bode plot of magnitude Z and (c) Bode plot of phase angle.

To further investigate the surface modification effects after laser treatment, two types

of equivalent circuits were adopted to analyze the EIS data, as shown in Figure 4-6. The EIS data of the unirradiated specimens were fitted by the equivalent circuit, as illustrated in Figure 4-6 (a), representing the situation of the steel surface without the iron oxide film. The data of laser-treated specimens were fitted in the equivalent circuit of Figure 4-6 (b) to describe the existence of laser-affected layer (i.e. iron oxide film and modified microstructures). These equivalent circuits were proved to be adequate for specimens with or without the passive layer on the surface [87][99][101]. As a result, the electrochemical properties of different surface conditions can be compared. The equivalent circuits used in this study were composed of solution resistance (R_s), constant phase element of the oxide film (CPE_f), resistance of the oxide film (R_f), constant phase element of the double electrical layer (CPE_{dl}), and the charge transfer resistance (R_{ct}).

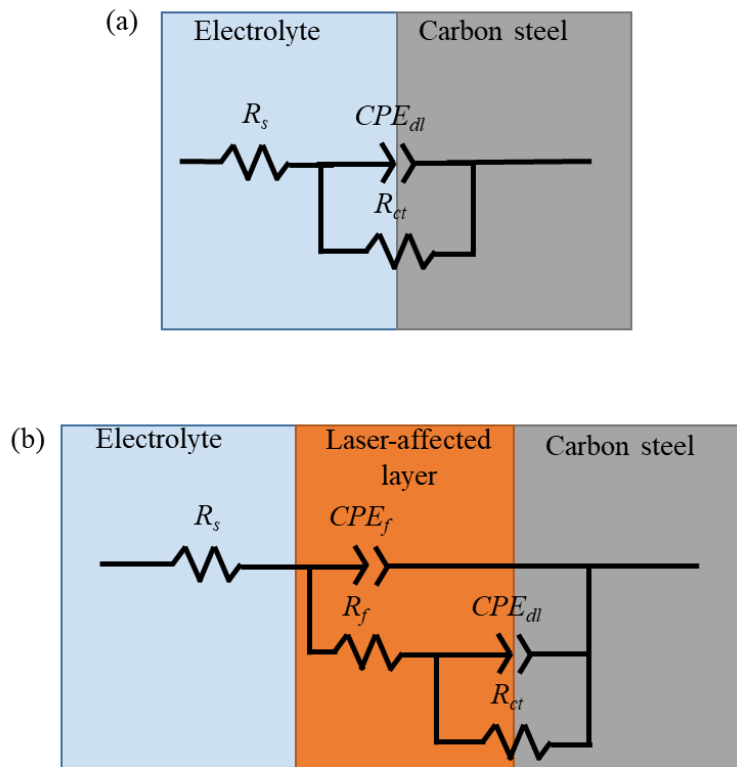


Figure 4-6 Equivalent circuit used to fit EIS data of (a) Unirradiated specimen and (b) Laser-treated specimen.

The surface coverage (θ) of the iron oxide can be calculated using the polarization resistance (R_p) of the specimens[87]:

$$\theta = 1 - \frac{R_p^0}{R_p} \quad (4-2)$$

in which the R_p is calculated by:

$$R_p = R_f + R_{ct} \quad (4-3)$$

where R_p^0 is the polarization resistance of the unirradiated specimens and R_p is the polarization resistance of the laser-treated specimens.

A denser and less defective surface will lead to a higher θ [102], resulting in improved corrosion resistance of laser-treated specimens. From the θ results of LA, LB and LC conditions listed in Table 4-2, the LA specimen possessed the highest θ among the laser-treated specimens, presenting 71.8 % coverage. LB specimens have a relatively lower value of 29.9 % coverage compared with LA specimens. The lowest θ was found to occur under LC conditions, with 3.70 % coverage. The surface coverage results correspond with the XRD semi-quantitative results of iron oxide formed on the specimen surface, as illustrated in Figure 3-12. Confirming the modified corrosion resistance is mainly attributed to the presence of iron oxide after laser treatment, and a higher proportion of oxide content leads to better corrosion resistance. The results are consistent with the study of Maharjan et al.[103]. Their work on the corrosion behavior of laser hardened steel suggests that improving corrosion resistance is mainly related to the oxide film. However, the lower surface coverage and oxide content in LC specimens suggest that modified microstructures under the oxide film have beneficial effects on the corrosion resistance. In fact, some of the microstructures have been proven to obtain better corrosion resistance, such as bainite and perlite [104]. Although the microstructures in the MZ of the laser-treated surface are complicated owing to the gradient temperature distribution and non-uniform heating-cooling process, it is possible that these microstructures may further improve the corrosion resistance of carbon steel according to the electrochemical test results.

The θ of LD1, LD2 and LD3 specimens presenting a higher value of 64.4% obtained under LD3 condition, which is also attributed to the iron oxide formation. On the other

hand, the LD1 and LD2 specimens have similar θ value, despite of the higher iron oxide content in LD2 condition. Noticing that the surface coverage θ is a parameter showing the surface integrity and density, the surface defect presented in the LD2 and LD3 conditions could be a damage for the θ value. Thus a less intact surface were observed in these two laser conditions basing on the EIS analysis.

Table 4-2 Fitted impedance parameters from EIS of laser-treated and unirradiated specimens.

Specimens	R_s ($\Omega \text{ cm}^2$)	CPE_f ($\Omega^{-1} \text{ s}^n \text{ cm}^{-2}$)	n	R_f ($\Omega \text{ cm}^2$)	CPE_{dl} ($\Omega^{-1} \text{ s}^n \text{ cm}^{-2}$)	n	R_{ct} ($\Omega \text{ cm}^2$)	θ (%)
Unirradiated	30.0	–	–	–	3.11×10^{-4}	0.806	1969	–
LA	16.4	1.34×10^{-5}	1.00	18.9	1.40×10^{-4}	0.763	6963	71.8
LB	15.4	1.74×10^{-4}	0.842	94.1	9.38×10^{-5}	0.846	2716	29.9
LC	29.2	2.01×10^{-4}	0.883	61.7	1.61×10^{-4}	0.826	1983	3.70
LD1	13.1	3.04×10^{-5}	1.00	17.0	2.53×10^{-4}	0.791	3040	35.6
LD2	14.2	2.72×10^{-5}	0.973	9.47	3.28×10^{-4}	0.718	2841	30.9
LD3	19.5	8.86×10^{-5}	0.679	75.1	9.26×10^{-5}	0.761	5453	64.4

Overall, the electrochemical analysis on the laser-treated specimens confirmed a better early corrosion resistance of carbon steel after laser irradiation. The main contribution for improving corrosion properties is the presence of iron oxide, and the modified microstructures. However, the surface roughness and defects also play an important role when the laser overlapping effects improved to a higher level. The surface defects remain on steel surface will result in a weaken area, where the localized corrosion take in place. The contour plots of laser-treated steel plates before and after potentiodynamic polarization test are shown in Figure 4-7. From the appearance it is obvious that most of the laser-treated specimens has similar corroded profile after the polarization test, except for LD2 condition. Increasing altitude difference was presented on the LD2 specimen surface, from 55.8 μm ascended to 79.7 μm . The altitude difference represented deepness of pitting corrosion, as shown in Figure 4-7. Therefore, more severe pitting corrosion was confirmed on the LD2 surface, which is the evidence of decreasing corrosion resistance as described in Table 4-1 and Table 4-2.

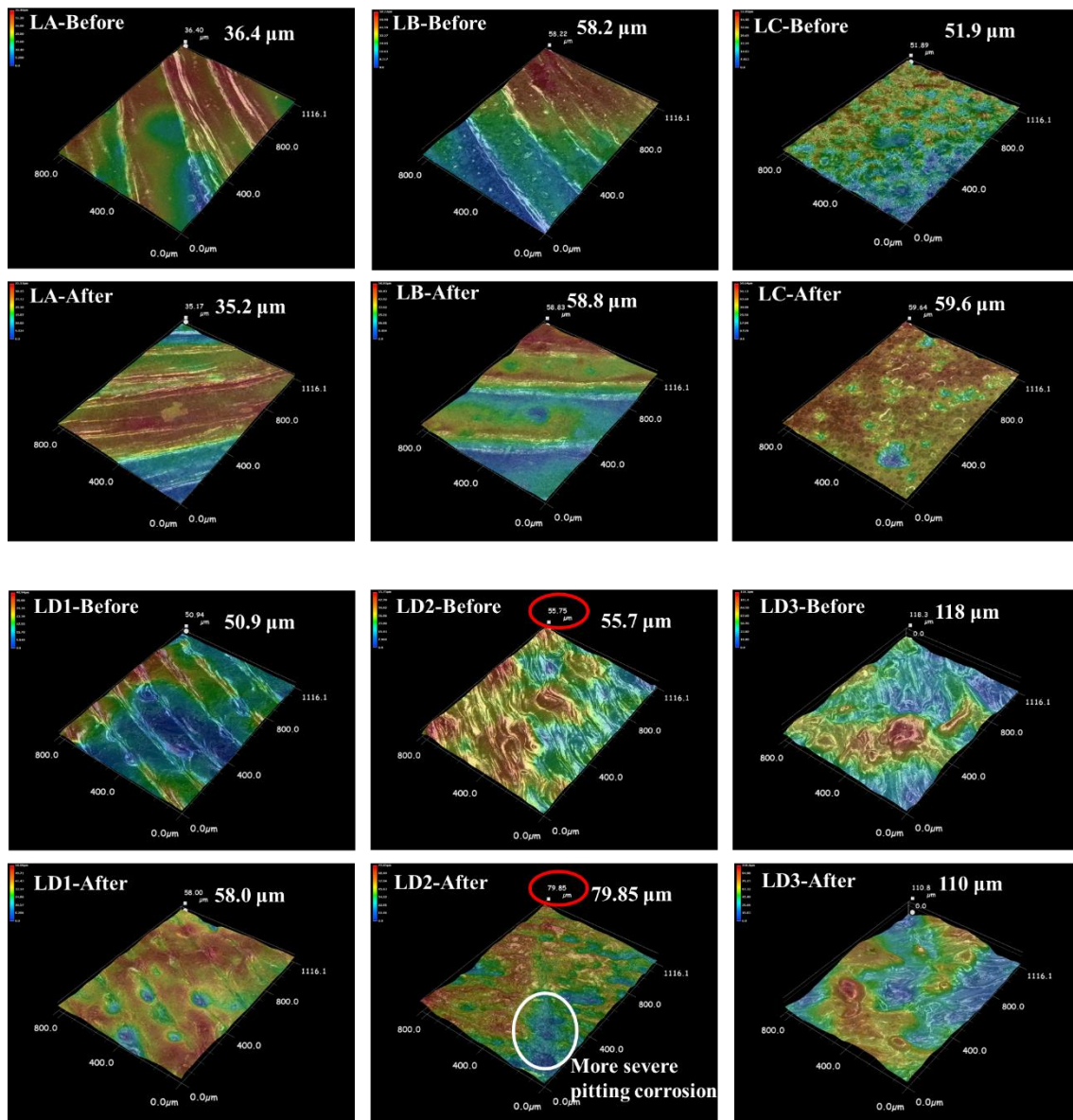


Figure 4-7 Contour plot of laser-treated specimens before and after potentiodynamic polarization test.

The corrosion progress of steel plate irradiated by different laser condition were illustrated in Figure 4-8. As for LA, LB, LC and LD1 conditions, the steel surface after laser irradiation presenting smoother features. Under the presence of iron oxide, aggressive chloride and oxygen were isolated by this protective layer. The improving corrosion resistance is depended in the amount and component of the iron oxide layer. As different early corrosion properties showed in the LA, LB, LC and LD1 specimens with different iron oxide content. The change in iron oxide amount of these laser conditions is

related to laser power density and interaction time. Higher power density and longer interaction time contributed to more iron oxide formation. When the laser overlapping effects increased, as shown in LD2 condition, the amount of iron oxide reached higher level, with slightly deeper modified microstructures. Yet a rougher surface with grooves existence concentrate of the corrosive ions [105], the localized corrosion destroyed the passive layer all the way down to the base metal easily. Thus a less protective laser-affected surface is presented in the LD2 condition. When the laser overlapping effect goes up, the oxide layer and modified microstructures further increased. Although the rough surface still induce localized corrosion, the extremely deep laser-affected layer protect the base metal throughout the test period, as shown in Figure 4-8.

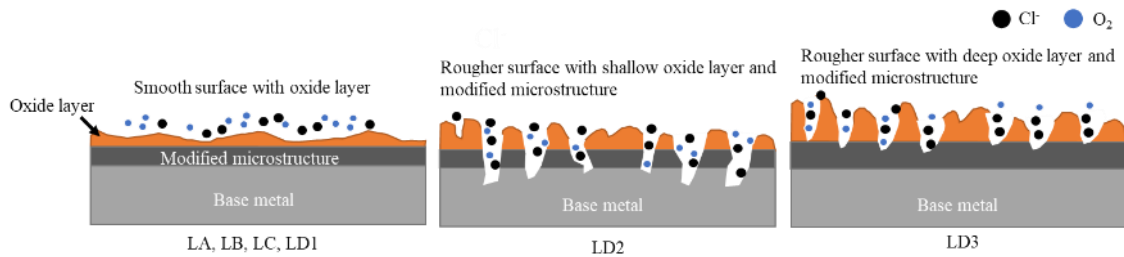


Figure 4-8 Schematic illustration of corrosion progress under different surface condition.

On the basis of all the above-mentioned test results, the surface of laser-treated carbon steel is confirmed to have better corrosion resistance. Under appropriate laser condition, no distinct damage to the surface morphology and corrosion properties manifest that laser cleaning is a promising preparation method for steel structures, and the improved corrosion resistance can be regarded as temperate corrosion protection on some occasions. However, the oxide film on the laser-treated steel surface may affect the coating quality if a repainting process is required. Future studies need to assess the the coating qualities of specimens before and after removing the laser-induced oxide film.

4.4 Summary

To determine the effects of high-power CW laser irradiation on the electrochemical properties of carbon steel plates, as well as the status of laser-affected layer. The potential-time curves, potentiodynamic polarization test and EIS of laser-treated carbon steels were investigated. From the test results, the following conclusions can be drawn:

- (1) Electrochemical test results indicated that CW laser-treated specimens have better corrosion resistance. The improved corrosion resistance was mainly attributed to the laser-induced oxide film formation. In less laser overlapping effects, denser and fewer defects in the oxide film were obtained under higher laser power density and interaction time. The results of the specimen with the least oxide film protection suggest that the modified microstructures also have beneficial effects on the corrosion properties.
- (2) The irregular surface profile and defects result from higher laser overlapping effects induce localized corrosion on the laser-treated steel surface, and weaken the protection effects of oxide film and modified microstructures. Thus a limit for the laser ring moving speed is required to restrict surface defect during laser irradiation. The calculation method for peak temperature distribution in CHAPTER 2 could be useful to avoid severe thermal effects derived from laser surface treatment.
- (3) Although the laser-treated carbon steel has corrosion resistance attributed to laser-affected layers, future research should further investigate the corrosion protection of laser-affected layer through atmospheric exposure test or accelerate corrosion test, due to the presence of oxide layer may induce pitting corrosion. The practicability of laser surface treatment would be improved if the laser-affected layer possess desirable corrosion resistance in long-term exposure.

CHAPTER 5 TENSILE PROPERTIES OF LASER-TREATED STEEL COUPON

5.1 Introduction

Although laser surface treatment has the potential to achieve desirable surface conditions, heat effects during laser irradiation may damage the material and influence the mechanical properties of steel members. Moreover, the input laser energy may also affect some components of steel structures, for example, the bolted connections and narrow positions. In the surface treatment area using laser technology, pulsed laser is the common equipment due to the treatment object is often small size, precise members, such as the titanium alloys used in aerospace and medical sectors [106], or aiming at the shallow oxide layer removal [107]. Compares to the high power CW laser used in this study, the pulsed laser possessed relatively lower thermal effects. The modification of pulsed laser on the metallic surface has limited effects, usually surface oxidation and superficial hardened layer can be formed after pulsed laser irradiation. No obvious surface defects can be observed after pulsed laser irradiation, cause the laser ablation effects induced by pulsed laser is approximate mechanical cutting rather than thermal effects [108]. Studies concerning the mechanical properties after pulsed laser irradiations presenting almost unchanged after laser irradiation [107]. But the laser peening technique contribute to a hardened layer [109], which might be beneficial for improving fatigue life of the laser-treated metallic materials. In some cases, microstructures on the laser-treated metal surface will transform into a gradient distribution along the direction of depth [110][111], consequently improving the mechanical properties of the metal surface.

To date, there is no study concerning the high power CW laser surface treatment on the mechanical properties of steel material, the combined effects of thermal and non-thermal in laser ablation procedure are worried to be harmful to the mechanical properties of steel materials. This study applied high-power CW laser to irradiate the carbon steel surface, and compared it with non-thermal abrasive blasting method. The relationship between changes in mechanical properties and laser energy density is established using tensile test and high vacuum SEM fractography.

Basing on the fractography, fracture can be described in terms of the macroscopic or microscopic details of the fracture surface, that is, macrofractography and microfractography respectively. On a macrofractography, ductile and brittle fracture surfaces as shown in Figure 5-1 can be described by various fracture features. High amounts of plastic deformation prior to fracture is the characteristics of ductile fractures. The cup and cone, slant fracture features are the common fracture surface of ductile failure as shown in Figure 5-1. On the other hand, the brittle fracture presenting a square fracture, on account of less plastic deformation before fracture. In microfractography, ductile fractures usually initiate from voids, or inclusions, forming distinct equiaxed or elongated dimples [112]. While the brittle failure will generate from two different mechanisms, cleavage fracture and intergranular fracture. The cleavage fracture occurs across crystallographic planes creating distinct river patterns, which helps to determine the crack progression. In intergranular fracture, also known as rock candy fractures, are low energy failures that occur along the weak grain boundaries [113].

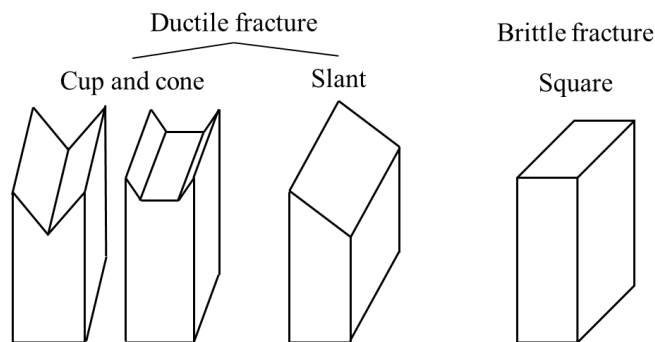


Figure 5-1 Schematic of macrofractography of the fracture surface.

5.2 Experimental

Carbon steel coupon (JIS G3106 SM400A) were manufactured based on JIS Z2201 for surface treatment and tensile test, as shown in Figure 5-2. All specimens were abrasive blasted according to ISO Sa 2.5 before laser irradiation to achieve identical surface condition, and the steel coupon only treated by abrasive blasting were also used as comparison to laser surface treatment. Basing on the previous analysis, the thermal effects on LA and LB specimens are similar to each other, major difference is the surface oxide compositions. The thin oxide layer on steel surface only affects electrochemical properties rather than mechanical properties. In consideration of the relationship between

mechanical properties and heat affected layers, the laser conditions adopted for the surface preparation were LA and LC, to represent the varying laser power density and interaction time, also LD1, LD2 and LD3 to investigate the laser overlapping effects on the mechanical properties of steel material. The laser irradiation were conducted on both side, interval time was prepared before irradiate the other side to prevent unstable heat conduction realated physical properties, for the purpose of similar thermal effects on the both sides. Three identical coupons of each surface treatment condition were prepared for the tensile test.

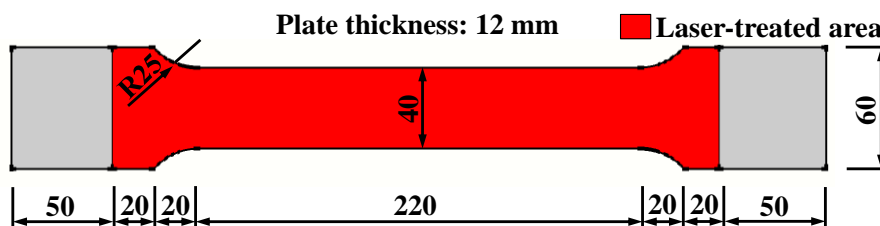


Figure 5-2 Size of tensile specimens basing on JIS Z2201.

During tensile test, all specimens were subjected to universal tension machine under displacement control of 0.03 mm/s, a Ω extensometer was utilized to track the elongation. The fractography was proceeded under macroscale and microscale observation, in which SEM was performed for microscale fracture morphology.

5.3 Tensile test results

The fracture types of each tensile test are exhibited in Figure 5-3. All the steel coupons shown similar fracture features from the appearance under the same surface preparation method, in the pictures here only typical images were presented. The photo shows obvious necking region occured at lower heat effects laser coditions of LA, LC and LD1. Then the necking becomes less noticeable under higher laser heat effects of LD2 and LD3 conditions. Especially for the LD3 condition, there was almost no necking phenomenon can be observed from the appearance. Usually, only ductile materials presenting necking after tensile test, and there is no necking region in brittl materilas, the material will simply fracture with a relatively flat plane at the fracture area. Since the material used in the tensile test is the same mild steel SM400A, different degrees of necking may suggest that laser thermal effects does impact the mechanical properties. In addition, basing on

the fracture position presented in LD2 and LD3 specimens, the initial failure portion may near the top/bottom portion where the surface defects and changing mechanical properties were observed as evaluated in CHAPTER 3. In this case, the laser overlapping effects are supposed to impact the tensile properties of steel material due to the surface defects.

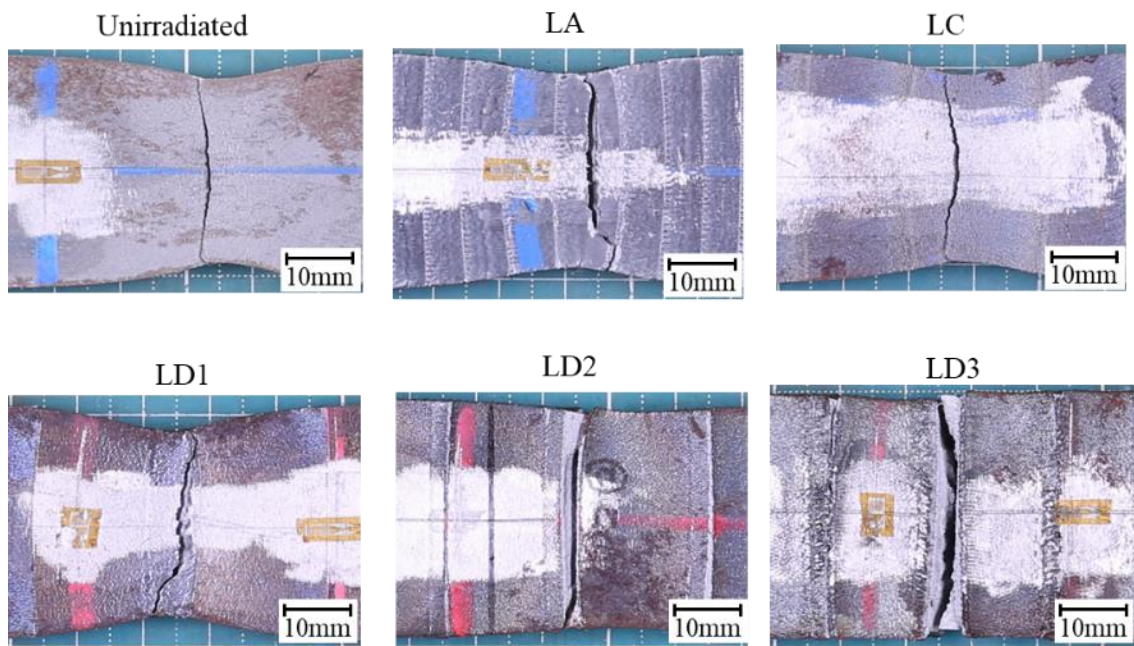


Figure 5-3 Fracture portions of specimens after tensile test.

The nominal stress-strain curves of specimens at room temperature are illustrated in Figure 5-4. It can be found in unirradiated and lower heat effects conditions, that the curves are similar to each other. Such as LC, LD1 and LD2 specimens, an ultimate tensile strength of appxomatly 400 MPa and similar elongation were presented in those specimens. However, tensile results of LA and LD3 specimens exhibited smaller elongation, and slight increase in the plastic stress-strain curve compared with the other specimens. Especially in LD3 speicmen, a sharp decrease in the elongation was presented. From the nominal stress-strain curve of the unirradiated specimens. The steel coupon deformed elastically until 0.11 % of the nominal strain in initial portion. From the stress-strain curve, the upper-yield and lower-yield point phenomena indicate a transition from elastic to plastic deformation. The deformation in the unirradiated steel coupon is distinctly inhomogeneous at this time, known as Lüders band. During this period the specimens are partially yielded, the Lüders band develops along with tensile process and

eventually covered the whole area. The Lüders band of unirradiated specimen starts at 0.11 % of strain from the gripped portion of the steel coupon where the stress is concentrated, and it covered gauge length at 2.00 % of the strain level. The total strain from upper-yield point to lower-yield point also known as Lüders strain. In case of unirradiated steel coupon, the Lüders strain is approximately 1.89 % in average. From the stress-strain curve of LC and LD1 specimens shown in Figure 5-4, similar tensile properties with unirradiated specimens are observed. Under LC condition, the upper-yield point appeared at 0.15 % of strain, and the lower-yield point was reached until 2.00 % of strain, showing a Lüders strain of 1.85 %, which is close to unirradiated specimens. Similar upper-yield point, lower-yield point and Lüders strain were presented in LD1 specimen as 0.15 %, 2.04 % and 1.89 % respectively. When the laser heat effects enhanced, as the stress-strain curve of LA, LD2 and LD3 specimens shown in Figure 5-4. The upper-yield point, lower-yield point and Lüders strain appeared 0.15 %, 1.50 % and 1.35 % in LA, 0.16 %, 1.69 %, 1.53 % in LD2 0.25 %, 1.63 %, 1.38 % in LD3 specimens. Smaller Lüders strain were observed in steel coupon treated by higher laser heat effects condition.

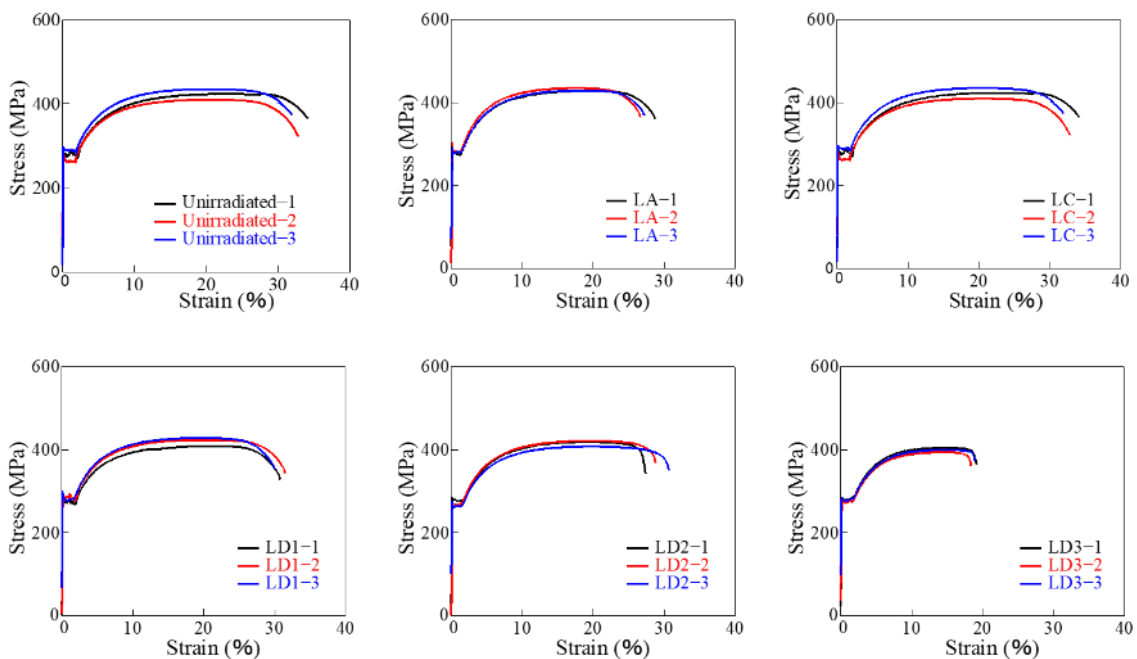


Figure 5-4 Nominal stress-strain curves of specimens.

The length of the Lüders strain mainly decided by the strain history and manufacturing method the of the tested steel materials and is not an intrinsic material property. The

chemical composition, microstructures, strain ageing and heat treatment are commonly considered to related to the Lüders strain [114]. In this study, chemical composition and strain ageing are the same for all the steel coupons as the same batch was used to manufacture the tensile test coupons. Thus, heat treatment and modified microstructures near laser-irradiated surface are the main reason responsible for decreasing Lüders strain. Besides, this difference in Lüders strain will change the cyclic and seismic performance of steel material to some extent [115].

The average yield strength, tensile strength, elongation, Young’s modulus and Poisson’s ratio of specimens extracted from tensile test are reported in Table 5-1. No obvious variation in most of the tensile properties can be observed in the results. The ultimate tensile strength were located around 400 to 430 MPa, and the yield strength were varying within 266 to 299 MPa. However, the elongation of the laser-treated steel coupons seems to decrease compares to the unirradiated specimens. The LD3 specimen even reach 19.3 elongation value which is the three fifths of unirradiated steel coupons.

Table 5-1 Average tensile test results and standard deviation

Specimens	Tensile strength (MPa)	Yield strength (MPa)	Young’s modulus (GPa)	Poisson’s ratio	Elongation (%)
Unirradiated	423 ± 10.3	289 ± 6.84	210 ± 6.01	0.285 ± 0.005	33.3 ± 3.71
LA	430 ± 2.01	282 ± 3.74	199 ± 8.18	0.262 ± 0.006	27.9 ± 1.12
LC	416 ± 1.41	266 ± 2.31	202 ± 3.60	0.268 ± 0.004	32.0 ± 1.49
LD1	424 ± 8.25	299 ± 5.51	206 ± 2.97	0.296 ± 0.010	31.6 ± 0.60
LD2	416 ± 5.86	277 ± 5.47	197 ± 4.02	0.291 ± 0.002	29.7 ± 1.10
LD3	400 ± 4.10	281 ± 2.54	197 ± 8.00	0.286 ± 0.003	19.3 ± 0.72

Average ± Standard deviation

To take various laser thermal effects into account, a simple indicator is demanded to express the total heat that steel coupons had absorbed during the laser irradiation. Considering the output power of laser conditions were fixed at a given value during the irradiation process, and the total irradiation time were also decided by the moving speed and direction of XY-axis motorized stage. Thus the amount of spend energy for each laser condition is a definite value. Although laser heat effects on the detail surface characteristics is still related to different power density, interaction time and overlapping effects, the depth of MZ&HAZ were deemed to a result of total laser thermal effects. And the changing microstructures, micro cracks and surface defects inside MZ&HAZ were primary causes of mechanical properties degradation. Thus the output energy during laser

treatment divided by irradiated area was defined as energy density, to represent a total laser thermal effects, as shown in Figure 5-5.

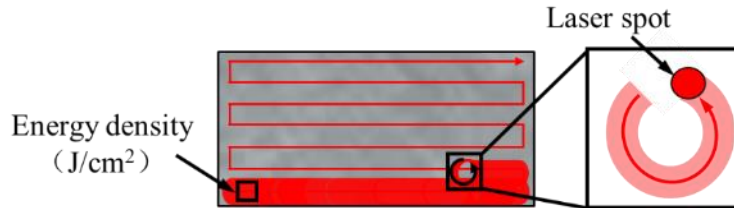


Figure 5-5 Schematic illustration of energy density result from laser irradiation.

Using the laser energy density as described in previous section, the tensile strength, yield strength and elongation were used to produce a graph with laser energy density as shown in Figure 5-6. From the plotted mechanical properties, the tensile strength and yield strength of steel coupons after laser irradiation remain steady state, while notable variation of mechanical property is the decrease in elongation. The elongation and laser energy density exhibit decline relationship, from 600 (LC) to 4615 (LD3) J/cm^2 . The result here manifest laser thermal effects does impact the mechanical properties of steel material, and higher energy density result in decreasing elongation. As described in the CHAPTER 3, the surface defects and modified microstructure near laser-irradiated surface were considered responsible for the decreasing elongation. The following study on fractography of tensile tested specimens will give further explanation of the relationship between laser thermal effects and the mechanical properties changing.

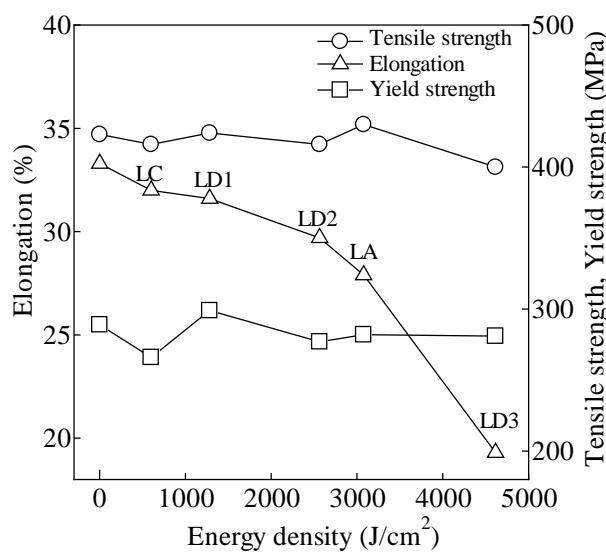


Figure 5-6 Relationship between laser energy density and mechanical properties.

5.4 Fractography and fracture mechanism of specimens

The macroscale fracture morphologies of specimens are shown in Figure 5-7. It can be seen the fracture morphology changes significantly under laser conditions with higher thermal effects. For unirradiated specimen, a typical cup-and-cone fracture surface is presented, indicating ductile failure [116]. The same macroscale fracture morphology is found in LC specimen, demonstrated lower laser energy (600 J/cm^2 in this case), and the consequence of shallow MZ&HAZ depth had limited impact on the fracture mechanism of steel coupons. However, the macroscale fracture pattern of LA, LD1 and LD2 conditions showing slant fractures instead of cup-and-cone feature. Although this kind of fracture morphology still represents ductile failure, meanwhile, it indicates the fracture mechanism of these specimens might be changed by laser thermal effects. Also, the fracture patterns in the edge of LA, LD1 and LD2 specimens are worth noting that both LA and LD1 specimens presenting the shear lip, while the LD2 specimen presenting flat plateau in the edge. Usually the shear lips indicating a typical internal ductile fracture initiation, and the flat plateau might suggest that LD2 specimen undergoing an opposite fracture progress. On the other hand, the fracture of LD3 specimen revealed brittle morphology of square features instead of ductile type fracture morphologies. Noticing that the fracture position on steel surface were located on the top/bottom portion of both laser-treated side. It is considered that the surface defects and microstructure changing in the intense laser overlapping effects area of top/bottom portion could be harmful to the fracture mechanism of steel material. The distinct defects may causing stress concentration, and changing hardness of microstructure may also contribute to the uneven distribution of stress transmission.

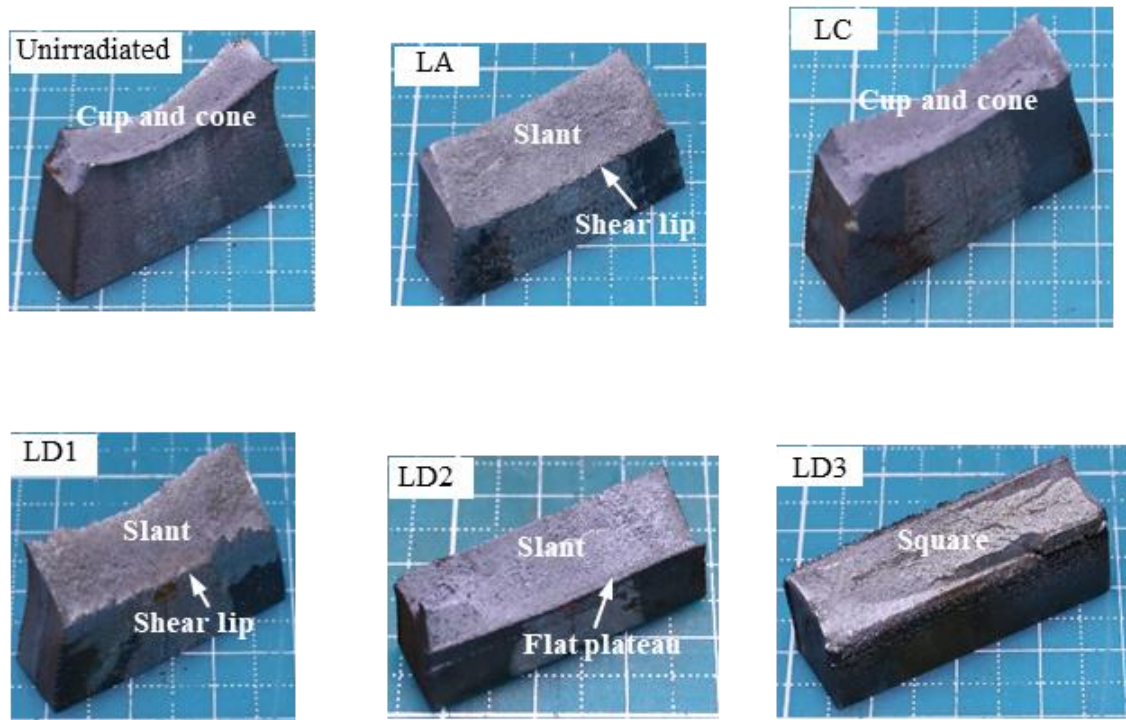


Figure 5-7 Fracture surface of specimens.

The SEM fractographs showed in Figure 5-8 exhibit microscale fracture morphologies of specimens. Two observation spots within fracture surface were adopted in this study, in which central portion labeled as Center and edge portion near laser-irradiated surface labeled as Edge in the figures. Typical rough surface with fairly equiaxed dimples is observed in central portion for unirradiated specimens, with elongated dimples were presented at the edge of all inspected samples, indicating internal ductile fracture initiation [117]. Similar microscale fracture can be observed in LA, LC and LD1 specimens, manifesting lower laser thermal effects have limited influence on the fracture mechanism of steel coupons. It can be found in microfractography that similar small and deep dimples were presented in the unirradiated, lower thermal effects of LC and LD1 specimens, while the LA specimen presented large and shallow dimples. On the edge of fracture surface, alike elongated dimple distributions are exhibit in unirradiated, LC and LD1 specimens, yet LA specimen present fewer elongated dimples with partial equiaxed dimples. To be specific, larger size and elongated dimples representative of better plasticity [118]. Changes of microfractography at the edge and center portion provided the visual evidence of relatively poor plasticity of laser-treated steel coupon when under higher laser thermal effects. From the above mentioned results, laser thermal

effects will not necessarily change the fracture mechanism of steel material, but the presence of heat affected layers will definitely influence the plasticity. The higher thermal effects were supposed to decrease the plasticity of laser-treated steel coupons.

From the microfractographies of LD2 specimen, elongated dimples were observed in the center portion, and deep equiaxed dimples were presented at the edge region. The distribution of equiaxed dimples and elongated dimples just the reverse of unirradiated, LA, LC and LD1 specimens. As a result, surface initiation of the fracture [117] is confirmed under LD2 laser condition. The shifting fracture initiation might be attributed to the presence of surface defects under LD2 condition as shown in Figure 2-9. Stress concentration take place in the cracks of top/bottom portion, and the laser-treated steel surface reached ultimate tensile strength at first, then the fracture propagate from the surface to center of cross-section. Resulting in equiaxed dimples on the edge, and elongated dimples in the center.

The microfractographies of LD3 specimen in the center portion showing a typical brittle characteristics of river patterns [119], while the edge portion is the similar morphologies as LD2 specimen. Indicating the fracture mechanism of LD3 specimen just like LD2 condition, surface initiation was take in place under this laser condition. Compares to LD2, the LD3 specimen possessed distinctly deeper MZ in Region B as shown in Figure 2-9. The depth of MZ in LD3 is 1200 μm deep with a keyhole shape. From the hardness presented in Figure 3-14, relatively lower hardness were observed in the MZ region, and the surrounding hardness in Region A presenting higher hardness values. Noticing that ultimate tensile strength is directly proportional to the hardness value, thus the Region B is weaker than Region A in the heat affected layers. Combined with the surface defects remained in the bulges of LD3, the stress concentration level was significantly improved inside the keyhole MZ area. As a result, the fracture initiate at the Region B surface, and develop rapidly from the surface to the inner, eventually a brittle fracture occurred in the LD3 specimen. The brittle fracture mechanism also decreased elongation of the LD3 specimen.

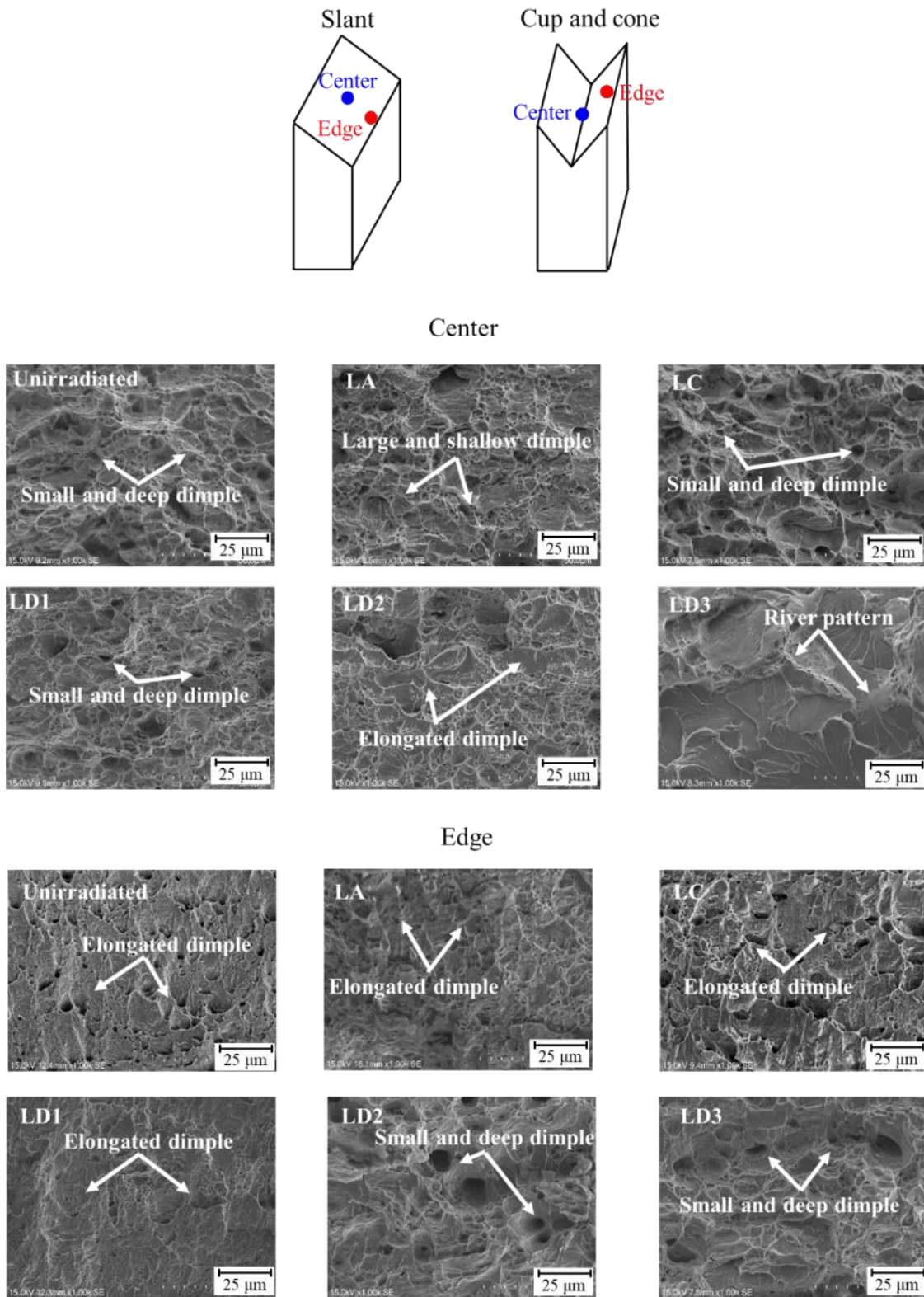


Figure 5-8 SEM observation position and fractographs of specimens.

The SEM fractographs illustrates the main fracture mechanism for tested specimens is the coalescence of micro-voids [120], despite surface treatment method. However, the fracture mechanism of steel coupons with higher laser thermal effects were different from unirradiated and lower thermal effect conditions. As for the cup and cone fracture features exhibited in unirradiated and LC specimens, larger quantities of small and deep dimples were observed in the central portion of fracture surface, The small and deep dimples were the results of low stress triaxiality induced by distinct necking effects. The radial component stress of specimen is very small due to low stress triaxiality, therefore, most of the micro-voids are developed along loading direction, then become small and deep dimples [120]. Consequently, a cavity appeared at the center of necking portion and the final cup-and-cone fracture occurred [116], as the illustrative sketch of fracture mechanism shown in Figure 5-9 (a). When it comes to slant fracture of LA, LD1 and LD2, large and shallow (approximate 20 μm in width) dimple features are the main fracture morphologies. The stress triaxiality of these specimen were relatively higher than the other specimens because of the presence of deeper MZ&HAZ. The micro-voids suffered larger radial component stress at the high stress triaxiality, which accelerates voids in the shear band growth along the radial direction and coalescence with adjacent each other. Finally, the ductile failure with large and shallow dimples on the slant fracture surface was appeared at LA, LD1 and LD2 specimens, as shown in Figure 5-9 (b). Moreover, the fracture strain decreased with increasing stress triaxiality, causing smaller elongation of these specimens exhibited in Figure 5-6.

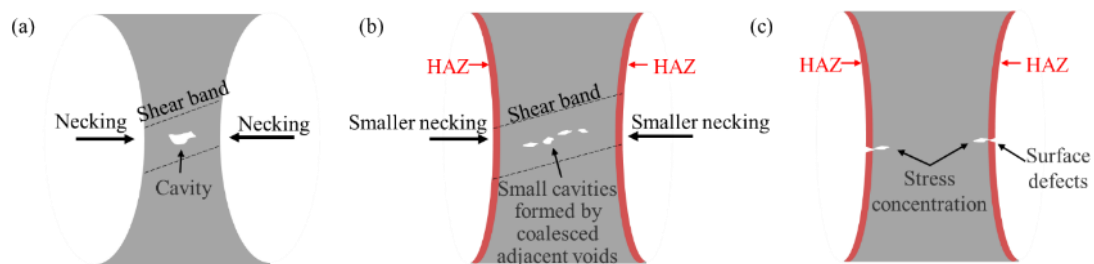


Figure 5-9 Illustrative sketches of fracture mechanism from thickness direction.

When the laser overlapping effects increased to a certain extent, as the tensile results shown in LD3 specimens, the fracture mechanism of the steel coupons were dominated by the surface defects and modified microstructures. Fracture initiate on surface due to outstanding surface defects, combining with the microstructure modification, the stress

concentration phenomena improved and leading to a rapid fracture develop, consequently, brittle failure occurred as shown in Figure 5-9 (c). The significant decreasing in elongation also attributed to the brittle fracture.

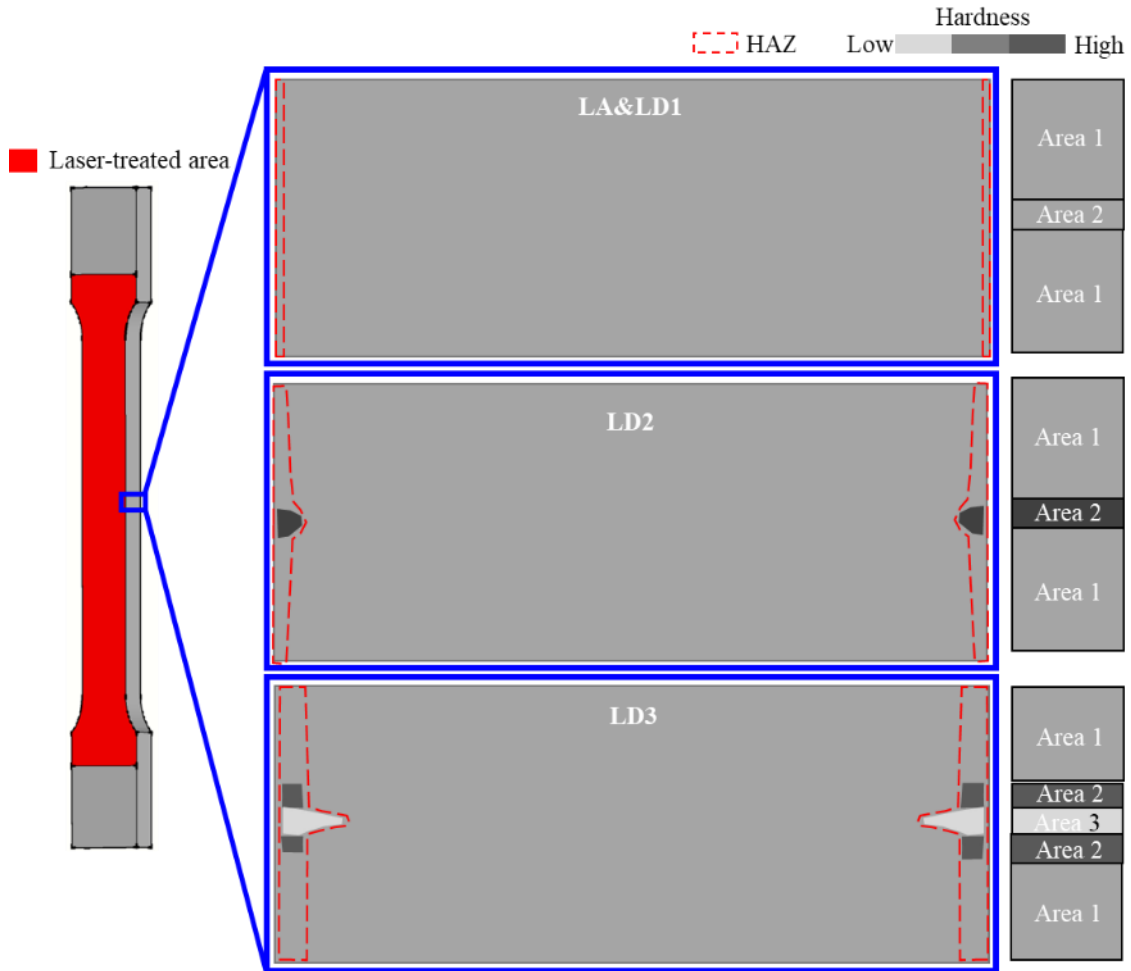


Figure 5-10 Schematic illustration of hardness and MZ&HAZ on cross-section of laser-treated tensile specimens.

To further discuss the laser thermal effects on the mechanical properties, the depth and distribution of MZ&HAZ with the hardness were presented in Figure 5-10. The influence of modified microstructure on the mechanical properties basically relied on the hardness changing, as the hardness is directly related to ultimate tensile strength and yield strength [73]. The first consideration is the thickness of MZ&HAZ. To evaluate thickness of hardness changing layer, the Rule of Mixture (ROM) [121] is a simple and reliable method for quantitative analysis of the ultimate tensile strength or yield strength of a gradient mixed material. Basing on the ROM, the overall strength can be regarded as the

summation of the strength of MZ&HAZ and base metal layers:

$$\sigma_{ROM} = V_{MZ\&HAZ}\sigma_{MZ\&HAZ} + (1 - V_{MZ\&HAZ})\sigma_{base} \quad (5-1)$$

where the σ_{ROM} is the integrated strength calculated by ROM, $V_{MZ\&HAZ}$ is the volume fraction of the MZ&HAZ layer, $\sigma_{MZ\&HAZ}$ is the strength of MZ&HAZ layer, σ_{base} is the strength of base metal.

Assuming the MZ&HAZ depth in Region A and Region B are constant, the average depth can be used as substitute. Then the volume fraction of the HZ&HAZ layer is the percentage of thickness. On the other hand, the ultimate tensile strength or yield strength can be obtained from the hardness testing basing on the relational equations [73]. Noticed that Region A and Region B had different heat affected layer depth, and the hardness in these regions either rising or decrease, depending on the overlapping effects. Thus both calculation for these two regions should be made in case of predict the strength after laser irradiation, weaker region decide the final integrated strength. However, the depth of MZ&HAZ is rather shallow compares to the thickness of tensile test coupons according to Figure 3-14. The volume fraction of the major laser conditions only presented a value lower than 1/12. And the improving on hardness still no large enough to bring noteworthy strength variation.

In this case, the effects of changing microstructures for a thicker steel plate (12 mm in this study) is combining to the surface defects and hardness distribution, overall effects of these factors causing stress concentration on the steel surface. From the distribution of hardness in Figure 5-10, the LA and LD1 conditions generate an ignorable MZ&HAZ depth compares to the steel thickness, thus a steady state mechanical properties is presented after tensile test, except for the elongation as discussed in previous sections. When the outstanding MZ&HAZ layer is formed in the Region B, the adjacent material remain lower hardness values as shown in the LD2 specimen. Thus the stress concentration between Area 1 and Area 2, together with surface defects in Region B induce the fracture initiate on surface. In the LD3 specimen, the hardness near MZ in Region B is significantly higher than the hardness in Region B as shown in Figure 5-10. Thus the stress concentration is more severe in this laser condition, leading to a brittle

fracture mechanism instead of ductile fracture. It should be noticed that for a thinner steel coupons, the volume fraction of MZ&HAZ after laser irradiation is an innegligible issue, the ultimate tensile strength and yield strength are supposed to improve according to the ROM.

5.5 Summary

To investigate the heat effects of laser irradiation on mechanical properties of carbon steel, tensile test and fractography were adopted. Compared to the surface and cross-section inspections in CHAPTER 3, the results are summarized as follows:

- (1) Tensile test results indicated that laser surface treatment has no distinct effects on most of the mechanical properties, except for decreasing elongation in higher laser thermal effect condition. Laser energy density could be a preferable parameter to represent overall laser thermal effects. The decreasing elongation showed negative correlation to the laser energy density.
- (2) Fractography of specimens indicated the laser-treated steel coupons undergo ductile failure under lower laser thermal effects. In which the fracture mechanism of LA, LD1 and LD2 specimens changed due to deeper HAZ formed on the surface, and finally results in decreasing elongation. In higher laser thermal effects of LD3, the fracture mechanism of steel coupon presented brittle characteristics according to the SEM microfractography.
- (3) Surface defects, micro cracks and hardness distribution after laser irradiation are the main reason for decreasing elongation. Stress concentration take place due to distinct surface defects and MZ&HAZ depth, resulting in final brittle fracture.

CHAPTER 6 CONCLUSIONS AND FUTURE WORK

6.1 Main conclusions and innovations

- (1) A new surface treatment technique for corroded steel structures using rotating CW laser was present in this work, the potential degradations in steel material performance due to laser thermal effects were established.
- (2) A modified peak temperature calculation method for rotating laser surface treatment was proposed, parameter optimization for laser irradiation can proceed before surface treatment.
- (3) Higher laser thermal effects result in steel surface with rough features and defects. Oxide layer formed on the laser-treated steel surface, content and integrity improved with laser output power. However, the oxide layer should be removed before coating to maintain quality. Refined microstructure was presented near the surface after laser treatment, higher laser overlapping effects contributed to deeper modified microstructure.
- (4) The electrochemical properties and mechanical properties of carbon steel affected by the surface properties and microstructures after laser treatment. Oxide layer contributed to improved corrosion resistance, yet surface defects would damage the protective efficiency of laser-affected layer. Surface defects and modified microstructure will induce stress concentration, and reduce the elongation of carbon steel.
- (5) To ensure complete treatment and avoid damage in the steel performance, proper laser processing parameters were suggested basing on peak temperature calculation, laser-treated surface properties and mechanical properties.

6.2 Summary

In this dissertation, a newly developed high-power CW laser equipment for surface treatment of corroded steel structures was adopted, the thermal effects result from laser beam were discussed in aspects of temperature field, surface properties, microstructure, electrochemical properties and mechanical properties of laser-treated steel material.

6.2.1 Peak temperature distribution in carbon steel during laser irradiation

A modified peak temperature calculation method was proposed to analyze the thermal effects of given laser conditions, the accuracy of the calculation method was verified using experimental result. Results showed that the modified calculation method described peak temperature distribution in good agreement with the experimental results. Higher laser overlapping effects definitely increasing the laser thermal effects, significantly lifted peak temperature in severe overlapping region induced surface defects on the irradiated steel surface. The modified calculation method was expected to provide a method for parameter optimization, in order to avoid severe laser thermal effects, and guarantee desirable laser ablation effects at the same time.

6.2.2 Surface properties and microstructure affected by laser irradiation

From the surface morphologies and roughness, higher laser power density and longer interaction time increased the laser thermal effects, thereby more irregular surfaces were obtained, yet the laser overlapping effects contributed to much more severe thermal effects that result in surface defects. With increasing laser thermal effects, higher state iron oxide and content were presented on the laser-treated steel surface. Meantime, the deepness of modified microstructures was increased with improving thermal effects, gradient distribution was observed in the cross-section of laser-treated steel plates. The application test indicated proper laser beam overlapping rate is higher than 0%, to ensure complete surface treatment. And the depth of corrosion pits has no obvious effects on the laser ablation effects, but narrow width of corrosion pit may trap fume inside and shelter the laser beam that reduce laser ablation effects as consequence.

6.2.3 The presence of oxide layer resulted from different laser conditions

Electrochemical test results indicating an improving corrosion resistance after laser irradiation, which is mainly attributed to the oxide layer formed on the surface. Although increasing laser thermal effects will bring more iron oxide formation, yet the resulted surface defects damage the corrosion properties. However, the integrated iron oxide can only provide temperate protection, pitting corrosion and re-coating quality are disadvantages under the presence of oxide layer. Thus, following procedure is expected after laser irradiation to remove the iron oxide.

6.2.4 Degradation of tensile properties in carbon steel after laser irradiation

Results from tensile test indicated that laser surface treatment had obvious effects in decreasing elongation of steel material under higher laser thermal effect condition. Fractography of specimens indicated the laser-treated steel coupons undergo ductile failure in lower laser thermal effects, and brittle failure was identified under higher laser thermal effects. Surface defects, micro cracks and hardness distribution after laser irradiation are the main reason for decreasing elongation. Stress concentration take place due to distinct surface defects.

6.2.5 Proper laser processing parameters

The laser processing parameters mainly contain two parts, those been set before the laser equipment assembled, and the laser ring moving speed (i.e. movement of handhold operation). The first step of parameter determination should adopt the modified peak temperature calculation method, to prevent deep MZ&HAZ formation in Region A and Region B, also ensure the temperature should higher than boiling point of the targeting material in order to obtain laser ablation effects. For the recommended depth of MZ&HAZ, the difference between Region A and Region B should lower than a factor of 2 according to Chapters 2, 3 and 5. For recommendation of laser ring moving speed, according to surface morphologies, electrochemical properties and tensile test result, the laser ring moving speed should ensure comprehensive treatment, which is higher than 0% laser beam overlapping rate, while the overlapping rate should lower than 75% to avoid degradation in corrosion resistance and tensile property.

6.3 Recommendations for future work

This dissertation had evaluated the laser thermal effects and suggested proper laser processing parameters for field usage. However, limitations existed in the work which worthy for future work:

- (1) This work adopted bare steel plates for the evaluation, lacking consideration in the presence of rust layer. The thermal effects on base metal may take place before removing the rust layer through heat conduction. Future work should prepare corroded steel plate for laser irradiation, to evaluate the actual laser thermal effects for corroded steel members. However, the preparation for identical uniform

corrosion could be a challenge to realize.

- (2) The effects of oxide layer on following coating quality, as well as approach for the iron oxide removal should be discussed in future research. Furthermore, other metallic materials such as weathering steel, stainless steel and aluminium alloy should be considered for CW laser treatment to expand the application of this technique. In addition, atmospheric exposure and accelerated corrosion test may be conducted for the laser-treated metallic material to evaluate the corrosion properties, due to possible improving corrosion resistance for weathering steel or aluminium alloy after laser irradiation.
- (3) The same thickness of specimens is used in this study, lacking consideration of relationship between plate thickness and laser thermal effects. In future study, the effect of plate thickness on the mechanical properties of laser-treated steel members should be investigated.
- (4) Although the degradation in elongation and corrosion resistance of carbon steel treated by higher laser thermal effects is discussed, this study only provide a parameter optimization method to avoid surface defects. Other method like repeat irradiation at intervals should be investigated for acquiring more clear surface condition under lower thermal effects.

REFERENCES

- [1] S. Guo, R. Si, Q. Dai, Z. You, Y. Ma, J. Wang, A critical review of corrosion development and rust removal techniques on the structural/environmental performance of corroded steel bridges, *J. Clean. Prod.* 233 (2019) 126–146. doi:10.1016/j.jclepro.2019.06.023.
- [2] W. Funke, Blistering of paint films and filiform corrosion, *Prog. Org. Coatings*. 9 (1981) 29–46. doi:10.1016/0033-0655(81)80014-3.
- [3] S. Kainuma, M. Yang, S. Ishihara, A. Kaneko, T. Yamauchi, Corrosion protection of steel members using an Al-Zn base sacrificial anode and fiber sheet in an atmospheric environment, *Constr. Build. Mater.* (2019). doi:10.1016/j.conbuildmat.2019.07.067.
- [4] M. Yang, S. Kainuma, S. Ishihara, A. Kaneko, T. Yamauchi, Atmospheric corrosion protection method for corroded steel members using sacrificial anode of Al-based alloy, *Constr. Build. Mater.* (2020). doi:10.1016/j.conbuildmat.2019.117405.
- [5] M. Morcillo, I. Díaz, H. Cano, B. Chico, D. de la Fuente, Atmospheric corrosion of weathering steels. Overview for engineers. Part II: Testing, inspection, maintenance, *Constr. Build. Mater.* 222 (2019) 750–765. doi:10.1016/j.conbuildmat.2019.06.155.
- [6] S. Kainuma, Y. Yamamoto, J.H. Ahn, Y.S. Jeong, Evaluation method for time-dependent corrosion depth of uncoated weathering steel using thickness of corrosion product layer, *Struct. Eng. Mech.* 65 (2018) 191–201. doi:10.12989/sem.2018.65.2.191.
- [7] M.K.A.A. Razab, A. Mohamed Noor, M. Suhaimi Jaafar, N.H. Abdullah, F.M. Suhaimi, M. Mohamed, N. Adam, N.A. Auli Nik Yusuf, A review of incorporating Nd:YAG laser cleaning principal in automotive industry, *J. Radiat. Res. Appl. Sci.* 11 (2018) 393–402. doi:10.1016/j.jrras.2018.08.002.
- [8] A. Ramil, J.S. Pozo-Antonio, M.P. Fiorucci, A.J. López, T. Rivas, Detection of the optimal laser fluence ranges to clean graffiti on silicates, *Constr. Build. Mater.* (2017). doi:10.1016/j.conbuildmat.2017.05.035.
- [9] T. Palomar, M. Oujja, I. Llorente, B. Ramírez Barat, M. V. Cañamares, E. Cano, M. Castillejo, Evaluation of laser cleaning for the restoration of tarnished silver

- artifacts, *Appl. Surf. Sci.* (2016). doi:10.1016/j.apsusc.2016.06.017.
- [10] J. Min, H. Wan, B.E. Carlson, J. Lin, C. Sun, Application of laser ablation in adhesive bonding of metallic materials: A review, *Opt. Laser Technol.* (2020). doi:10.1016/j.optlastec.2020.106188.
- [11] M. Schmidt, M. Merklein, D. Bourell, D. Dimitrov, T. Hausotte, K. Wegener, L. Overmeyer, F. Vollertsen, G.N. Levy, Laser based additive manufacturing in industry and academia, *CIRP Ann.* (2017). doi:10.1016/j.cirp.2017.05.011.
- [12] K.M. Hong, Y.C. Shin, Prospects of laser welding technology in the automotive industry: A review, *J. Mater. Process. Technol.* (2017). doi:10.1016/j.jmatprotec.2017.02.008.
- [13] S. Milles, M. Soldera, T. Kuntze, A.F. Lasagni, Characterization of self-cleaning properties on superhydrophobic aluminum surfaces fabricated by direct laser writing and direct laser interference patterning, *Appl. Surf. Sci.* (2020) 146518. doi:10.1016/j.apsusc.2020.146518.
- [14] G. Giannuzzi, C. Gaudio, R. Di Mundo, L. Mirengi, F. Fraggelakis, R. Kling, P.M. Lugarà, A. Ancona, Short and long term surface chemistry and wetting behaviour of stainless steel with 1D and 2D periodic structures induced by bursts of femtosecond laser pulses, *Appl. Surf. Sci.* (2019). doi:10.1016/j.apsusc.2019.07.126.
- [15] S.S. Singh, P.K. Baruah, A. Khare, S.N. Joshi, Effect of laser beam conditioning on fabrication of clean micro-channel on stainless steel 316L using second harmonic of Q-switched Nd:YAG laser, *Opt. Laser Technol.* (2018). doi:10.1016/j.optlastec.2017.08.020.
- [16] R. Solmaz, Investigation of adsorption and corrosion inhibition of mild steel in hydrochloric acid solution by 5-(4-Dimethylaminobenzylidene)rhodanine, *Corros. Sci.* 79 (2014) 169–176. doi:10.1016/j.corsci.2013.11.001.
- [17] P. Bothi Raja, M.G. Sethuraman, Inhibitive effect of black pepper extract on the sulphuric acid corrosion of mild steel, *Mater. Lett.* 62 (2008) 2977–2979. doi:10.1016/j.matlet.2008.01.087.
- [18] O.O. Joseph, S. Sivaprasad, O.S.I. Fayomi, Comparative study on the effect of NaNO₂ in corrosion inhibition of micro-alloyed and API-5L X65 steels in E20

- simulated FGE, in: *Energy Procedia*, Elsevier Ltd, 2017: pp. 953–960. doi:10.1016/j.egypro.2017.07.128.
- [19] S. Raffo, I. Vassura, C. Chiavari, C. Martini, M.C. Bignozzi, F. Passarini, E. Bernardi, Weathering steel as a potential source for metal contamination: Metal dissolution during 3-year of field exposure in a urban coastal site, *Environ. Pollut.* 213 (2016) 571–584. doi:10.1016/j.envpol.2016.03.001.
- [20] H.A. Mohamed, Eco-friendly zero VOC anticorrosive paints for steel protection, *J. Appl. Polym. Sci.* 125 (2012) 1790–1795. doi:10.1002/app.36256.
- [21] T.C. Miller, M.J. Chajes, D.R. Mertz, J.N. Hastings, Strengthening of a Steel Bridge Girder Using CFRP Plates, *J. Bridg. Eng.* 6 (2001) 514–522. doi:10.1061/(ASCE)1084-0702(2001)6:6(514).
- [22] S. Geng, J. Sun, L. Guo, Effect of sandblasting and subsequent acid pickling and passivation on the microstructure and corrosion behavior of 316L stainless steel, *Mater. Des.* 88 (2015) 1–7. doi:10.1016/j.matdes.2015.08.113.
- [23] K. Kambham, S. Sangameswaran, S.R. Datar, B. Kura, Copper slag: optimization of productivity and consumption for cleaner production in dry abrasive blasting, *J. Clean. Prod.* 15 (2007) 465–473. doi:10.1016/j.jclepro.2005.11.024.
- [24] L. Li, Chloride corrosion threshold of reinforcing steel in alkaline solutions - Open-circuit immersion tests, *Corrosion.* 57 (2001) 19–28. doi:10.5006/1.3290325.
- [25] P. Ortiz, V. Antúnez, R. Ortiz, J.M. Martín, M.A. Gómez, A.R. Hortal, B. Martínez-Haya, Comparative study of pulsed laser cleaning applied to weathered marble surfaces, *Appl. Surf. Sci.* 283 (2013) 193–201. doi:10.1016/j.apsusc.2013.06.081.
- [26] S. Pratheesh Kumar, S. Elangovan, R. Mohanraj, V. Sathya Narayanan, Significance of continuous wave and pulsed wave laser in direct metal deposition, *Mater. Today Proc.* (2021). doi:10.1016/j.matpr.2021.03.041.
- [27] N. Maharjan, W. Zhou, Y. Zhou, Y. Guan, N. Wu, Comparative study of laser surface hardening of 50CrMo4 steel using continuous-wave laser and pulsed lasers with ms, ns, ps and fs pulse duration, *Surf. Coatings Technol.* 366 (2019) 311–320. doi:10.1016/j.surfcoat.2019.03.036.
- [28] D. Bäuerle, Laser processing and chemistry: Recent developments, in: *Appl. Surf. Sci.*, 2002: pp. 1–6. doi:10.1016/S0169-4332(01)00655-9.

- [29] A. Kumar, R.B. Bhatt, P.G. Behere, M. Afzal, A. Kumar, J.P. Nilaya, D.J. Biswas, Laser-assisted surface cleaning of metallic components, in: *Pramana - J. Phys.*, Indian Academy of Sciences, 2014: pp. 237–242. doi:10.1007/s12043-013-0665-6.
- [30] X. Li, T. Huang, A.W. Chong, R. Zhou, Y.S. Choo, M. Hong, Laser cleaning of steel structure surface for paint removal and repaint adhesion, *Oejournal.Org.* 44 (2017). doi:10.3969/j.issn.1003-501X.2017.03.009.
- [31] C. Zhou, H. Li, G. Chen, G. Wang, Z. Shan, Effect of single pulsed picosecond and 100 nanosecond laser cleaning on surface morphology and welding quality of aluminium alloy, *Opt. Laser Technol.* (2020). doi:10.1016/j.optlastec.2020.106197.
- [32] G. Zhang, X. Hua, Y. Huang, Y. Zhang, F. Li, C. Shen, J. Cheng, Investigation on mechanism of oxide removal and plasma behavior during laser cleaning on aluminum alloy, *Appl. Surf. Sci.* (2020). doi:10.1016/j.apsusc.2019.144666.
- [33] S. Liu, Y.C. Shin, Additive manufacturing of Ti6Al4V alloy: A review, *Mater. Des.* (2019). doi:10.1016/j.matdes.2018.107552.
- [34] F. Liu, C. Tan, X. Gong, L. Wu, B. Chen, X. Song, J. Feng, A comparative study on microstructure and mechanical properties of HG785D steel joint produced by hybrid laser-MAG welding and laser welding, *Opt. Laser Technol.* 128 (2020) 106247. doi:10.1016/j.optlastec.2020.106247.
- [35] V. Errico, S.L. Campanelli, A. Angelastro, M. Mazzarisi, G. Casalino, On the feasibility of AISI 304 stainless steel laser welding with metal powder, *J. Manuf. Process.* 56 (2020) 96–105. doi:10.1016/j.jmapro.2020.04.065.
- [36] S. Huang, D. Ma, J. Sheng, E. Agyenim-Boateng, J. Zhao, J. Zhou, Effects of laser peening on tensile properties and martensitic transformation of AISI 316L stainless steel in a hydrogen-rich environment, *Mater. Sci. Eng. A.* 788 (2020) 139543. doi:10.1016/j.msea.2020.139543.
- [37] Y. Wang, J. Shi, Recrystallization behavior and tensile properties of laser metal deposited Inconel 718 upon in-situ ultrasonic impact peening and heat treatment, *Mater. Sci. Eng. A.* (2020). doi:10.1016/j.msea.2020.139434.
- [38] Y. Shi, X. Yang, D. Yang, D. Shi, G. Miao, Z. Wang, Evaluation of the influence of surface crack-like defects on fatigue life for a P/M nickel-based superalloy FGH96, *Int. J. Fatigue.* 137 (2020) 105639. doi:10.1016/j.ijfatigue.2020.105639.

-
- [39] J. Gao, C. Wu, Y. Hao, X. Xu, L. Guo, Numerical simulation and experimental investigation on three-dimensional modelling of single-track geometry and temperature evolution by laser cladding, *Opt. Laser Technol.* 129 (2020) 106287. doi:10.1016/j.optlastec.2020.106287.
- [40] F. Lambiase, S. Genna, Homogenization of temperature distribution at metal-polymer interface during Laser Direct Joining, *Opt. Laser Technol.* 128 (2020) 106226. doi:10.1016/j.optlastec.2020.106226.
- [41] Q. Nguyen, A. Azadkhou, M. Akbari, A. Panjehpour, A. Karimipour, Experimental investigation of temperature field and fusion zone microstructure in dissimilar pulsed laser welding of austenitic stainless steel and copper, *J. Manuf. Process.* (2020). doi:10.1016/j.jmapro.2020.03.037.
- [42] M.F. Ashby, K.E. Easterling, Transformation Hardening of Steel Surfaces By Laser Beams., Cambridge Univ. Eng. Dep. (Technical Report) CUED/C-MATS. 32 (1984) 1935–1948.
- [43] A. Bendoumi, N. Makuch, R. Chegroune, M. Kulka, M. Keddou, P. Dziarski, D. Przystacki, The effect of temperature distribution and cooling rate on microstructure and microhardness of laser re-melted and laser-borided carbon steels with various carbon concentrations, *Surf. Coatings Technol.* (2020). doi:10.1016/j.surfcoat.2020.125541.
- [44] L. Zhang, G. Yu, S. Li, X. He, X. Xie, C. Xia, W. Ning, C. Zheng, The effect of laser surface melting on grain refinement of phase separated Cu-Cr alloy, *Opt. Laser Technol.* (2019). doi:10.1016/j.optlastec.2019.105577.
- [45] P. Wei, Z. Wei, Z. Chen, J. Du, Y. He, J. Li, Y. Zhou, The AlSi10Mg samples produced by selective laser melting: single track, densification, microstructure and mechanical behavior, *Appl. Surf. Sci.* (2017). doi:10.1016/j.apsusc.2017.02.215.
- [46] R. Mathew, P.R. Stoddart, D. Nolan, Y. Durandet, Microstructural refinement of aluminium-zinc-silicon coated steels, *Surf. Coatings Technol.* (2016). doi:10.1016/j.surfcoat.2016.01.024.
- [47] Q. Lin, Z.J. Fan, W. Wang, Z. Yan, Q. Zheng, X. Mei, The effect of spot overlap ratio on femtosecond laser planarization processing of SiC ceramics, *Opt. Laser Technol.* (2020). doi:10.1016/j.optlastec.2020.106270.

-
- [48] P. Haglund, J. Frostevarg, J. Powell, I. Eriksson, A.F.H. Kaplan, Holographic measurement of distortion during laser melting: Additive distortion from overlapping pulses, *Opt. Laser Technol.* (2018). doi:10.1016/j.optlastec.2017.09.053.
- [49] F. Giudice, A. Sili, Weld metal microstructure prediction in laser beam welding of austenitic stainless steel, *Appl. Sci.* 11 (2021) 1–14. doi:10.3390/app11041463.
- [50] F. Giudice, S. Missori, A. Sili, Parameterized multipoint-line analytical modeling of a mobile heat source for thermal field prediction in laser beam welding, *Int. J. Adv. Manuf. Technol.* 112 (2021) 1339–1358. doi:10.1007/s00170-020-06479-0.
- [51] M. Paczkowska, N. Makuch, M. Kulka, The influence of various cooling rates during laser alloying on nodular iron surface layer, *Opt. Laser Technol.* (2018). doi:10.1016/j.optlastec.2017.12.027.
- [52] M. Brandt, *Laser additive manufacturing: Materials, design, technologies, and applications*, 2016.
- [53] H. Mustafa, M. Mezera, D.T.A. Matthews, G.R.B.E. Römer, Effect of surface roughness on the ultrashort pulsed laser ablation fluence threshold of zinc and steel, *Appl. Surf. Sci.* 488 (2019) 10–21. doi:10.1016/j.apsusc.2019.05.066.
- [54] C. Chen, H.L. Tsai, Fundamental study of the bulge structure generated in laser polishing process, *Opt. Lasers Eng.* (2018). doi:10.1016/j.optlaseng.2018.03.006.
- [55] A. Temmler, N. Pirch, Investigation on the mechanism of surface structure formation during laser remelting with modulated laser power on tool steel H11, *Appl. Surf. Sci.* 526 (2020) 146393. doi:10.1016/j.apsusc.2020.146393.
- [56] D. Gandy, *Carbon Steel Handbook*, Carbon N. Y. 3 (2007) 172. doi:10.1016/j.apsusc.2007.05.066.
- [57] M. Shamsujjoha, S.R. Agnew, M.A. Melia, J.R. Brooks, T.J. Tyler, J.M. Fitz-Gerald, Effects of laser ablation coating removal (LACR) on a steel substrate: Part 1: Surface profile, microstructure, hardness, and adhesion, *Surf. Coatings Technol.* 281 (2015) 193–205. doi:10.1016/j.surfcoat.2015.01.071.
- [58] S. Hashmi, G.F. Batalha, C.J. Van Tyne, B. Yilbas, eds., *Comprehensive Materials Processing*, 1st ed., Elsevier, 2014. doi:10.1016/c2009-1-63473-0.
- [59] S.L. Engel, Basic of Laser Heat Treating, in: E. Metzbower (Ed.), *Source B. Appl. Laser Metalwork.*, American Society for Metals, 1981: pp. 149–171.

- [60] G. Udaya Kumar, S. Suresh, C.S. Sujith Kumar, S. Back, B. Kang, H.J. Lee, A review on the role of laser textured surfaces on boiling heat transfer, *Appl. Therm. Eng.* 174 (2020) 115274. doi:10.1016/j.applthermaleng.2020.115274.
- [61] P. Zhang, Z. Jia, Z. Yu, H. Shi, S. Li, D. Wu, H. Yan, X. Ye, J. Chen, F. Wang, Y. Tian, A review on the effect of laser pulse shaping on the microstructure and hot cracking behavior in the welding of alloys, *Opt. Laser Technol.* 140 (2021) 107094. doi:10.1016/j.optlastec.2021.107094.
- [62] J. Metelkova, Y. Kinds, K. Kempen, C. de Formanoir, A. Witvrouw, B. Van Hooreweder, On the influence of laser defocusing in Selective Laser Melting of 316L, *Addit. Manuf.* (2018). doi:10.1016/j.addma.2018.08.006.
- [63] W. Gao, S. Zhao, F. Liu, Y. Wang, C. Zhou, X. Lin, Effect of defocus manner on laser cladding of Fe-based alloy powder, *Surf. Coatings Technol.* 248 (2014) 54–62. doi:10.1016/j.surfcoat.2014.03.019.
- [64] B. Das, M. Gopinath, A.K. Nath, P.P. Bandyopadhyay, Effect of cooling rate on residual stress and mechanical properties of laser remelted ceramic coating, *J. Eur. Ceram. Soc.* 38 (2018) 3932–3944. doi:10.1016/j.jeurceramsoc.2018.04.020.
- [65] Q. Wang, Z. Zhang, X. Tong, S. Dong, Z. Cui, X. Wang, L. Ren, Effects of process parameters on the microstructure and mechanical properties of 24CrNiMo steel fabricated by selective laser melting, *Opt. Laser Technol.* 128 (2020) 106262. doi:10.1016/j.optlastec.2020.106262.
- [66] B. Mao, A. Siddaiah, Y. Liao, P.L. Menezes, Laser surface texturing and related techniques for enhancing tribological performance of engineering materials: A review, *J. Manuf. Process.* 53 (2020) 153–173. doi:10.1016/j.jmapro.2020.02.009.
- [67] S.G. Croll, Surface roughness profile and its effect on coating adhesion and corrosion protection: A review, *Prog. Org. Coatings.* 148 (2020) 105847. doi:10.1016/j.porgcoat.2020.105847.
- [68] I. Diaz, H. Cano, D. de la Fuente, B. Chico, J.M. Vega, M. Morcillo, Atmospheric corrosion of Ni-advanced weathering steels in marine atmospheres of moderate salinity, *Corros. Sci.* 76 (2013) 348–360. doi:10.1016/j.corsci.2013.06.053.
- [69] C.R. Hubbard, R.L. Snyder, RIR — Measurement and Use in Quantitative XRD, *Powder Diffr.* (1988). doi:10.1017/S0885715600013257.

- [70] R.M. Mahamood, E.T. Akinlabi, M. Shukla, S. Pityana, Scanning velocity influence on microstructure, microhardness and wear resistance performance of laser deposited Ti6Al4V/TiC composite, *Mater. Des.* (2013). doi:10.1016/j.matdes.2013.03.049.
- [71] X. Kang, S. Dong, P. Men, X. Liu, S. Yan, H. Wang, B. Xu, Microstructure evolution and gradient performance of 24CrNiMo steel prepared via laser melting deposition, *Mater. Sci. Eng. A.* (2020). doi:10.1016/j.msea.2020.139004.
- [72] Y. Zhou, S. Chen, X. Chen, T. Cui, J. Liang, C. Liu, The evolution of bainite and mechanical properties of direct laser deposition 12CrNi2 alloy steel at different laser power, *Mater. Sci. Eng. A.* (2019). doi:10.1016/j.msea.2018.10.092.
- [73] S. Naib, W. De Waele, P. Štefane, N. Gubeljak, S. Hertelé, Crack driving force prediction in heterogeneous welds using Vickers hardness maps and hardness transfer functions, *Eng. Fract. Mech.* 201 (2018) 322–335. doi:10.1016/j.engfracmech.2018.07.020.
- [74] K. Wang, A. Wei, Z. Shi, X. Chen, J. Lin, X. Tong, Z. Tao, X. Chen, The preparation and performance of grain size gradient TWIP steel fabricated by laser heat treatment, *Mater. Sci. Eng. A.* 743 (2019) 294–300. doi:10.1016/j.msea.2018.11.074.
- [75] W. Li, M. Vittoriotti, G. Jongbloed, J. Sietsma, The combined influence of grain size distribution and dislocation density on hardness of interstitial free steel, *J. Mater. Sci. Technol.* 45 (2020) 35–43. doi:10.1016/j.jmst.2019.11.025.
- [76] A. Ladewig, G. Schlick, M. Fisser, V. Schulze, U. Glatzel, Influence of the shielding gas flow on the removal of process by-products in the selective laser melting process, *Addit. Manuf.* 10 (2016) 1–9. doi:10.1016/j.addma.2016.01.004.
- [77] P.Y. Shcheglov, A. V. Gumenyuk, I.B. Gornushkin, M. Rethmeier, V.N. Petrovskiy, Vapor-plasma plume investigation during high-power fiber laser welding, *Laser Phys.* 23 (2013). doi:10.1088/1054-660X/23/1/016001.
- [78] C.Y. Barlow, Plume attenuation under high power Nd:yttrium aluminum garnet laser welding Sustainability cohort View project Integration of informal and formal sector in waste management in developing countries. View project, *Artic. J. Laser Appl.* 16 (2004) 9–15. doi:10.2351/1.1642636.
- [79] D. Bergström, The absorption of laser light by rough metal surfaces, Thesis. (2008)

- 226.
- [80] A. Hemmasian Etefagh, H. Wen, A. Chaichi, M.I. Islam, F. Lu, M. Gartia, S. Guo, Laser surface modifications of Fe-14Cr ferritic alloy for improved corrosion performance, *Surf. Coatings Technol.* 381 (2020) 125194. doi:10.1016/j.surfcoat.2019.125194.
- [81] Y.X. Liu, W. Guo, L. Li, H. Liu, S.L. Zhang, F.D. Zhang, Y.M. Cheng, Z. Liu, C. Suebka, Corrosion behaviour of laser-cleaned AA7024 aluminium alloy, *Appl. Surf. Sci.* 435 (2017) 452–461. doi:10.1016/j.apsusc.2017.11.141.
- [82] N. Dai, L.C. Zhang, J. Zhang, Q. Chen, M. Wu, Corrosion behavior of selective laser melted Ti-6Al-4 V alloy in NaCl solution, *Corros. Sci.* (2016). doi:10.1016/j.corsci.2015.10.041.
- [83] X. Lou, M. Song, P.W. Emigh, M.A. Othon, P.L. Andresen, On the stress corrosion crack growth behaviour in high temperature water of 316L stainless steel made by laser powder bed fusion additive manufacturing, *Corros. Sci.* (2017). doi:10.1016/j.corsci.2017.09.017.
- [84] L. Ding, H. Torbati-Sarraf, A. Poursaei, The influence of the sandblasting as a surface mechanical attrition treatment on the electrochemical behavior of carbon steel in different pH solutions, *Surf. Coatings Technol.* (2018). doi:10.1016/j.surfcoat.2018.08.013.
- [85] X.Y. Wang, D.Y. Li, Mechanical and electrochemical behavior of nanocrystalline surface of 304 stainless steel, *Electrochim. Acta.* (2002). doi:10.1016/S0013-4686(02)00365-1.
- [86] P. Montoya, C.R. Martins, H.G. De Melo, I. V. Aoki, F. Jaramillo, J.A. Calderón, Synthesis of polypyrrole-magnetite/silane coatings on steel and assessment of anticorrosive properties, *Electrochim. Acta.* 124 (2014) 100–108. doi:10.1016/j.electacta.2013.07.105.
- [87] S. He, Z. Wang, J. Hu, J. Zhu, L. Wei, Z. Chen, Formation of superhydrophobic micro-nanostructured iron oxide for corrosion protection of N80 steel, *Mater. Des.* 160 (2018) 84–94. doi:10.1016/j.matdes.2018.09.002.
- [88] J.K. Saha, *Corrosion of Constructional Steels in Marine and Industrial Environment*, 2013. doi:10.1080/08940886.2017.1316123.

- [89] W.S. Li, J.L. Luo, Uniformity of passive films formed on ferrite and martensite by different inorganic inhibitors, *Corros. Sci.* (2002). doi:10.1016/S0010-938X(01)00178-0.
- [90] M. Moine, N. Mary, B. Normand, L. Peguet, A. Gaugain, H.N. Evin, Tribo electrochemical behavior of ferrite and ferrite-martensite stainless steels in chloride and sulfate media, *Wear.* (2012). doi:10.1016/j.wear.2012.06.001.
- [91] S. Qu, X. Pang, Y. Wang, K. Gao, Corrosion behavior of each phase in low carbon microalloyed ferrite-bainite dual-phase steel: Experiments and modeling, *Corros. Sci.* 75 (2013) 67–77. doi:10.1016/j.corsci.2013.05.017.
- [92] H. Irani, M.S. Ghazani, Effect of grain refinement on tensile properties and electrochemical behavior of Fe-18.5%Cr ferritic stainless steel, *Mater. Chem. Phys.* (2020) 123089. doi:10.1016/j.matchemphys.2020.123089.
- [93] P.K. Rai, S. Shekhar, K. Mondal, Development of gradient microstructure in mild steel and grain size dependence of its electrochemical response, *Corros. Sci.* 138 (2018) 85–95. doi:10.1016/j.corsci.2018.04.009.
- [94] T. Suter, Y. Müller, P. Schmutz, O. von Trzebiatowski, Microelectrochemical Studies of Pit Initiation on High Purity and Ultra High Purity Aluminum, *Adv. Eng. Mater.* 7 (2005) 339–348. doi:10.1002/adem.200500067.
- [95] Z. Ahmad, *Principles of Corrosion Engineering and Corrosion Control*, Elsevier Ltd, 2006. doi:10.1016/B978-0-7506-5924-6.X5000-4.
- [96] A.O. Borode, N.A. Ahmed, P.A. Olubambi, Electrochemical corrosion behavior of copper in graphene-based thermal fluid with different surfactants, *Heliyon.* 7 (2021) e05949. doi:10.1016/j.heliyon.2021.e05949.
- [97] B.S. Hou, Q.H. Zhang, Y.Y. Li, G.Y. Zhu, H.F. Liu, G.A. Zhang, A pyrimidine derivative as a high efficiency inhibitor for the corrosion of carbon steel in oilfield produced water under supercritical CO₂ conditions, *Corros. Sci.* (2020). doi:10.1016/j.corsci.2019.108334.
- [98] Y. Sun, Y. Rong, Y. Zhao, Y. Zhao, R. Hang, X. Yao, P.K. Chu, Electrochemical stability, corrosion behavior, and biological properties of Ni–Ti–O nanoporous layers anodically on NiTi alloy, *Corros. Sci.* 179 (2021) 109104. doi:10.1016/j.corsci.2020.109104.

- [99] X. Lu, Y. Li, P. Ju, Y. Chen, J. Yang, K. Qian, T. Zhang, F. Wang, Unveiling the inhibition mechanism of an effective inhibitor for AZ91 Mg alloy, *Corros. Sci.* (2019). doi:10.1016/j.corsci.2018.12.025.
- [100] P. Murkute, S. Pasebani, O.B. Isgor, Production of corrosion-resistant 316L stainless steel clads on carbon steel using powder bed fusion-selective laser melting, *J. Mater. Process. Technol.* (2019). doi:10.1016/j.jmatprotec.2019.05.024.
- [101] Q.H. Zhang, B.S. Hou, G.A. Zhang, Inhibitive and adsorption behavior of thiadiazole derivatives on carbon steel corrosion in CO₂-saturated oilfield produced water: Effect of substituent group on efficiency, *J. Colloid Interface Sci.* (2020). doi:10.1016/j.jcis.2020.03.065.
- [102] M.H. Abdi, N.B. Ibrahim, H. Baqiah, High magnetic saturation of undoped and cobalt-doped tin oxide prepared by sol–gel method annealed in air and nitrogen gas, *J. Sol-Gel Sci. Technol.* (2017). doi:10.1007/s10971-017-4305-3.
- [103] N. Maharjan, V.K. Murugan, W. Zhou, M. Seita, Corrosion behavior of laser hardened 50CrMo4 (AISI 4150) steel: A depth-wise analysis, *Appl. Surf. Sci.* (2019). doi:10.1016/j.apsusc.2019.07.172.
- [104] P.K. Katiyar, S. Misra, K. Mondal, Comparative Corrosion Behavior of Five Microstructures (Pearlite, Bainite, Spheroidized, Martensite, and Tempered Martensite) Made from a High Carbon Steel, *Metall. Mater. Trans. A Phys. Metall. Mater. Sci.* (2019). doi:10.1007/s11661-018-5086-1.
- [105] Y. Zuo, H. Wang, J. Xiong, The aspect ratio of surface grooves and metastable pitting of stainless steel, *Corros. Sci.* 44 (2002) 25–35. doi:10.1016/S0010-938X(01)00039-7.
- [106] Z. Li, D. Zhang, X. Su, S. Yang, J. Xu, R. Ma, D. Shan, B. Guo, Removal mechanism of surface cleaning on TA15 titanium alloy using nanosecond pulsed laser, *Opt. Laser Technol.* 139 (2021) 106998. doi:10.1016/j.optlastec.2021.106998.
- [107] T. Shi, C. Wang, G. Mi, F. Yan, A study of microstructure and mechanical properties of aluminum alloy using laser cleaning, *J. Manuf. Process.* 42 (2019) 60–66. doi:10.1016/j.jmapro.2019.04.015.
- [108] C. Schultz, M. Fenske, J. Dagar, A. Zeiser, A. Bartelt, R. Schlatmann, E. Unger, B. Stegemann, Ablation mechanisms of nanosecond and picosecond laser scribing for

- metal halide perovskite module interconnection – An experimental and numerical analysis, *Sol. Energy*. 198 (2020) 410–418. doi:10.1016/j.solener.2020.01.074.
- [109] Y. WANG, X. PAN, X. WANG, Z. LIU, S. LIU, W. WAN, P. WANG, Influence of laser shock peening on surface integrity and tensile property of high strength low alloy steel, *Chinese J. Aeronaut.* (2020). doi:10.1016/j.cja.2020.09.004.
- [110] N. Maharjan, W. Zhou, N. Wu, Direct laser hardening of AISI 1020 steel under controlled gas atmosphere, *Surf. Coatings Technol.* (2020). doi:10.1016/j.surfcoat.2020.125399.
- [111] H.S. Dewi, A. Fischer, J. Volpp, T. Niendorf, A.F.H. Kaplan, Microstructure and mechanical properties of laser surface treated 44MnSiVS6 microalloyed steel, *Opt. Laser Technol.* 127 (2020) 106139. doi:10.1016/j.optlastec.2020.106139.
- [112] A. Cabrilo, A. Sedmak, Z. Burzic, S. Perkovic, Fracture mechanics and fatigue crack propagation in armor steel welds, *Eng. Fail. Anal.* 106 (2019). doi:10.1016/j.engfailanal.2019.104155.
- [113] *Metallurgical Failure Analysis*, Elsevier, 2018. doi:10.1016/c2017-0-01343-5.
- [114] A.J. Sadowski, J. Michael Rotter, P.J. Stafford, T. Reinke, T. Ummenhofer, On the gradient of the yield plateau in structural carbon steels, *J. Constr. Steel Res.* 130 (2017) 120–130. doi:10.1016/j.jcsr.2016.11.024.
- [115] F. Hu, G. Shi, Constitutive model for full-range cyclic behavior of high strength steels without yield plateau, *Constr. Build. Mater.* 162 (2018) 596–607. doi:10.1016/j.conbuildmat.2017.11.128.
- [116] P.J. Noell, J.D. Carroll, B.L. Boyce, *Acta Materialia* The mechanisms of ductile rupture, *Acta Mater.* 161 (2018) 83–98. doi:10.1016/j.actamat.2018.09.006.
- [117] A.T. Myers, G.G. Deierlein, A. Kanvinde, *Testing and Probabilistic Simulation of Ductile Fracture Initiation in Structural Steel Components and Weldments*, (2013) 386. <https://purl.stanford.edu/tn725xk1691>.
- [118] W. Guo, R. Sun, B. Song, Y. Zhu, F. Li, Z. Che, B. Li, C. Guo, L. Liu, P. Peng, Laser shock peening of laser additive manufactured Ti6Al4V titanium alloy, *Surf. Coatings Technol.* 349 (2018) 503–510. doi:10.1016/j.surfcoat.2018.06.020.
- [119] J. He, J. Lian, G. Golisch, A. He, Y. Di, S. Münsterman, Investigation on micromechanism and stress state effects on cleavage fracture of ferritic-pearlitic

REFERENCES

- steel at $-196\text{ }^{\circ}\text{C}$, *Mater. Sci. Eng. A.* 686 (2017) 134–141. doi:10.1016/j.msea.2017.01.042.
- [120] Y.C. Lin, X. Zhu, W. Dong, H. Yang, Y. Xiao, N. Kotkunde, Effects of deformation parameters and stress triaxiality on the fracture behaviors and microstructural evolution of an Al-Zn-Mg-Cu alloy, *J. Alloys Compd.* 832 (2020) 154988. doi:10.1016/j.jallcom.2020.154988.
- [121] W. Zhou, X. Ren, Y. Yang, Z. Tong, L. Chen, Tensile behavior of nickel with gradient microstructure produced by laser shock peening, *Mater. Sci. Eng. A.* 771 (2020) 138603. doi:10.1016/j.msea.2019.138603.

ACKNOWLEDGEMENT

Foremost, I would like to express my deepest appreciation to my supervisor, Assoc. Prof. Shigenobu Kainuma, whose expertise was invaluable in formulating the research and methodology. His guidance helped me in all the time of research and writing this dissertation.

Besides my supervisor, I would like to thank the dissertation examining committee: Prof. Hidenori Hamada and Prof. Hiroaki Nakano. Your insightful feedback pushed me to sharpen my thinking and brought my work to a higher level.

I would like to acknowledge Takahiro Asano from West Nippon Expressway Company Limited, Manabu Haraguchi and Hirohisa Miki from TOYOKOH Inc. for their wonderful collaboration. I would particularly like to single out Research Assistant Professor Muye Yang, Secretary Ms. Reiko Kato and Ms. Sayuri Gondo, Technical staff Mr. Hiroyuki Shibata in structural design laboratory, for their patient support.

My sincere thanks also goes to fellow labmates: Kazuya Yamashita, Aran Kim, Sanghong Park, Yang Gao, Weikun Xu, Haoxuan Yang, Qidi Wang, Jiajing Xie, Maoling Zhao, Saki Okada, Weijie Liu, Keisuke Suzuki, Ryohei Toyota, Soushi Tanaka and Kaishi Takaki, for the stimulating discussions, for the sleepless nights we were working together, and for all the fun we have had.

Last but not the least, I would like to thank my family, for supporting me throughout my life.